NASA NGT-70153

IMPACT OF INFERRED LATENT HEATING RATES ON PREDICTIONS OF CONVECTIVE STORMS

by Sandra L. Grant Henry

William R. Cotton, Co-P.I.
Roger A. Pielke, Co-P.I.

Colorado State University

DEPARTMENT OF ATMOSPHERIC SCIENCE

PAPER NO. 487

IMPACT OF INFERRED LATENT HEATING RATES ON PREDICTIONS OF CONVECTIVE STORMS

by

Sandra L. Grant Henry

Department of Atmospheric Science

Colorado State University

Fort Collins, CO 80523

Research Supported by

National Aeronautics and Space Administration

under contract NGT-70153

November 8, 1991

Atmospheric Science Paper No. 487

ABSTRACT

IMPACT OF INFERRED LATENT HEATING RATES ON PREDICTIONS OF CONVECTIVE STORMS

A localized ordinary thunderstorm system occurred during the Convective Initiation and Downburst Experiment (CINDE), in the Denver, Colorado area on 29-30 July 1987. The three-dimensional, nonhydrostatic version of the Regional Atmospheric Modeling System (RAMS), developed at Colorado State University, was utilized in this case to investigate the impact of forced latent heating rates on short-range (12 hours or less) quantitative precipitation forecasts (QPFs). This was accomplished by using estimated convective precipitation rates, in a modified Kuo-type convective parameterization scheme, to determine the vertical-distribution of latent-heating rates. The inferred heating rates were then used, instead of the model predicted heating rates, to guide the model to a more desirable state. The sensitivity of the model to a variety of precipitation rates and the impact of the duration of simulation time are also examined.

The 12 hour simulation with no forced heating failed to predict any precipitation in the northeast Colorado region. On the other hand, while the 24 hour simulation with no forced heating did predict precipitation in the northeast area of interest, the precipitation was positioned too far north of the observed precipitation area and the intensity was too small. In general, 12 hour simulations that used forced heating rates, for a one hour period during the simulation, produced the most improved precipitation forecasts. However, the

results were extremely sensitive to the various precipitation rates used to obtain the forced heating rates, with weaker values having no impact at all and the strongest rates producing the most improved forecast.

Sandra L. Grant Henry
Department of Atmospheric Science
Colorado State University
Fort Collins, Colorado 80523
Fall 1991

ACKNOWLEDGEMENTS

I would like to express my gratitude to my adviser, Dr. William Cotton, for his guidance and support throughout this study. The comments from my other committee members, James Fankhauser, Dr. Richard H. Johnson and Dr. Paul Mielke, are also appreciated.

My thanks are also extended to Dr. Craig Tremback and Dr. Robert Walko for helping me run and modify the model. Mike Meyers is recognized for his helpful comments regarding this paper. Thanks are also extended to Brenda Thompson for her advice and assistance in manuscript preparation and to Lucy McCall and Walter Grant for their help with drafting the figures.

I would also like to thank the Mesoscale and Microscale Meteorology division of the National Center for Atmospheric Research (NCAR) for generously providing me with additional work space and allowing me to use their facilities.

Finally, a special thanks is extended to my family and friends for their continued support, patience and encouragement during my graduate studies and life in general, especially my husband, Bernard Henry.

This research was supported by the National Aeronautics and Space Administration under contract NGT 70153. Some of the computing was done at NCAR, which is supported by the National Science Foundation.

TABLE OF CONTENTS

LIST OF FIGURES

Chapter 1

INTRODUCTION

Convective rain is rainfall which is caused by vertical motion of an ascending mass of air which is warmer than its environment. In many regions mesoscale convective precipitation is a significant source of water for plants and animals. However, convective storms can also negatively impact regions because they are often associated with lightning, hail, flash floods, and strong, damaging winds. To minimize the negative impact, more knowledge and better predictions of these storms are needed.

Forecasting the time and location of convective-scale precipitation accurately has been difficult in the past, and despite the continuous progress made over the years, it still remains a challenge for today's numerical weather models. For most cases where good mesoscale quantitative precipitation forecasts (QPFs) have been produced using only smooth synoptic-scale data, the model dynamics and physics-parameterizations have had sufficient time to develop mesoscale structures before the onset of precipitation (Wang and Warner, 1988). Also, even though these experimental mesoscale QPFs are very encouraging by historical standards, they often still do not verify well objectively. That is, the model may predict the convective event during the correct 12 hour time period and in the correct state, but it generally does not provide more exact timing and position information. Nevertheless, these forecasts are still considered fairly successful from a modelling viewpoint.

One method utilized to produce improved short-range (0-12 hour) QPFs, is to use precipitation rates, estimated from radar or satellite data, to define a three-dimensional heating rate field that contributes to the diabatic heating term in the model's thermodynamic equation. Thus, the inferred heating rates are used in place of model-predicted

heating rates to guide the model towards radar or satellite observations which have a higher frequency and spatial density than standard synoptic observations. This reduces the time required to spin-up (generate) mesoscale circulation systems in prediction models, which typically spend the first 2-6 hours of a forecast adjusting to the initial fields and establishing low-level moisture convergence.

The main objective of this thesis is to investigate the impact of incorporating heating rates, inferred from precipitation data, into mesoscale models in an attempt to predict localized ordinary thunderstorms that are not adequately resolved in the model's simulation. This objective was accomplished by using estimated convective precipitation rates, in a modified Kuo-type convective parameterization scheme at a time that storms were observed, to determine the vertical distribution of heating rates. The inferred heating rates were then used, in place of the model predicted heating rates, to guide the model to a more observed state. The new contribution made by this study is that the diabatic heating rates are being used to drive the model toward the observed atmosphere at the time that the storm is observed, instead of focusing on reducing the spin-up time by initializing the model with forced heating rates. The benefit of this technique is that if while running a model in real-time a storm is observed that is not simulated by the model, precipitation rates can be inserted, at that time, to infer heating rates that will guide the model to a more observed state.

This study was performed by employing the Regional Atmospheric Modelling System (RAMS), developed at Colorado State University, to a Convective Initiation and Downburst Experiment (CINDE) case study on 29 July 1987 in northeast Colorado. The sensitivity of the model to different precipitation rates will be examined by comparing estimates obtained from conventional radar and surface rain gauges.

Chapter 2

LITERATURE REVIEW

Despite the continuous progress made during recent years, numerical weather prediction models are still plagued by a slowness to forecast baroclinic development and appropriate amounts of precipitation during the first few (12) hours of model time integration (Turpeinen et al., 1989). Consequently, the usefulness of numerical weather prediction models in very- short-range forecasting (0-12 hours) is limited by this so-called spin-up problem. The spin-up problem is sometimes characterized by significant negative departures of the precipitation field from the observations during the initial stages of a forecast, especially for strong rainfall events (Lejenas, 1980; Benoit and Roch, 1987; Turpeinen et al.,1989). This is partly caused by a poorly resolved initial moisture analysis, as the density of data made available to objective analysis programs is generally insufficient to describe mesoscale features (Ninomiya and Kurihara, 1987). The other factor is the frequent exclusion of the existing condensation activity (Anthes et al., 1981), which constitutes a significant heat source affecting the mass/flow fields' mutual adjustment.

Cumulus convection can have an important effect on the dynamics and energetics of larger scale atmospheric systems because of the large magnitude of the energy transformations associated with the changes of phase of water in precipitating cumulus clouds (Cotton and Anthes, 1989). Thus, the inclusion of observed latent heat sources and of a consistent and higher-resolution moisture analysis are critical components in reducing the underestimation of initial divergence, which in turn directly affects the modeled convective-storm development in the early hours of the simulation.

Consequently, numerous studies have employed techniques for retrieval of heating rates using rainfall data in an attempt to produce better QPFs. This chapter will briefly

discuss methods used for estimating precipitation rates and then summarize various studies which have used latent heating rates, inferred from precipitation data, to initialize models; focusing on those studies which utilized diabatic initializations during 1981-1989.

2.1 Precipitation Rate Estimates

Several meteorological instruments have been used over the years to obtain estimates of rainfall rates. This section will describe methods used and the problems encountered with precipitation rates estimated from surface rain gauges, satellite data and weather radars.

Surface rain gauges can be used to determine rainfall rates by measuring the amount of precipitation that has fallen over a specified period of time. However, the intensity of convective precipitation varies greatly over the storm area so it is not feasible to determine a representative instantaneous rainfall rate based on this method. Also, due to the spatial variability of convective rainfall and the great distance between observing sites, rain gauges may not represent any or only part of the total precipitation for any particular region.

Widespread data on the spatial characteristics of rain can be obtained from satellite data. The remote sensing techniques for estimating rain rates are based on a qualitative and quantitative interpretation of the thermal or reflected radiation emitted from the earth and the atmosphere either in the infrared and visible (Griffith, et al., 1978) or in the microwave spectral range (Adler and Rodgers, 1977). One of the biggest problems encountered when attempting to derive rainfall estimates from infrared and visible satellite imagery is that it's based on cloud-top temperature patterns, which may not accurately represent conditions at the surface or through the depth of the storm. For example, Augustine et al. (1981) presented results where significant rain from clouds whose tops do not reach the -20 C level contributed to satellite rain underestimates of radar-derived results, since these clouds were not considered rain clouds (typically, only clouds colder than -20 C are defined as rain clouds). The study also revealed an opposing effect, perhaps due to long-lived anvils, where overestimates for very deep convective storms were

produced. The microwave radiation emitted by the earth and atmosphere (expressed in terms of brightness temperature, TB) provides a vertical integral of atmospheric water vapor, liquid water and ice particles that can be related to rain rates. Thus, microwave satellite measurements can provide better rain rates than infrared satellite data since it can determine distinct features of the hydrometeor profiles at various vertical levels and detect warm rain, however, problems still exist. Smith et al. (1991) noted that one problem of predicting surface rainfall, using multi-channel TB, was due to the fact that no passive microwave frequencies can see clearly to the surface in the presence of rain.

One of the most efficient ways to estimate precipitation rates is by weather radar, which can provide better spatial coverage of a local convective storm than rain gauges and a better vertical distribution of the storm than satellite data. Conventional Doppler radars measure the mean power (or reflectivity, Z) as well as the mean velocity (Chandrasekar and Bringi, 1987). The rainfall rate, R, is conventionally related to Z by power law equations of the form $Z = aR^b$, where a and b depend on the unknown raindrop size distribution, Atlas (1964), Ulbrich (1983). The uncertainties involving drop-size distributions can cause significant errors in rainfall rate measurements (Doviak, 1983). Other factors that can have an equally important impact on the rain-rate measurements include the inability to clearly and reliably differentiate regions of rainfall from hail shafts, changes in vertical rainwater flux that is caused by vertical air motions at the radar scanning level, evaporation of rain below subcloud layer during descent, variations in horizontal airflow between scanning level and the ground and effects on radar signal strength such as, incomplete beam filling, attenuation, beam blockage, errors in radar calibration and reflectivity gradients across the beam.

Multiparameter radars, which are radars with dual frequency and dual polarization capability, can measure reflectivity, as well as, differential reflectivity (Z_{dr}), attenuation (A_x), and other parameters. The differential reflectivity technique was first introduced by Seliga and Bringi (1976) to improve the accuracy of radar estimates of rainfall rate over conventional (single-parameter) Z-R methods. In addition to producing improved accuracy in rain rates, differential reflectivity can also discriminate contributions by hail.

Differential reflectivity is derived as $Z_{dr} = 10log(Z_h/Z_v)$, where Z_h and Z_v are the horizontal and vertical polarized reflectivities, respectively.

2.2 Heating Rates

Several studies used latent-heat forcing to improve QPF in the 1980's. Summaries of the studies which utilized diabatic initializations during 1981-1989 are presented in the remainder of this chapter.

Fiorino and Warner (1981) perform a 12 hour dynamic initialization (DI), with a three-dimensional hurricane model, in which the latent heat release due to convection is externally specified based upon satellite estimates of rainfall rate. The dynamic initialization is performed by integrating the model for 12 hours where the convective heating term in the model's thermodynamic equation is specified according to the estimated rainfall rate. Vertical partitioning of the heating is based on representative profiles in tropical storms, obtained from cloud-model results of Anthes (1977). The Fiorino and Warner study reveal that 12 hour forecasts based on DI produce forecasts of surface pressure and precipitation that are greatly improved, compared to static initialization, and these forecasts are reflective of observed storm intensity; however the track forecasts are not significantly changed.

Regarding scale analysis, the diabatic heating term can be the largest of the forcing function terms in the mesoscale omega equation; if rain occurs at typical mesoscale rates, the diabatic term dominates. Based on this statement, Tarbell et al. (1981) and Salmon and Warner (1986) use mesoscale primitive equation models to conduct similar experiments; where latent heating rates are roughly estimated from routinely measured variables, including hourly rain rates (obtained from surface rain gauge measurements). The vertical distribution of latent heating was prescribed as a parabolic profile (maximum at mid-atmosphere pressure) with an amplitude derived from a gridding of the surface rain gauges at ± 3 hours. A mesoscale initialization procedure was then used, where the initial horizontal divergence is diagnosed from the omega-equation with the rate of latent heat used in the diabatic term. Both investigations showed that model-predicted rainfall

rates during the first several hours of the forecast period were smaller than observed. However, greatly improved 0-6 hour QPF were noted when diagnosed divergent-wind initialization were used.

Wang and Warner (1988) conducted two experiments where inferred latent heating rates were used to initialize a mesoscale primitive equation model. One experiment uses hourly raingauge data for the period, -1 to 0 hour (where 0 hour denotes the initialization time) and radar data near the initialization time period to construct an estimated precipitation-rate field appropriate for that time period. This two-dimensional field was then used to produce an estimate of the three-dimensional latent-heating field, which entirely determines the contribution to the diabatic-heating term in the model's thermodynamic equation for a specified period of time after the static initialization. The other experiment utilizes a four-dimensional data assimilation procedure. The latent-heating function was specified in a way identical to that described in the other experiment, but the forcing was applied only during the 12 hour preforecast period and was based on observed hourly precipitation during this period. The hourly precipitation rate analyses for the last 3 hours of the preforecast period were determined and from each of these fields, the three dimensional latent-heating function was defined, and applied for the appropriate one-hour period during the preforecast integration. The study showed considerable improvement when the model was initialized with a specified latent-heat forcing function, compared to simulations initialized with a conventional technique. They also concluded that even though some static initialization (SI) experiments were better than the DI experiments, it is encouraging that the dynamic-initialization procedures performed reasonably well because they can be viewed as less limited in one sense than the static-initialization procedure. That is, the application of a constant latent-heat forcing during the first forecast hour after the static initialization would not be as reasonable, and perhaps not as effective, for a rapidly evolving precipitation event.

In the study by Ninomiya and Kurihara (1987) an experiment is conducted where prescribed (forced) condensation heating is included in the first 1-hour of the time integration. The prescribed heating rate is estimated from a satellite IR observation and

a parabolic vertical profile is assumed to distribute the condensation heating. After the first 1-hour integration with this forced condensation heating, the time integration of the mesoscale primitive equation model progressed with the models own physical processes alone. The results from this investigation showed that the heating in the first 1-hour was effective to spin-up (or to generate) the meso-alpha-scale convective system in the correct time and over the correct area. The spin-up of the convective system, caused by the forced heating in the model, resulted in the timely change of circulations around the meso-alpha-scale convective system, and this change contributed to the further development of the convective system. Thus, the forced condensation heating in the first 1-hour had strong influence throughout the whole model integration period.

In a study by Puri and Miller (1990) a procedure is described in which outgoing longwave radiation (OLR) data, obtained from satellite data, is used in the specification of convective heating for diabatic initialization in the global European Center for Medium Range Weather Forecast (ECMWF) model. Two methods were used to determine convective heating rates from the derived precipitation rates. In the first method the intensity of heating, I, is determined from

$$I = \frac{L}{c_p} \frac{\dot{R}}{\int_{P_b}^{P_t} H(p)dp} \tag{2.1}$$

where H denotes the vertical profile of heating, $\dot{R}$ is the rainfall rate, P_t and P_b indicate the pressures at the top and bottom of the column, c_p is the specific heat and L is the latent heat of evaporation. The vertical profile of heating is obtained from vertical profiles of vertical motion, gathered from ECMWF analyses. The other method derives heating rates based on the Kuo convective parameterization scheme used in the model (where $\dot{R}$ from the OLR data is used to define the moisture convergence in the Kuo parameterization). The inferred heating rates are then used in diabatic normal mode initialization (NMI) to derive an initialized divergence field. They concluded that the specification of appropriate heating rates for diabatic NMI, in conjunction with the use of divergent structure functions during analysis, has the capability of producing an improved divergence field that is dynamically balanced through the use of diabatic NMI. However,

the balance achieved during initialization could be rapidly lost if the heating rates in the early stages of the model forecast were inconsistent with those used during initialization.

Danard (1985) uses a 4-dimensional data assimilation procedure, in a limited-area 8-level primitive equation model, to incorporate satellite estimates of precipitation into the initialization of operational numerical weather prediction models. Latent heating is then inferred from the estimated rain rates, that are assumed to be constant for 6 hours. The inferred latent heating then replaces the heating computed by the model, throughout the integration. The vertical distribution of the latent-heating is guided by the model if the model rain rate exceeded both 1 mm/hr and the observed rain rate; otherwise, a statistical profile is used. Danard's study revealed that having the latent heating and moisture estimated by satellite override the model's calculations produced an improved "first-guess" field which led to better analyses and prognoses.

Turpeinen et al. (1989) uses a hemispheric primitive equation model in their experiment. Two simulations were conducted: a control run with an adiabatic initialization and a test run with a forced diabatic initialization and humidity enhancement. The forced diabatic initialization, which is static (i.e. forcing inferred from constant rain rates), was based on satellite-inferred rain rates. Before the actual diabatic initialization, an adiabatic implicit normal mode initialization (INMI) was performed to establish an initialized vertical motion field, based on the initial dynamic fields. In the subsequent diabatic initialization, the initialized vertical motion field was employed in the condensation scheme to identify the columns where the motion is ascending and where condensation and subsequent latent heat release may occur. The results indicated that the adiabatic initialization resulted in spin-up times of nearly nine hours for the vertical motions. The spin-up time was drastically reduced by the diabatic initialization, where realistic vertical motions occurred from the very beginning of the integration. However, even though improved precipitation rates were obtained throughout the first nine hours of the integration, the rates continued to be deficient for the first few time-steps (up to 1-2 hours).

Chapter 3

THE CINDE EXPERIMENT

3.1 Experiment Objectives

The Convective Initiation and Downburst Experiment (CINDE) was conducted in the vicinity of Denver, Colorado from 22 June to 7 August, 1987. The field experiment was a joint venture with participating agencies from the National Center for Atmospheric Research (NCAR), National Oceanic and Atmospheric Administration (NOAA), the University of Wyoming (UW), the University of California at Los Angeles (UCLA), the University of North Dakota (UND), the Colorado State University (CSU), and the Massachusetts Institute of Technology (MIT) Lincoln Laboratory. The objective of the project was to study the kinematic and thermodynamic properties of clear air, wind convergence lines in the planetary boundary layer that lead to the initiation of convective storms, to study the initiation and forcing of downburst downdrafts, and to investigate the structure and evolution of the mesoscale boundary layer.

3.2 Location and Topography

The 80 km X 50 km CINDE network, which was located along the front range of the Rocky Mountains in the northeastern part of Colorado, was surrounded by complex terrain. This terrain had a significant affect on the daily weather in the vicinity of Denver and is believed to be partially responsible for the initiation of the storm on 29 July 1987, which is the case that will be examined in this study. Figure 3.1 shows that the network is less than 30 km east of the Rocky Mountains (which have peaks greater than 3700 m above MSL, rising more than 2000 m above the plains). The Palmer Ridge is 50 km south of Denver with an east-west orientation and reaches a maximum height of ~800m.

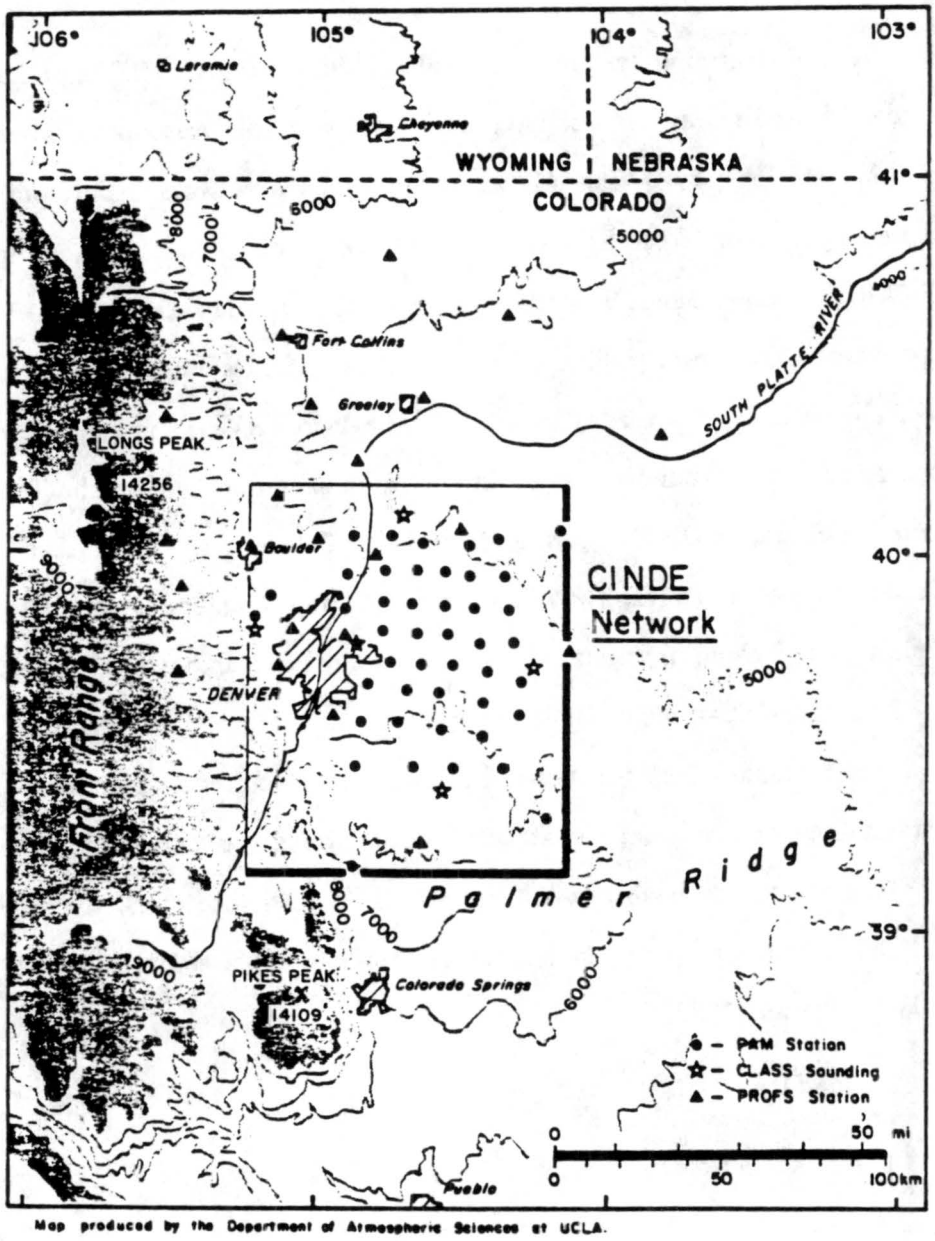

Figure 3.1: Geographical map of northeast Colorado. The area covered by the CINDE network is also shown. This figure is taken from the Operation and Data Summary for the Convection Initiation and Downburst Experiment.

The Cheyenne Ridge is another ridge orientated perpendicular to the Rockies, positioned 250 km north of the Palmer Ridge. The Cheyenne Ridge, like the Palmer Ridge, reaches a maximum height at the intersection with the Front Range and decreases in amplitude to the east; however, the maximum height is only 400 m.

3.3 Instrumentation

Several operating systems were utilized during the CINDE experiment. They included three Doppler radars, forty-six NCAR Portable Automated Mesonet (PAM II) weather stations, two King Air aircraft, five NCAR Cross-chain Loran Atmospheric Sounding System (CLASS) stations and three mobile sounding vans, and an array of NCAR time-lapse movie and still camera equipment. Locations of the CINDE operating systems are shown in Figure 3.2. In addition to these observing facilities, data were available from the Denver National Weather Service (NWS) and three other experiments being conducted around the same time. These experiments were the Terminal Doppler Weather Radar (TDWR) operational test, the Denver Advanced Weather Information Processing System (AWIPS)-90 Risk Reduction and Requirement Evaluation, and a precipitation and cloud-physics study conducted by Colorado State University (CSU) using the NCAR multiparameter CP-2 radar.

The radars, surface mesonetwork stations and soundings, which were all beneficial in determining the precipitation rates and/or describing the mesoscale features of the case (see Chapter 4), will be discussed further in the following sections. A complete list of the CINDE observing systems, their characteristics and affiliated organizations can be found in Wilson et al. (1988).

3.3.1 Radars

Three radars were used exclusively by the CINDE experiment. They were the NCAR CP-3 C-band (5 cm wavelength) Doppler radar and the NOAA-C and NOAA-D X-band (3 cm wavelength) Doppler radars. The CP-3 radar was located at Denver Stapleton International Airport along with the operations center, and typically began scanning by 1700 UTC each day and continued until the close of operations. CP-3 provided

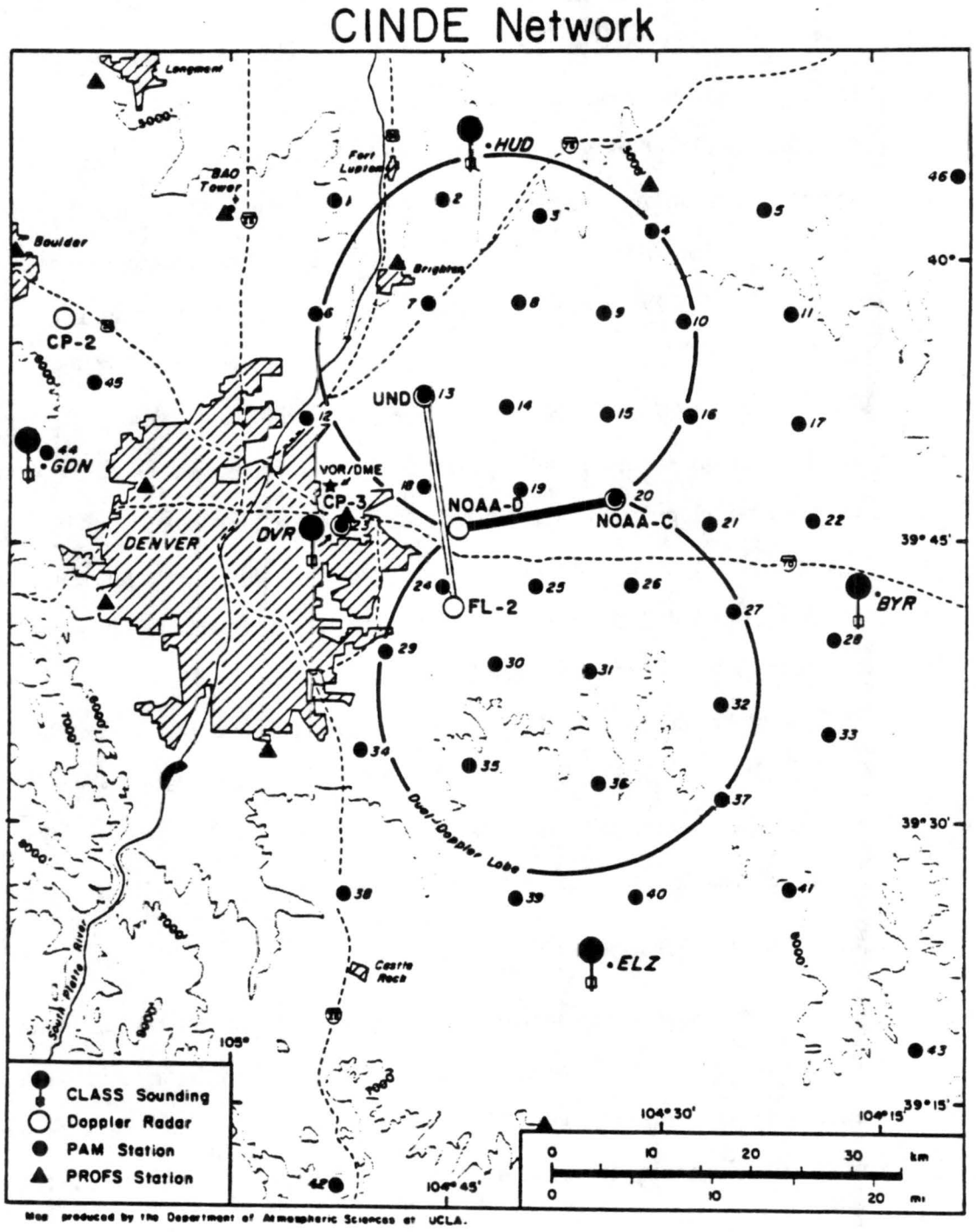

Figure 3.2: Locations of the CINDE operating systems. This figure is taken from the Operation and Data Summary for the Convection Initiation and Downburst Experiment.

continuous, 360°azimuth, radar surveillance at various elevation angles during the field operations. The two scan modes that were used are called pre-storm and storm. The pre-storm scan concentrated on low levels; however it had sufficiently high altitude to monitor storm development over the mountains. The storm scan was employed when storms were within or near the CINDE network.

The NOAA radars were separated by 15.9 km, as shown in Figure 3.2, allowing for high resolution dual-Doppler measurements. The two radars were the same in most respects; however, NOAA-C had additional dual-circular polarization capability.

The NCAR CP-2 radar is a dual-wavelength (3 and 10 cm wavelength) and dual-polarization (vertical and horizontal) radar. It was operated for PROFS (Program for Regional Observing and Forecasting Services) from 22 June to 10 July. During this time period a scanning sequence similar to the CP-3 pre-storm and storm scans was utilized. A separate research program, conducted by CSU, operated the radar from 10 July through 10 August. At this time the radar typically collected high resolution, multi-parameter data in RHI and PPI mode while sectoring a particular storm. A 360°surveillance scan at 0.7°elevation was obtained every 5 minutes.

Two other radars, the FL-2 S-band from Lincoln Laboratory and the University of North Dakota (UND) C-band Doppler radars were also located within the CINDE network. These radars collected data primarily for the TDWR program. The locations of these six Doppler radars are shown in Figure 3.2.

3.3.2 Surface Mesonetwork Stations

Forty-six Portable Automated Mesonet (PAM) II weather stations were deployed as shown in Figure 3.2. Forty-one stations comprised the primary grid, with a typical station spacing of about 10 km. The remaining five PAM II stations were deployed in areas surrounding this network. The PAM II stations provided 1-minute averages of wet and dry bulb temperature, pressure, the u and v components of the wind, and rainfall.

PROFS and the Federal Aviation Administration (FAA)-Lincoln Laboratory Operational Weather Studies (FLOWS) mesonet stations located in and around the CINDE

PAM network provided additional information on the structure of the mesoscale fields over the region.

3.3.3 Soundings

A fixed network of upper-air sounding stations consisted of five NCAR Cross-chain LORAN (Long-Range Aid to Navigation) Atmospheric Sounding System (CLASS) stations located at various sites throughout the CINDE network (see Figure 3.2). The CLASS soundings provided real-time displays of temperature, pressure, dew-point, wind direction, and wind speed at 10-sec intervals.

Three mobile sounding systems were also used, to supplement the soundings made from the fixed CLASS sites. These sounding systems utilized radiosondes that transmitted temperature, pressure, and relative humidity at 5-second intervals. The winds aloft were obtained by tracking the balloon visually using an optical theodolite.

Chapter 4

WEATHER SUMMARY OF THE CASE STUDY

The numerical experiments conducted in this study are based upon a convective storm that occurred in Denver Colorado on 29-30 July 1987. A detailed analysis of the case was possible due to the data collected from the CINDE experiment. This case study day was characterized by an abundance of low-level moisture and warm temperatures, which would indicate a strong possibility for convective storms later in the day.

As predicted, convective storms did develop shortly after 1630 MDT over the area of interest, an 80 km X 80 km area which included the majority of PAM stations and the CP3 doppler radar positioned at the origin of the grid. Figure 4.1 shows the grid used in the study (outlined by the dashed box) and the PAM station locations. The storms formed along a northeast/southwest convergence line. This line was produced as a storm over the mountains, northwest of the network, produced a gust front which collided with outflow from another storm south of the network. The storms northwest and south of the CINDE network were too far away to be observed by the mesonet data but these storms were observed visually and recorded in the CINDE log book. An overview of the synoptic and mesoscale features occurring on this day is provided in the following sections of this chapter.

4.1 Synoptic Features

The 850 mb and 500 mb analysis for 1200 UTC on 29 July (see Figures 4.2 and 4.3, respectively) depict the associated synoptic scale features for this storm. Weak pressure gradients and generally light and variable winds were observed over the entire United States at 850 mb with the exception of a few stations reporting southwesterly winds

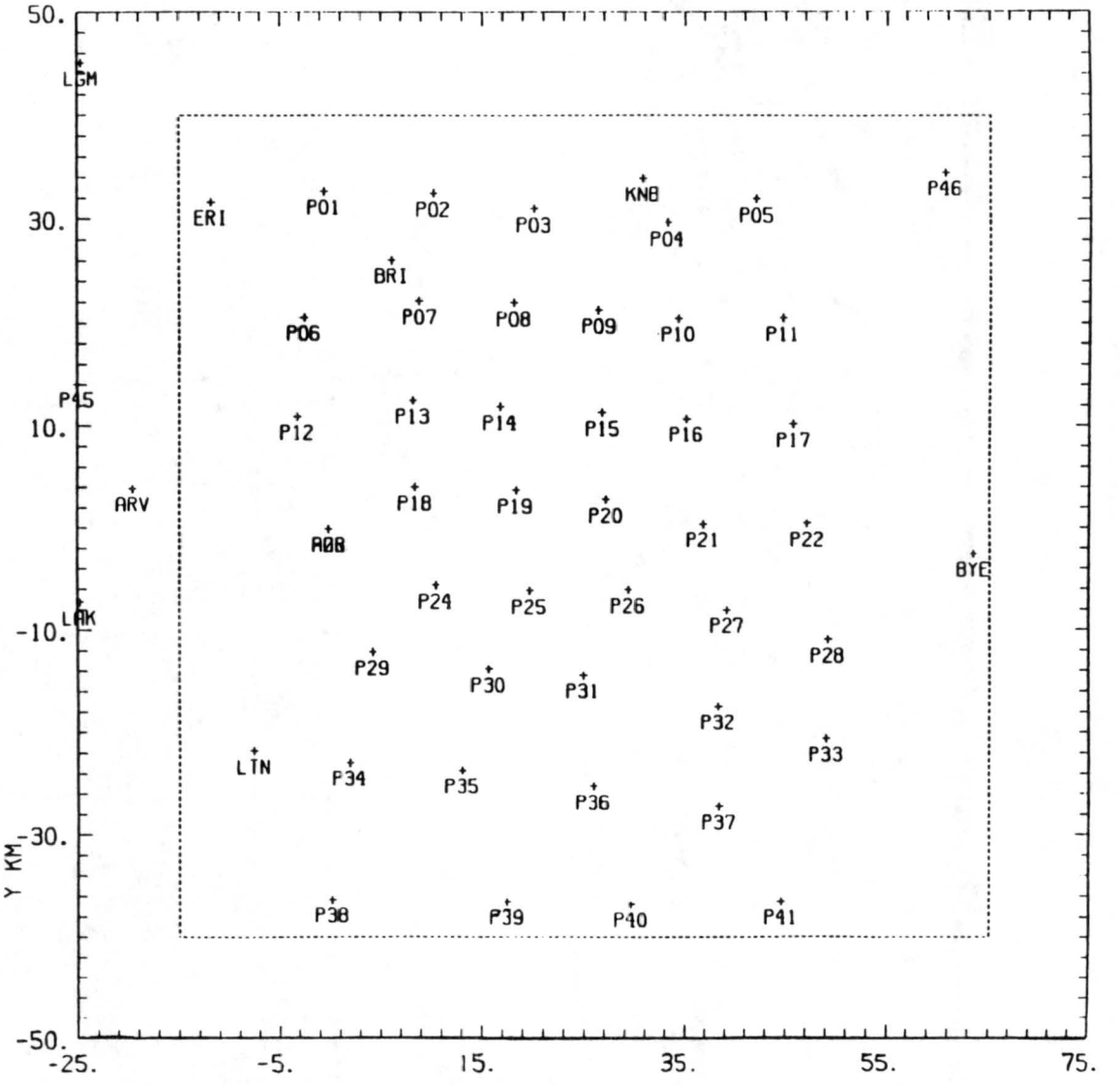

Figure 4.1: Locations of the PAM stations. The 80 km X 80 km grid used in the mesoscale analysis is outlined by the dashed box. The CP3 radar is located at the origin (0,0 km).

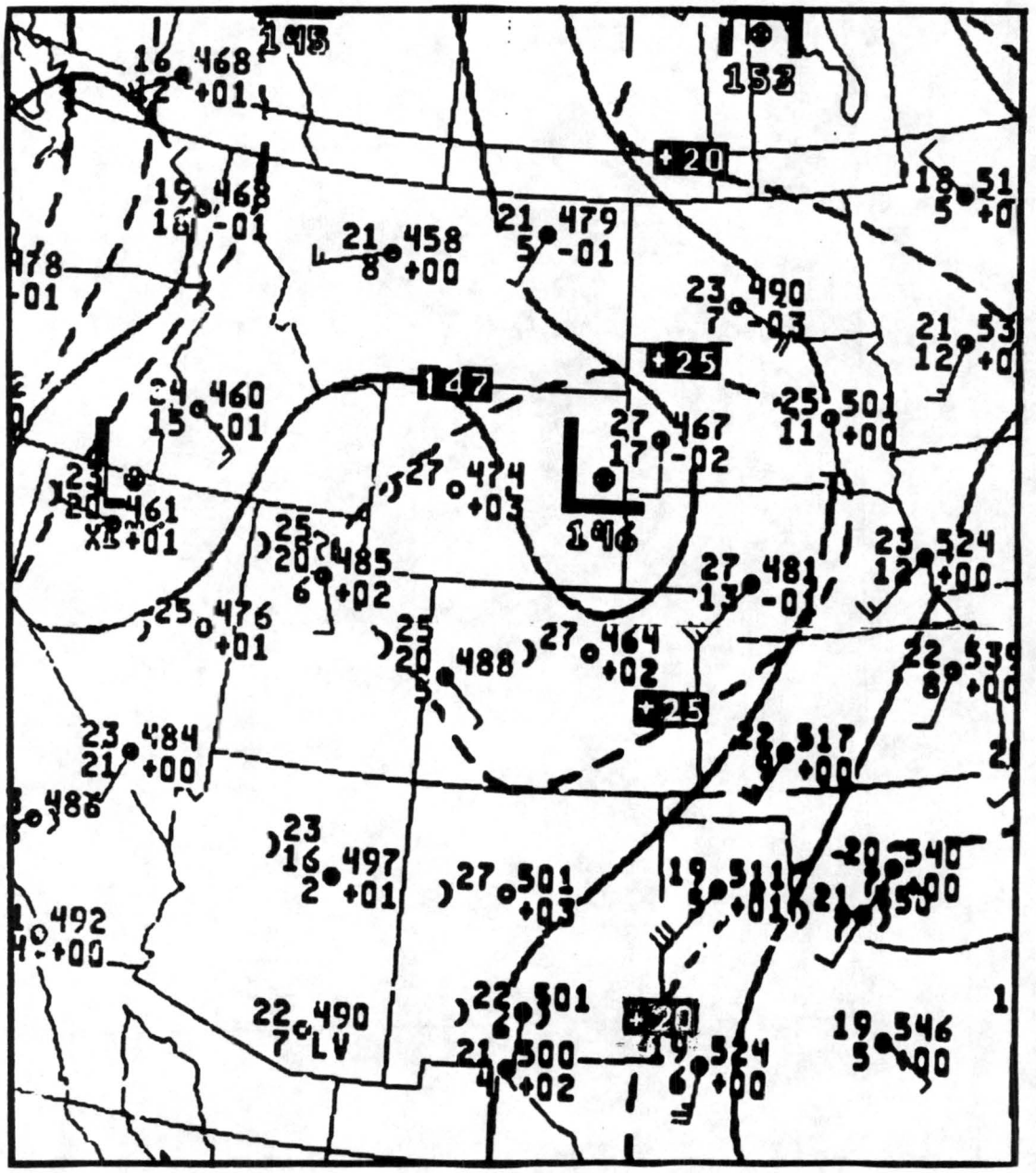

Figure 4.2: 29 July 1987 1200 UTC 850 mb analysis.

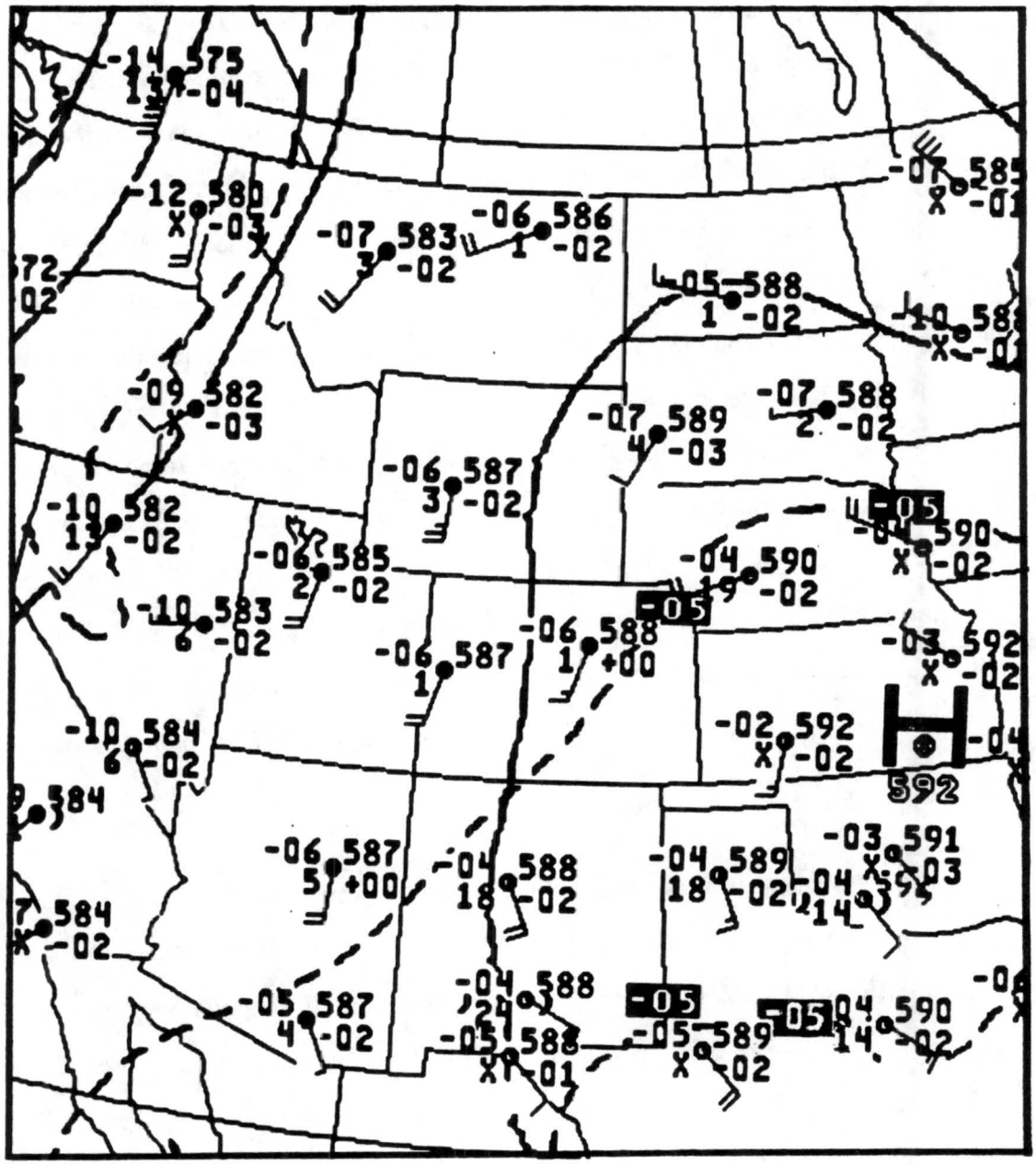

Figure 4.3: 29 July 1987 1200 UTC 500 mb analysis.

greater than 20 m/s over western Texas, Kansas, and Nebraska. A weak trough was also observed over eastern Wyoming at 850 mb. A pronounced ridge dominated the entire United States at 500 mb, which was centered over eastern Kansas. Southwesterly synoptic-scale flow occurred over Colorado at the 500 mb level with speeds ranging from 15 to 20 m/s. As a result of this 500 mb flow, warm, moist air was advected into Colorado with a temperature of -6°C at this level and a dewpoint depression of 1°C.

The National Weather Service (NWS) radar summary maps provided large-scale information about the precipitation patterns in the Rocky Mountain region on the day of interest. A twelve hour history (29 July at 1635 to 30 July at 0435 UTC) is depicted in Figures 4.4a-g at two hour intervals. These maps reveal that no rain was observed over Colorado until 1835 UTC (1235 MDT), when thunderstorms and rainshowers started to develop over the mountains and western Colorado. The thunderstorm located over the central mountains intensified and moved farther north over the next two hours. Another cell was also starting to form in southern Colorado at this time. The storms continued to grow, and by 2235 UTC hail was observed southwest of the Denver area. Two hours later (0035 UTC on 30 July) strong convective storms were still observed and an intense storm was located in the Denver area. The storms were less intense two hours later and by 0435 UTC only a few rainshowers were noted; primarily in northern Colorado.

4.2 Mesoscale Features

Mesoscale features were examined using data from the CINDE project. Surface wind, potential temperature and mixing ratio fields, and precipitation amounts were obtained from the PAM stations by using the GEneral Mesonet INterpolation Interface - GEMINI - batch processor (Bradford, 1988) to remap data collected by the mesonet stations, at irregularly spaced locations, to a two-dimensional cartesian grid. The Custom Editing and Display of Reduced Information in Cartesian space (CEDRIC) software analysis package (Mohr et al., 1986) was then used for subsequent data manipulation.

The environmental changes which occurred with the passage of a gust front through the CINDE observing network will be examined in the remainder of this section. The

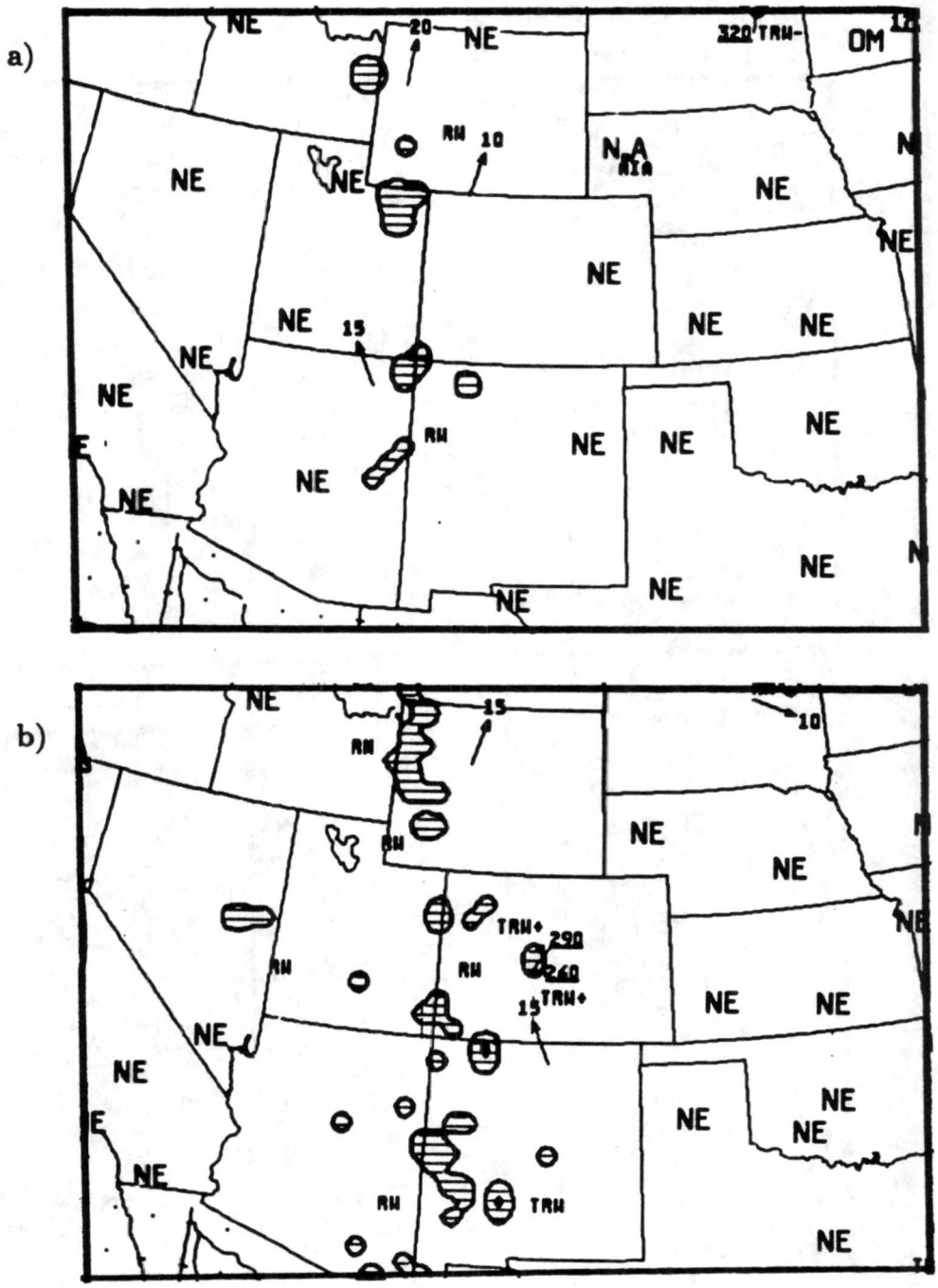

Figure 4.4: National Weather Service radar summaries from a) 1635 UTC 29 Jul 1987, b) 1835 UTC 29 Jul 1987, c) 2035 UTC 29 Jul 1987, d) 2235 UTC 29 Jul 1987, e) 0035 UTC 30 Jul 1987, f) 0235 UTC 30 Jul 1987 and, g) 0435 UTC 30 Jul 1987.

c)

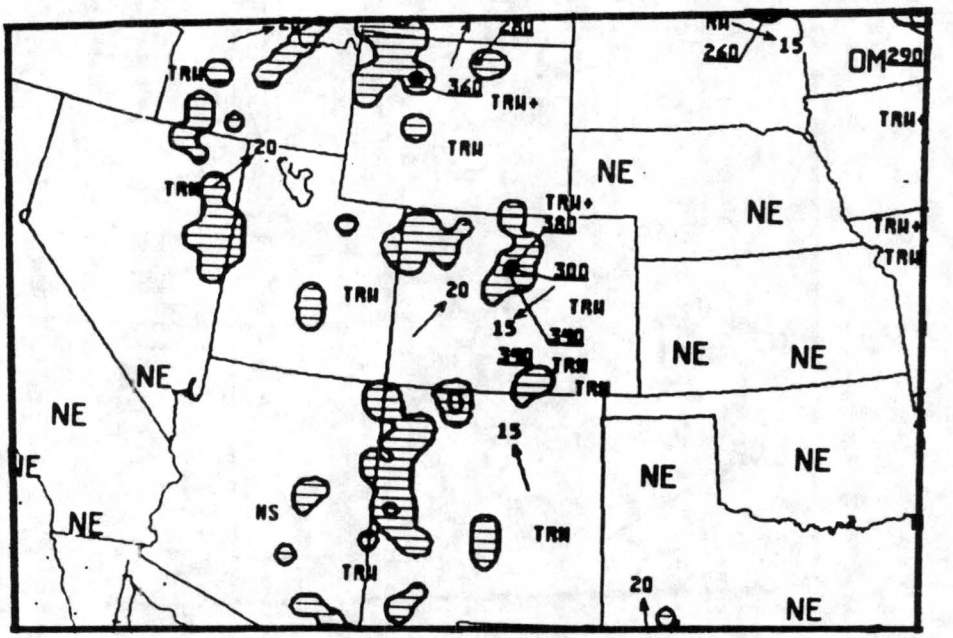

d)

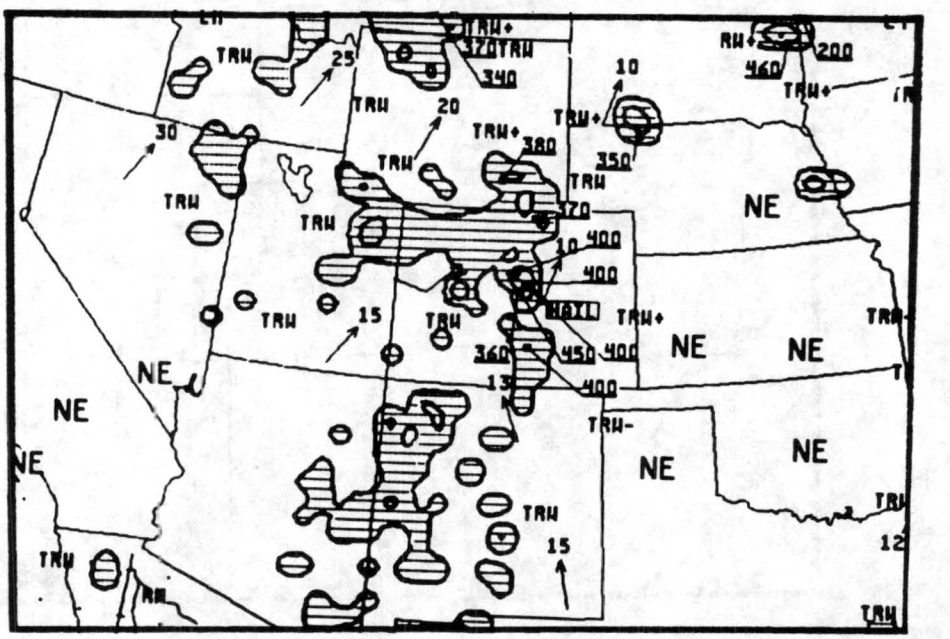

Figure 4.4: Continued.

e)

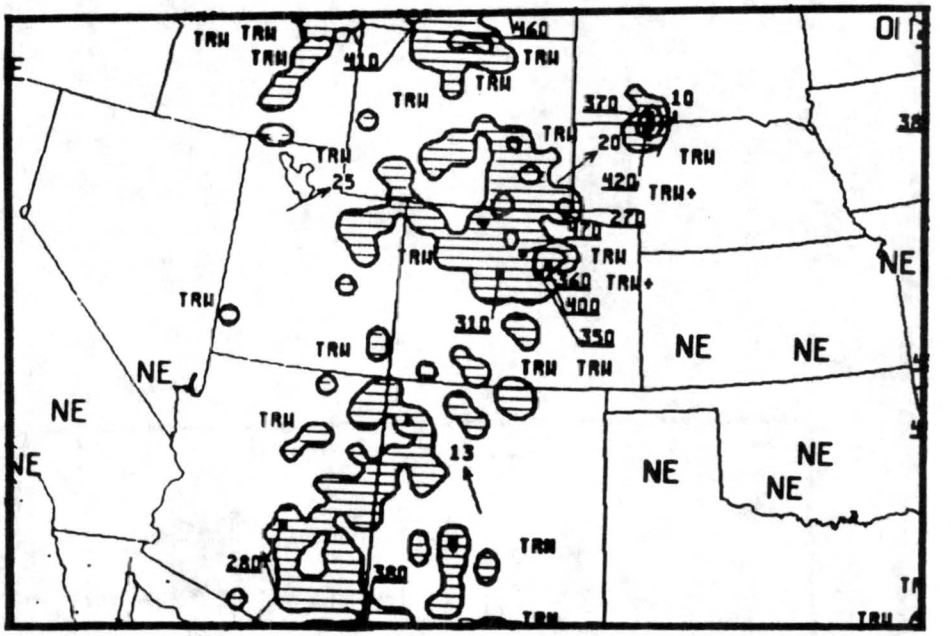

f)

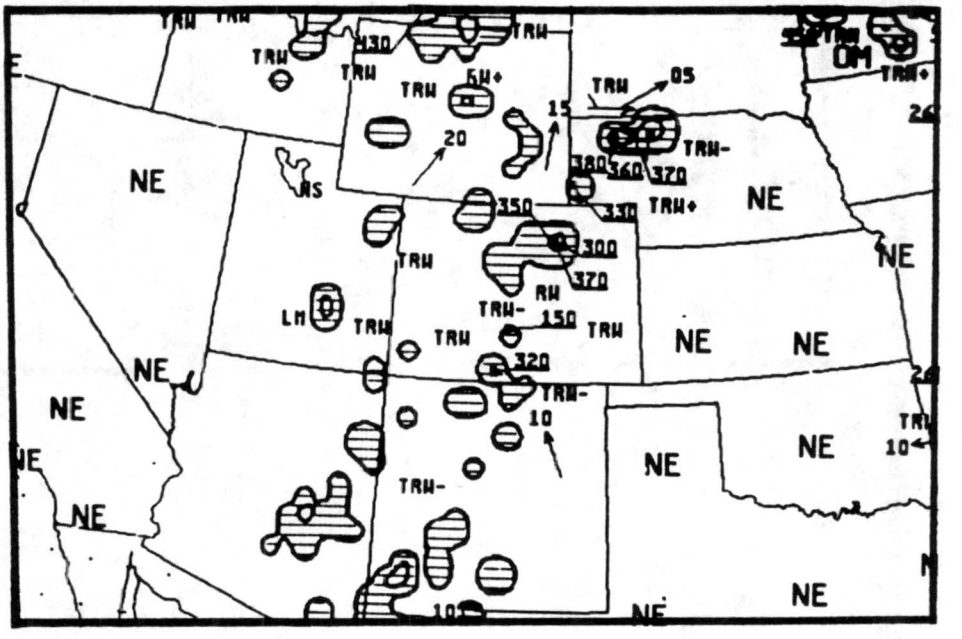

Figure 4.4: Continued.

g)

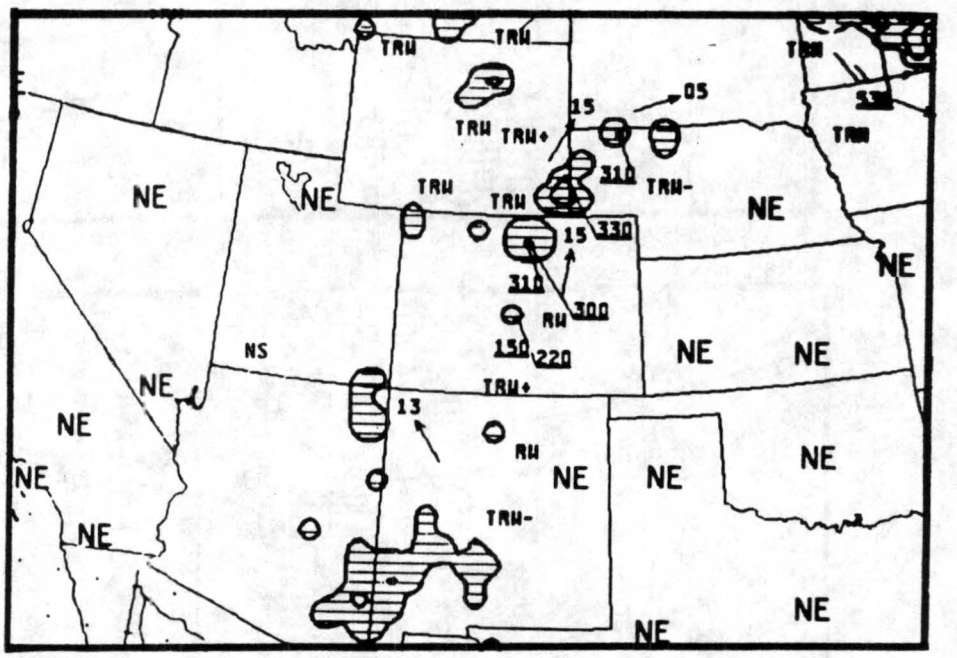

Figure 4.4: Continued.

plots used in the mesoscale analyses cover an 80 km X 80 km area and the CP3 radar (located at Stapleton Airport in Denver) is positioned at the origin of the plots (marked by a plus sign in the figures).

4.2.1 Thermodynamic structure

Figures 4.5 and 4.6 show plots of potential temperature (K) and mixing ratio (g/kg), respectively, for a three hour period (2200-0100 UTC), at one hour intervals. These times were chosen to show the effect of a gust front that moved through the area after 2200 UTC and convective storms (which began after 2330 UTC) on the surrounding environment. The temperatures were fairly constant (with most of the area reporting 323°K, ±1°) and the mixing ratios were relatively high (with 10 g/kg or more observed over the majority of the area) at 2202 UTC. Slightly cooler temperatures began moving into the northwest area at 2257 UTC; however, the mixing ratios remained about the same. One hour later temperatures dropped nearly 10°over some portions of the western area (Figure 4.5c), as a cold pool of air associated with the gust front moved in from the northwest (refer to figure 4.7d). Figure 4.6c reveals that mixing ratios also increased north of CP3 (located at 0,0 km), which coincides with the strongest radar echoes at that time (refer to figure 4.8d). Cooler air Continued to move across the network and the area of maximum mixing ratio values increased by 0057 UTC.

4.2.2 Kinematic structure

The objective analysis of the surface winds from the PAM stations is shown in Figure 4.7a-f. The wind speed and direction are depicted by the direction and length of the wind vectors. Thus, at 1957 UTC (Figure 4.7a), winds were typically from the east with speeds of less than 5 m/s. Two hours later (figure 4.7b) winds over the southern area (especially the southeast) were stronger and from the southeast, while northerly winds were observed in the northwest area of the grid. The changes in wind speed and direction were caused by outflows from storms to the south and northwest of the CINDE network (refer to section 4.1 for more on these storms). One hour later, at 2257 UTC (~1700 MDT), figure 4.7c strong northwesterly winds moved into the northwest area colliding

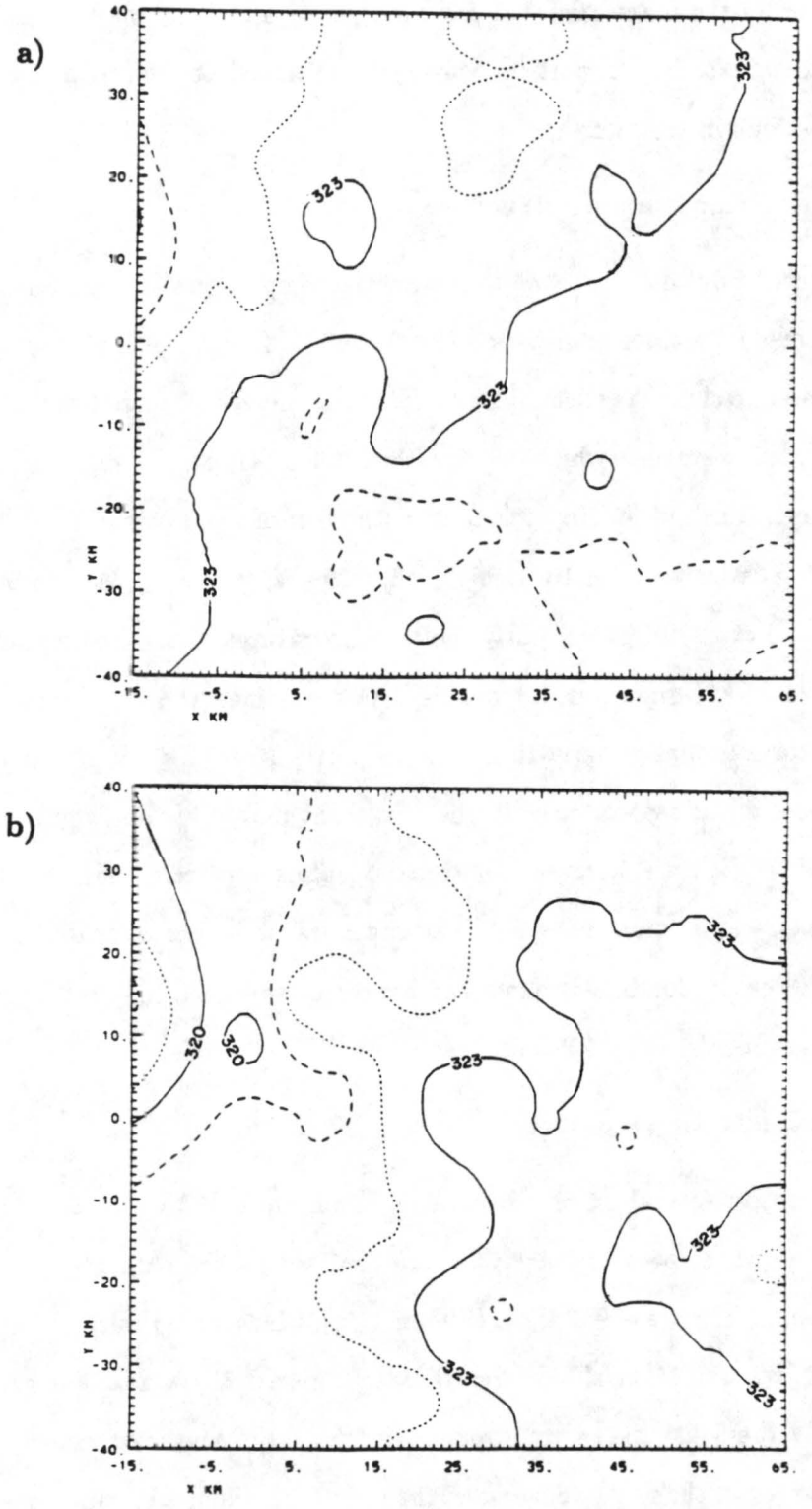

Figure 4.5: Contours of surface potential temperatures from PAM stations for a) 2202 UTC 29 Jul 1987, b) 2257 UTC 29 Jul 1987, c) 2357 UTC 29 Jul 1987 and, d) 0057 UTC 30 Jul 1987.

c)

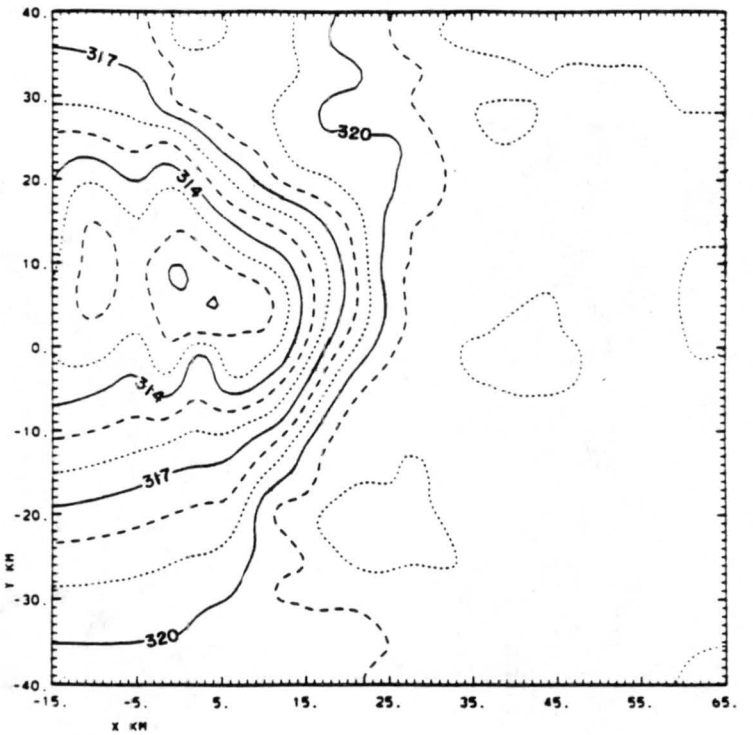

d)

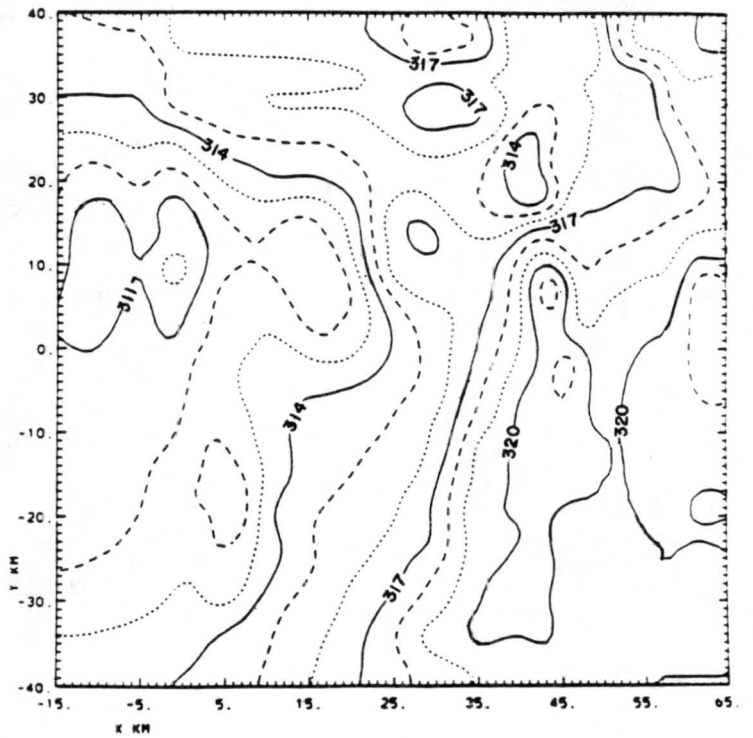

Figure 4.5: Continued.

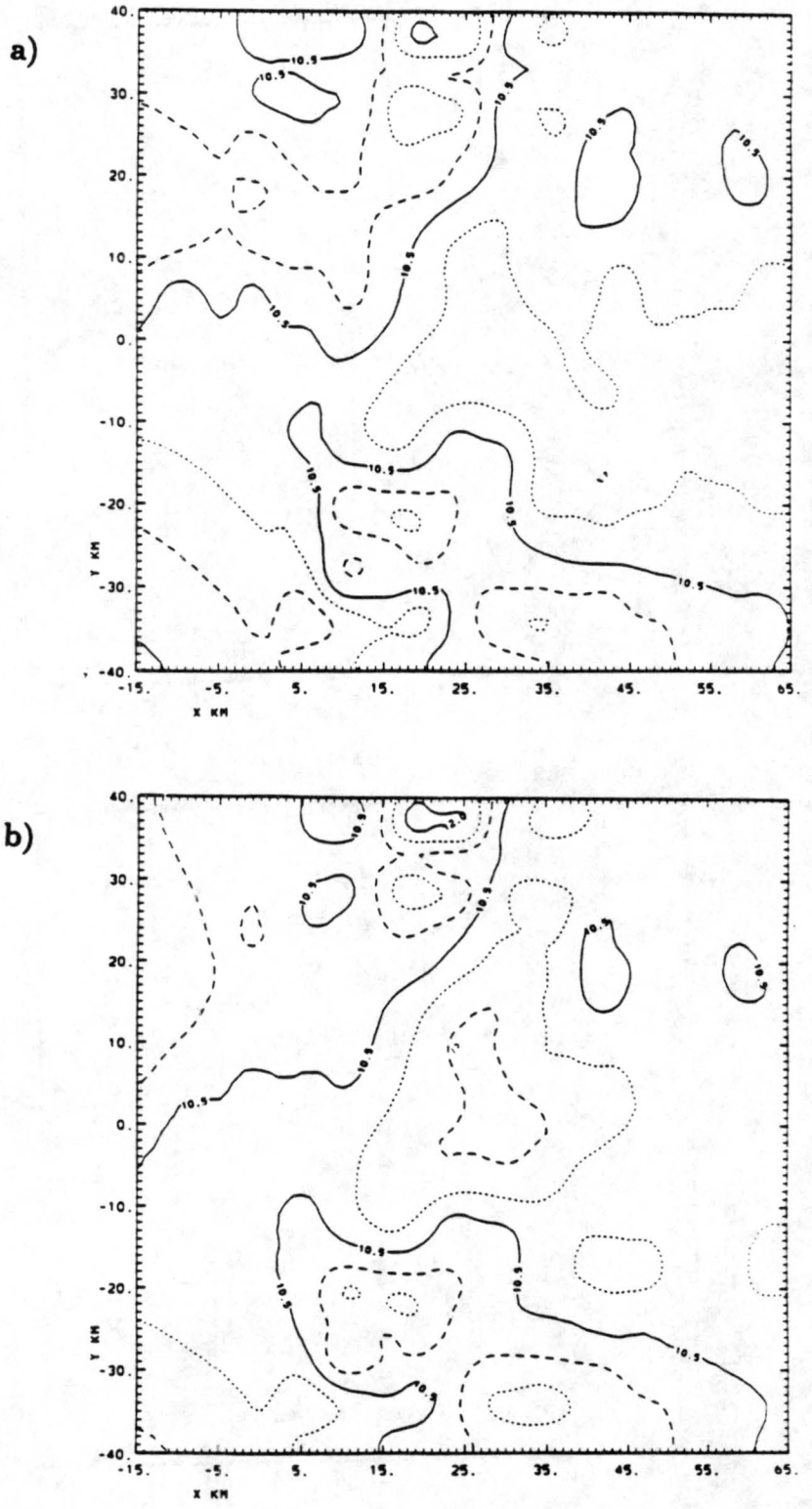

Figure 4.6: Contours of surface mixing ratios from PAM stations for a) 2202 UTC 29 Jul 1987, b) 2257 UTC 29 Jul 1987, c) 2357 UTC 29 Jul 1987 and, d) 0057 UTC 30 Jul 1987.

c)

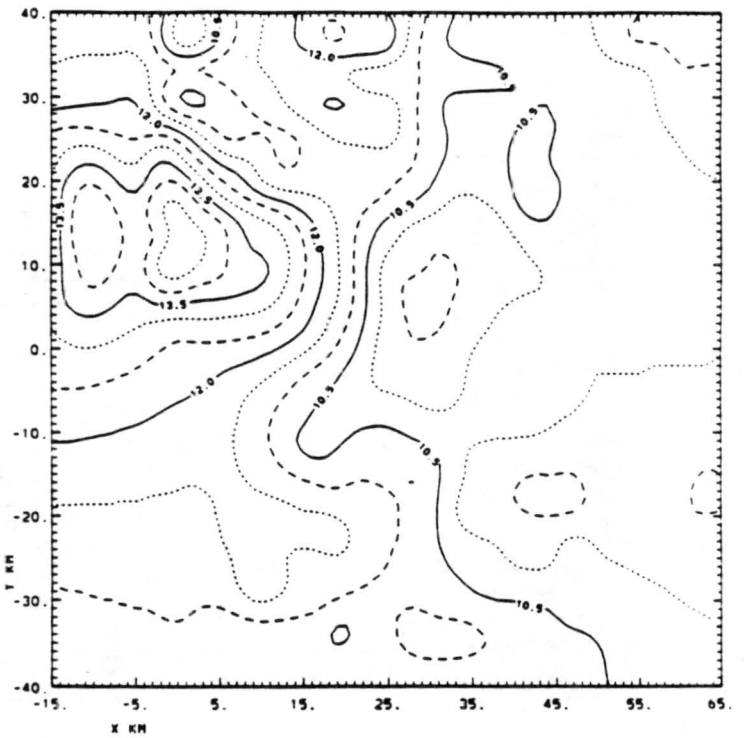

d)

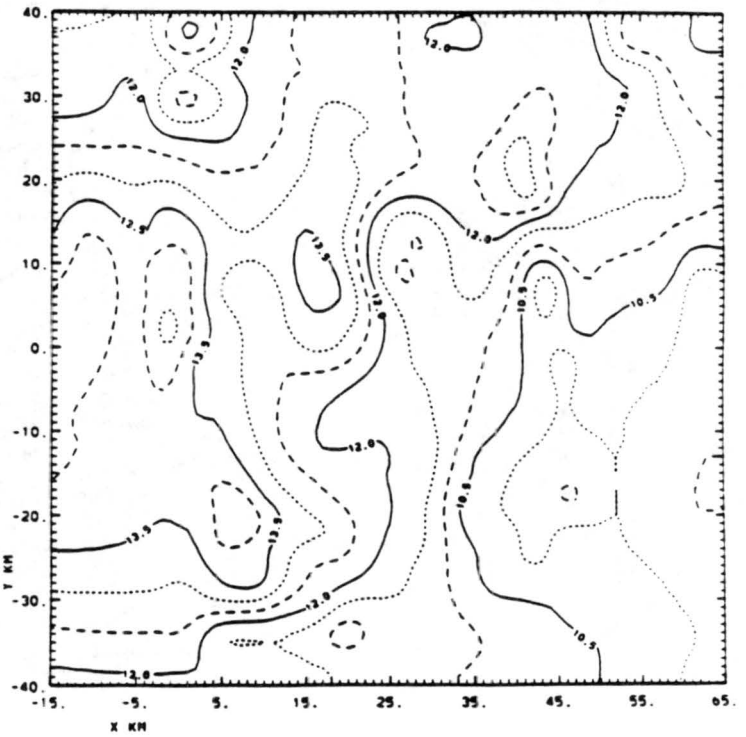

Figure 4.6: Continued.

a)

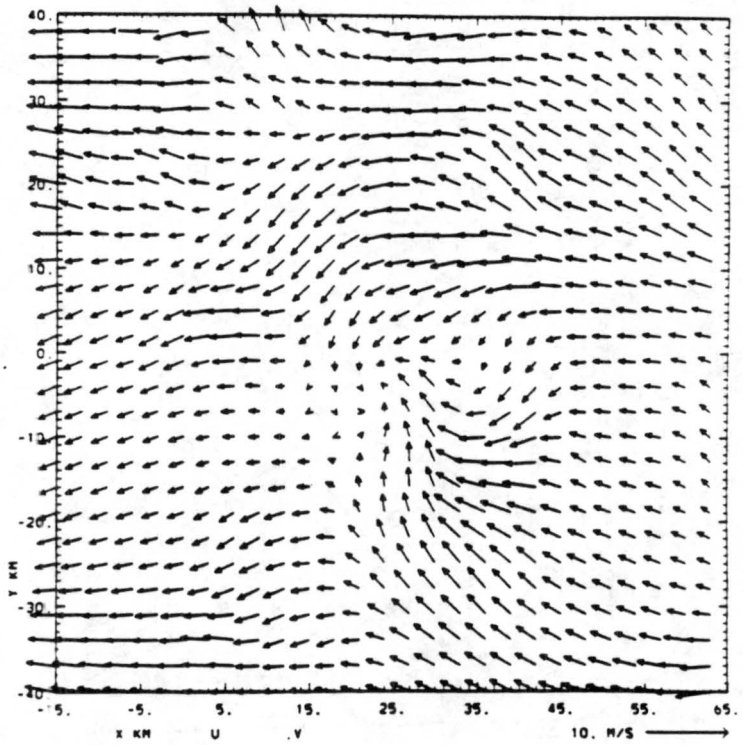

b)

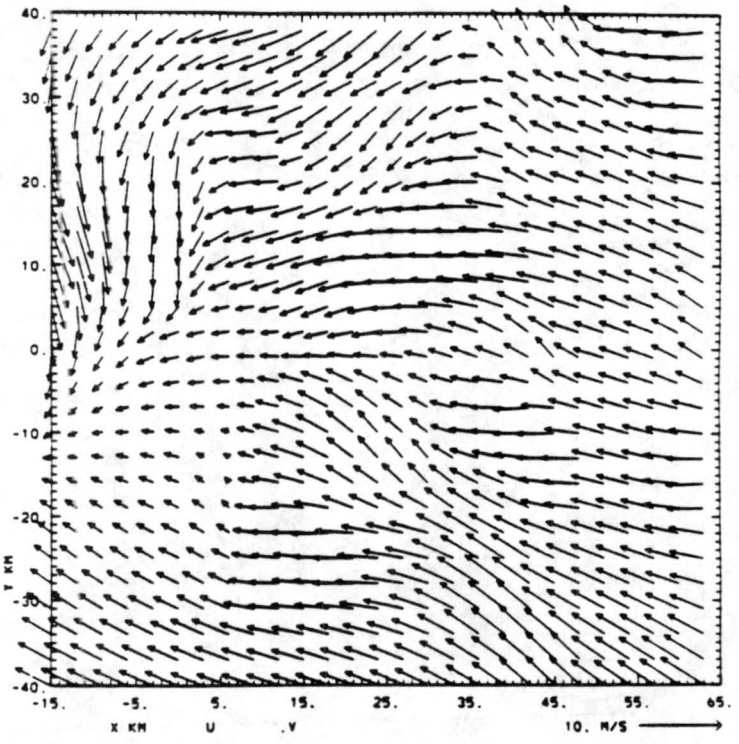

Figure 4.7: Surface wind vectors from PAM stations for a) 1957 UTC 29 Jul 1987, b) 2157 UTC 29 Jul 1987, c) 2257 UTC 29 Jul 1987, d) 2357 UTC 29 Jul 1987, e) 0057 UTC 30 Jul 1987 and, f) 0157 UTC 30 Jul 1987.

c)

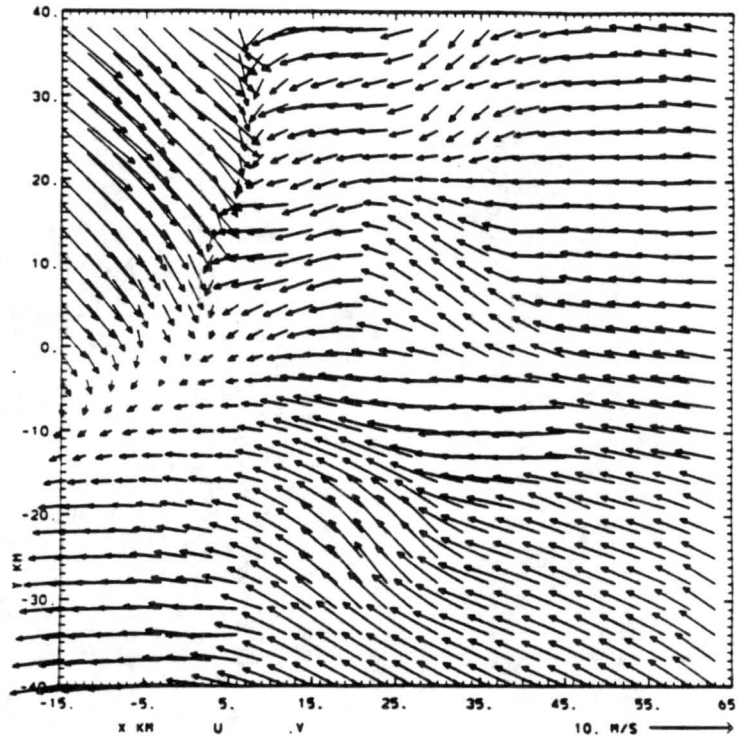

d)

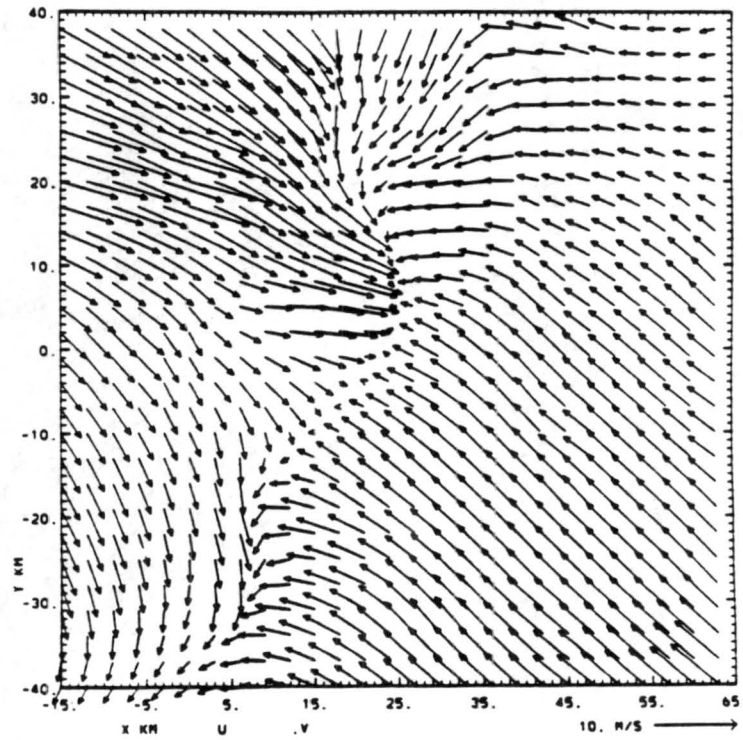

Figure 4.7: Continued.

e)

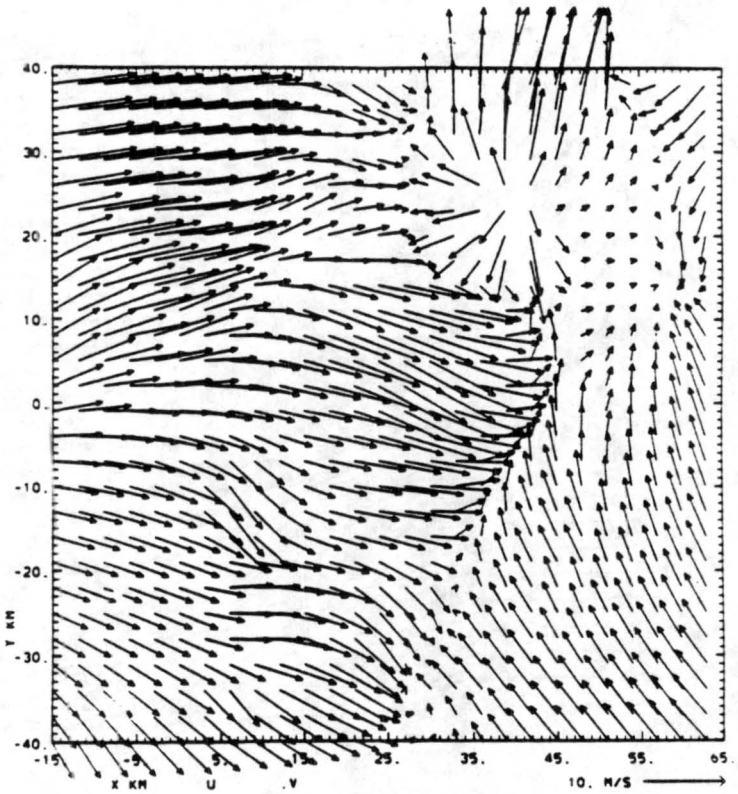

f)

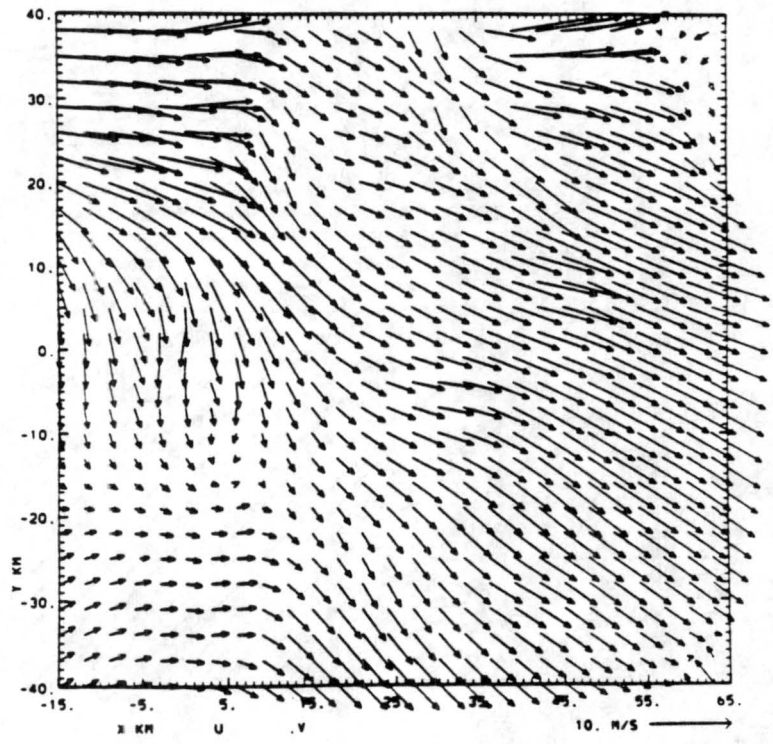

Figure 4.7: Continued.

with easterly winds in the northeast and southeasterly winds in the southeast, creating a northeast to southwest convergence line. This convergence line strengthened and moved in a southeast direction over the next two hours (as shown in figures 4.7d and e). However, by 0057 UTC an area of strong divergence was also observed in the northeast corner of the grid. Northwest winds dominated the area by 0157 UTC (figure 4.7f), indicating that the strongest gust front (which was the one associated with the storm northwest of the network) had moved through the area.

4.2.3 Radar

Radar reflectivity patterns from CP3 were used to reveal a detailed look at the mesoscale convective precipitation patterns over the area of interest. The 5.5°surveillance scans were contoured at 35 and approximately 50 dBZ and covered a 120 km X 120 km area (which includes the 80 X 80 grid used to examine the surface mesonet data).

Radar echoes were not detected within the smaller grid until 1630 MDT (figure 4.8a), when a storm developed over the NOAA D radar (located ~10 km east of CP3). Figure 4.8b reveals that thirty minutes later this storm had reached it's most intense stage and was starting to dissipate, as it moved to the north. A new storm was also developing over the CP3 radar at this time (1700 MDT). The storm that originated over the NOAA D radar had completely dissipated by 1730 MDT, while the other storm continued to grow (in both intensity and areal extent) as it moved to the north. At 1800 MDT, the reflectivity pattern showed smaller, fragmented areas of echoes greater than 50 dBZ but areas containing echoes between 35 and 50 dBZ had increased. Note that the echoes south of CP3 were associated with another storm moving in from the southwest. The radar echoes became less intense and more disorganized after 1830 MDT and by 1900 MDT the storms started to dissipate as they moved to the north.

4.3 Precipitation Rates

Precipitation rates play an important role in this study because in addition to providing the researcher with information regarding the mesoscale features of the storm (for example, the storm's location, the intensity of the storm at certain times, etc.), it is used

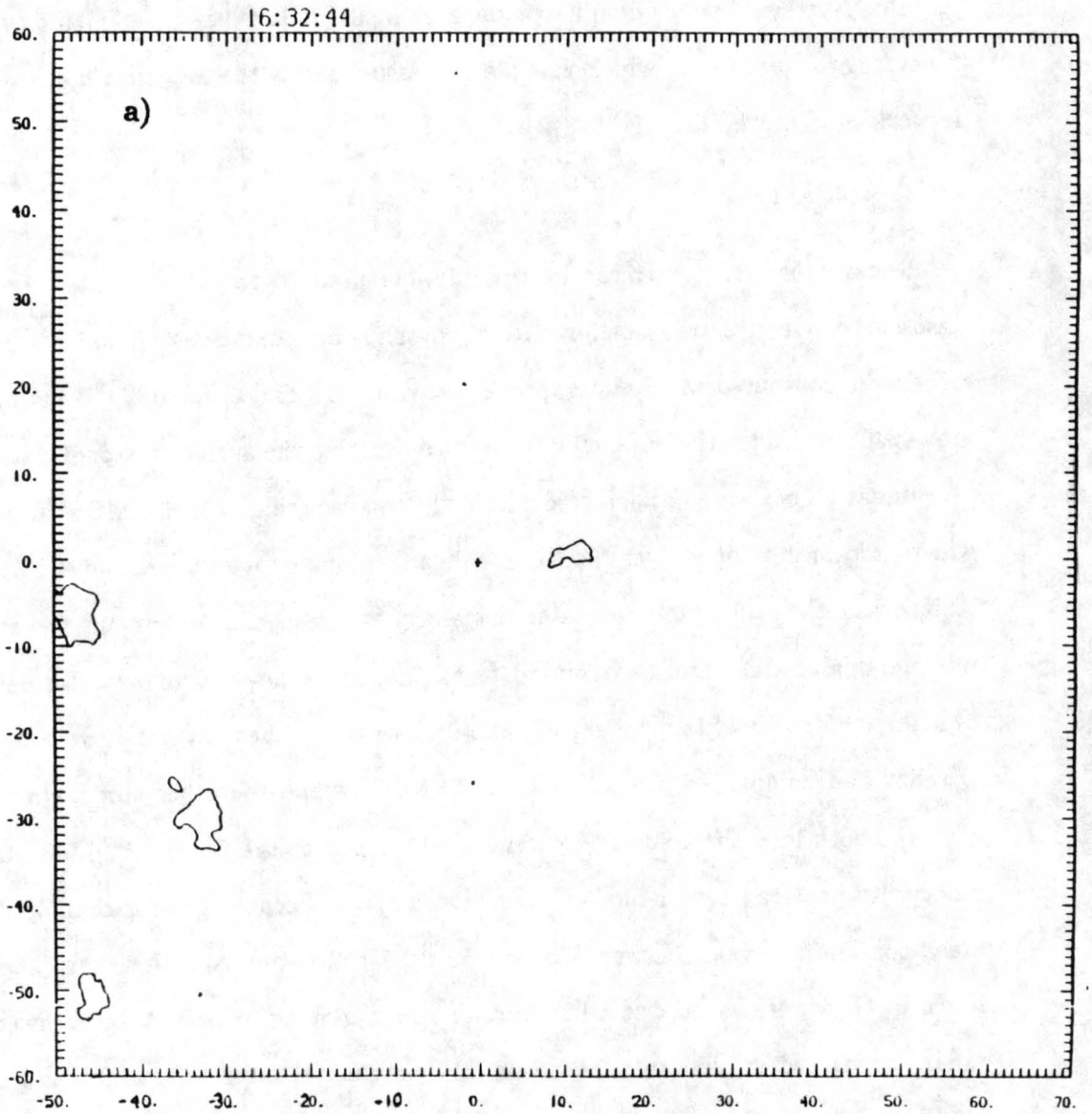

Figure 4.8: 5.5°surveillance scans from CP3 radar with reflectivity contours at 35 and 50 dBZ for an 120 km X 120 km area for a) 1632 MDT (or 2232 UTC), b) 1659 MDT, c) 1732 MDT, d) 1800 MDT, e) 1829 MDT and, f) 1902 MDT on 29 July.

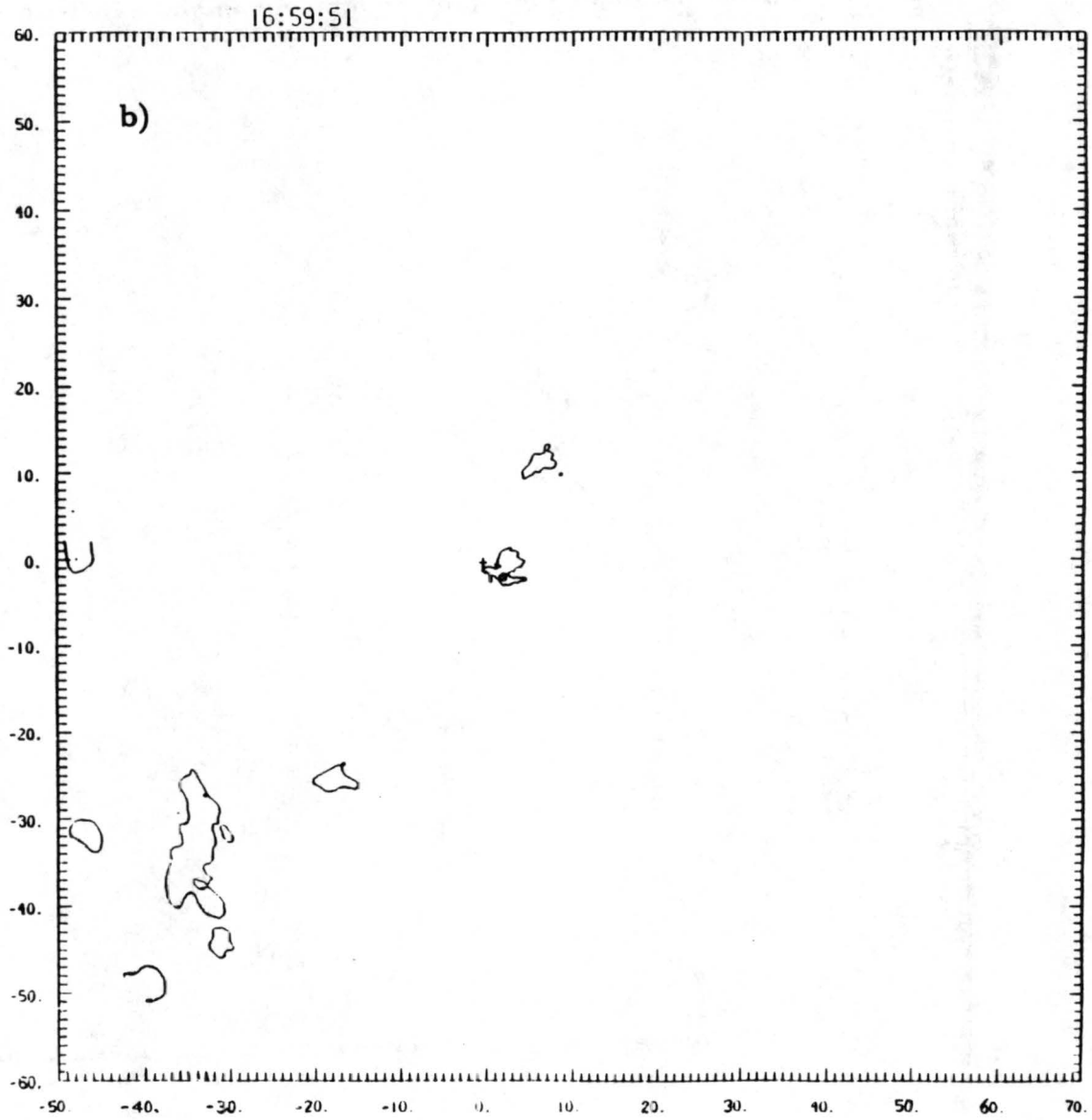

Figure 4.8: Continued.

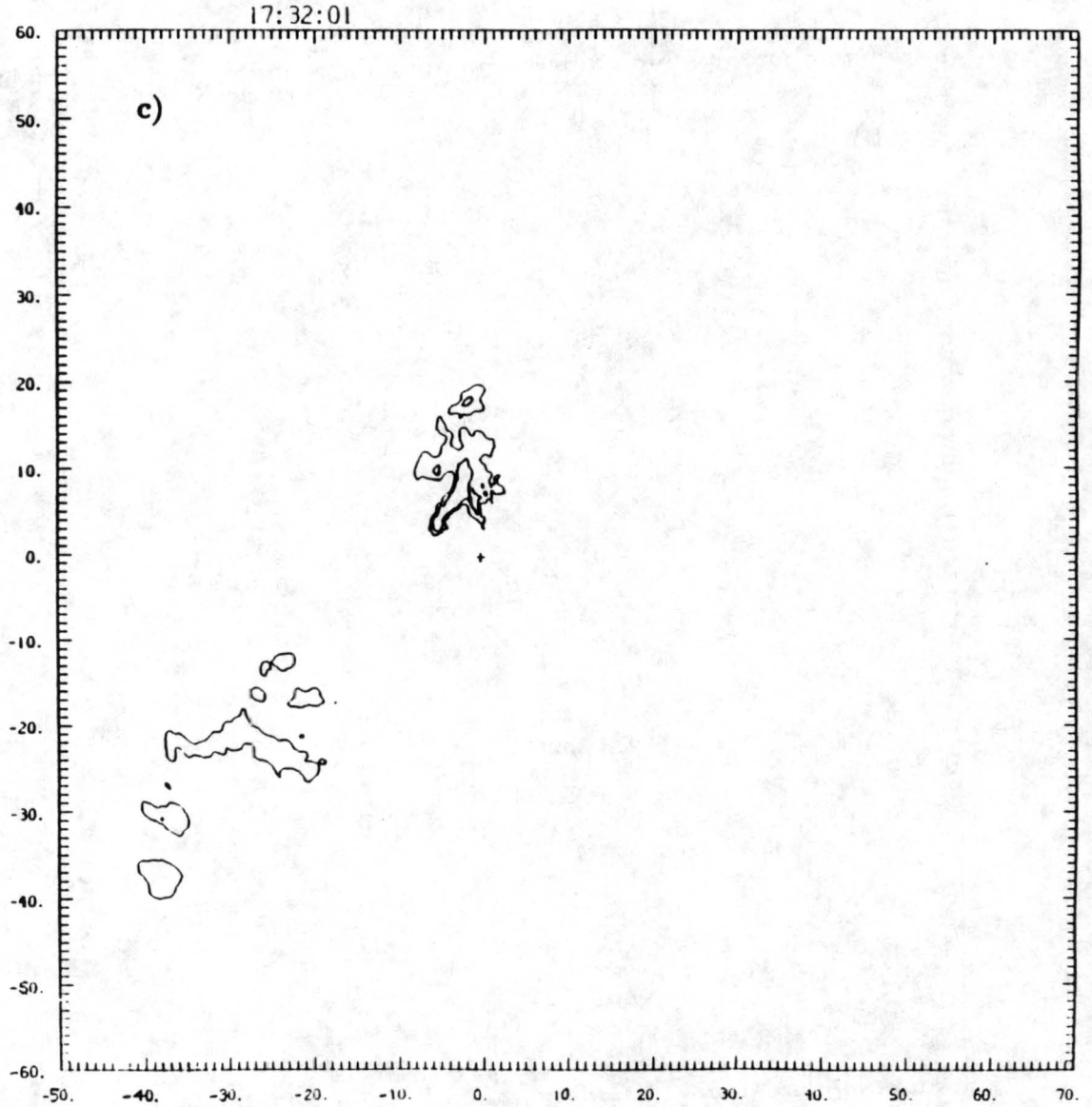

Figure 4.8: Continued.

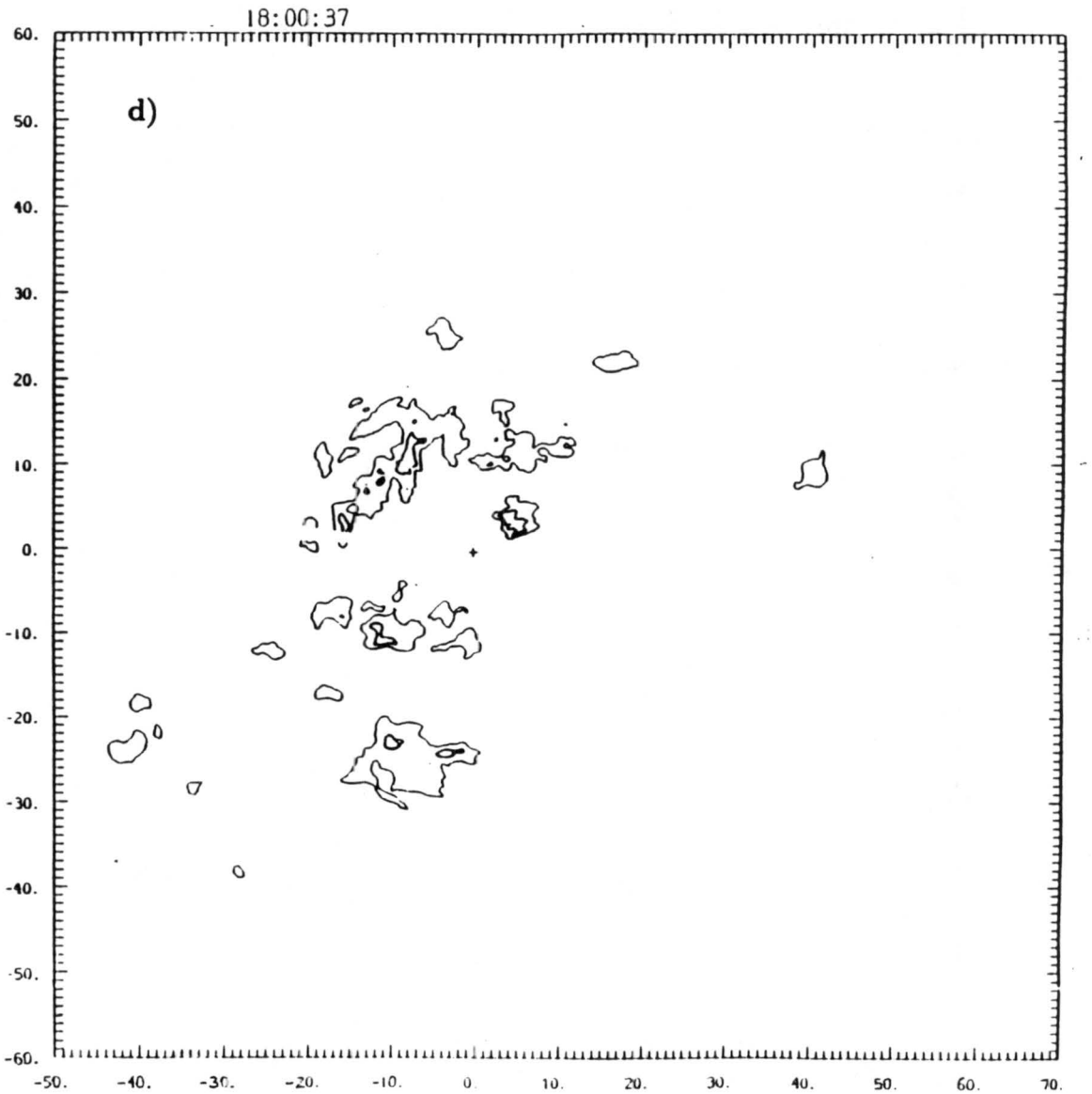

Figure 4.8: Continued.

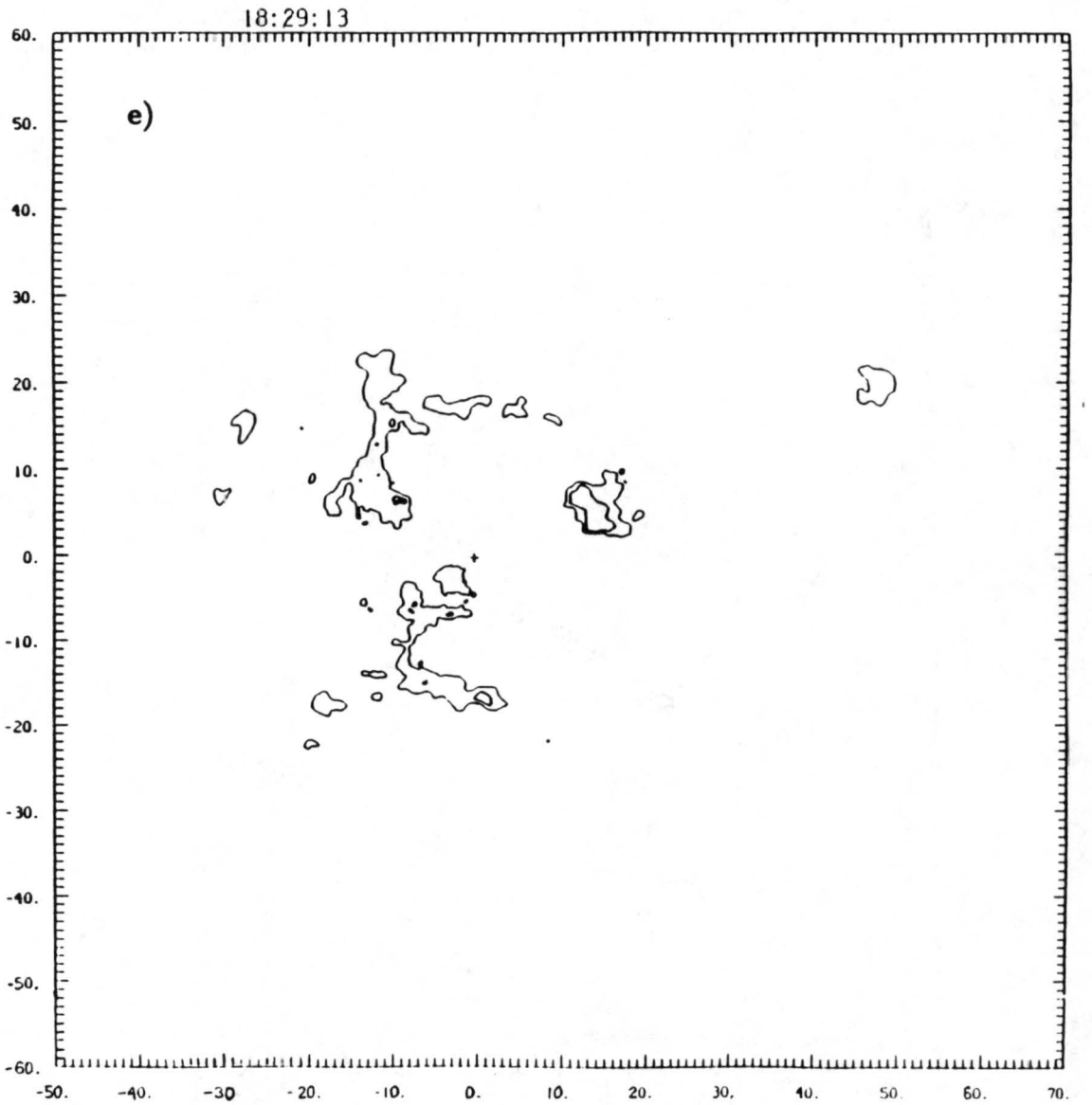

Figure 4.8: Continued.

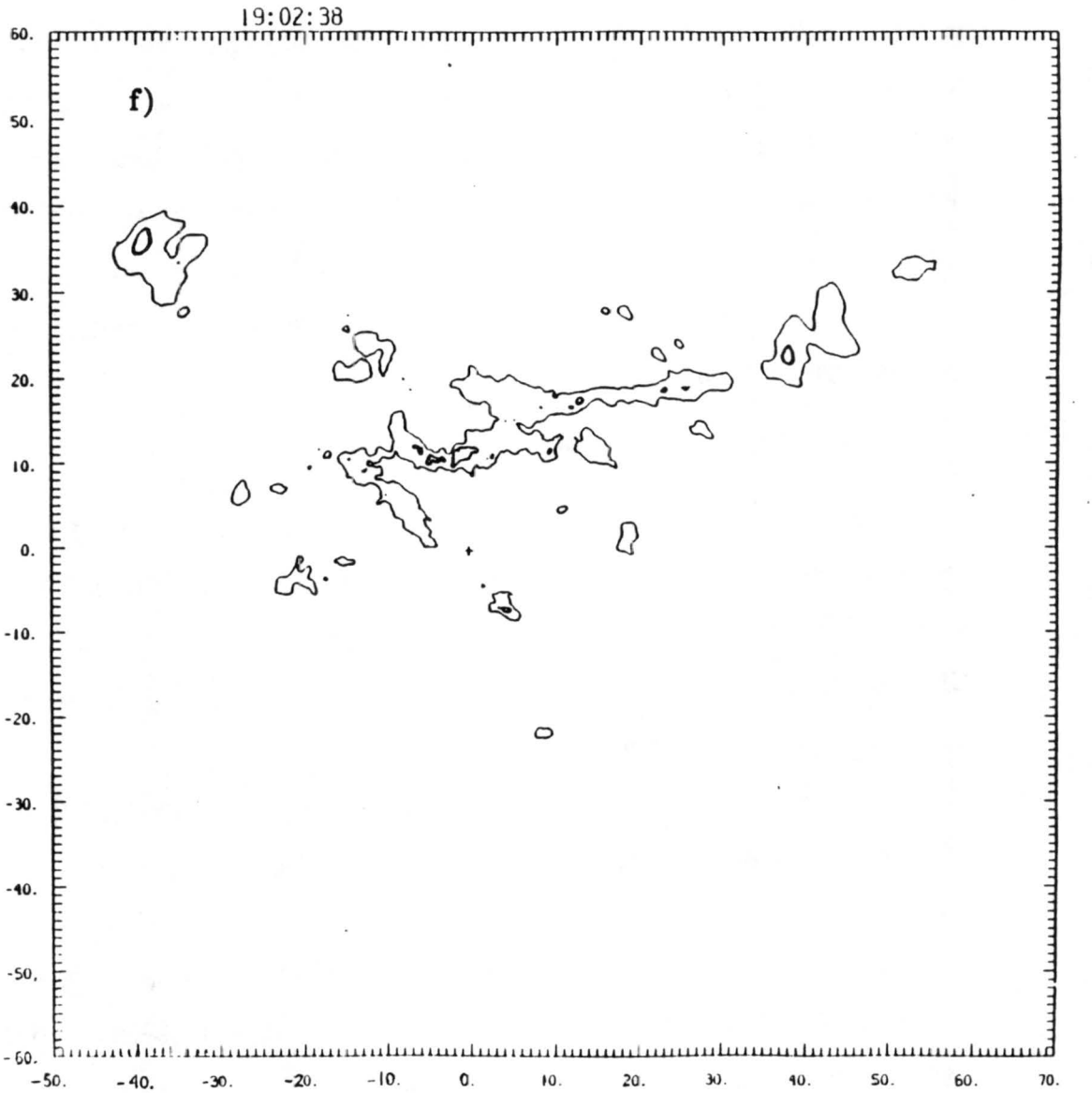

Figure 4.8: Continued.

as a tool to guide the model's release of convective heating rates, for selected runs, which employ a modified version of the RAMS convective parameterization scheme. A description of the modified convective parameterization scheme, along with an explanation of how the estimated rain rates are utilized, is given in section 5.3.

The precipitation rates are estimated from surface PAM data and the CP3 doppler radar. In both cases data are collected over a 30 km X 30 km area, since the fine grid spacing in the model is ~28 km. Hence, data collected over an area smaller than this could possibly not be represented in the model run and since the storm was never much larger than 30 km X 30 km, this was considered a good representative area. The rainfall rates obtained over this area were then applied to a larger area, based on the NWS radar summary maps. These rainfall rates were used to drive the modified convective parameterization scheme.

4.3.1 Mesonet data estimates

Figure 4.9 contains plots of 60 minute averages of rainfall (from PAM data) for times ending at 0000, 0100 and 0200 UTC 30 July. The amount of rain that fell from 2300 - 0000 UTC (Figure 4.9a) shows a maximum amount, of 13.2 mm, 10 km northeast of the CP3 radar (located at 0, 0 km). Over the next hour the amount of rainfall had decreased significantly (5.3 mm maximum) and the maximum amount was now located ~10 km east of the previous maximum location. The next one hour period, 0100-0200 UTC (which was not included in the precipitation rate calculation), shows that peak rainfall values had shifted back to the northwest, with a value of 10.6 mm.

The accumulated rainfall amount (in mm) for each 60 minute period (beginning at 7/29/87 2300 and ending at 7/30/87 0100 UTC) was obtained from individual PAM stations over a 30 km X 30 km area of the mesonetwork (extending from -20 to 10 km along the x-axis and 0 to 30 km along the y-axis); thus, providing an hourly rainfall rate (mm/hr). Although the storm was still quite intense after 0100 and PAM data was still available, this time period was chosen to coincide with the radar data which ended at approximately 0100 UTC. Area averaged rainfall rates, for each hour, were then obtained

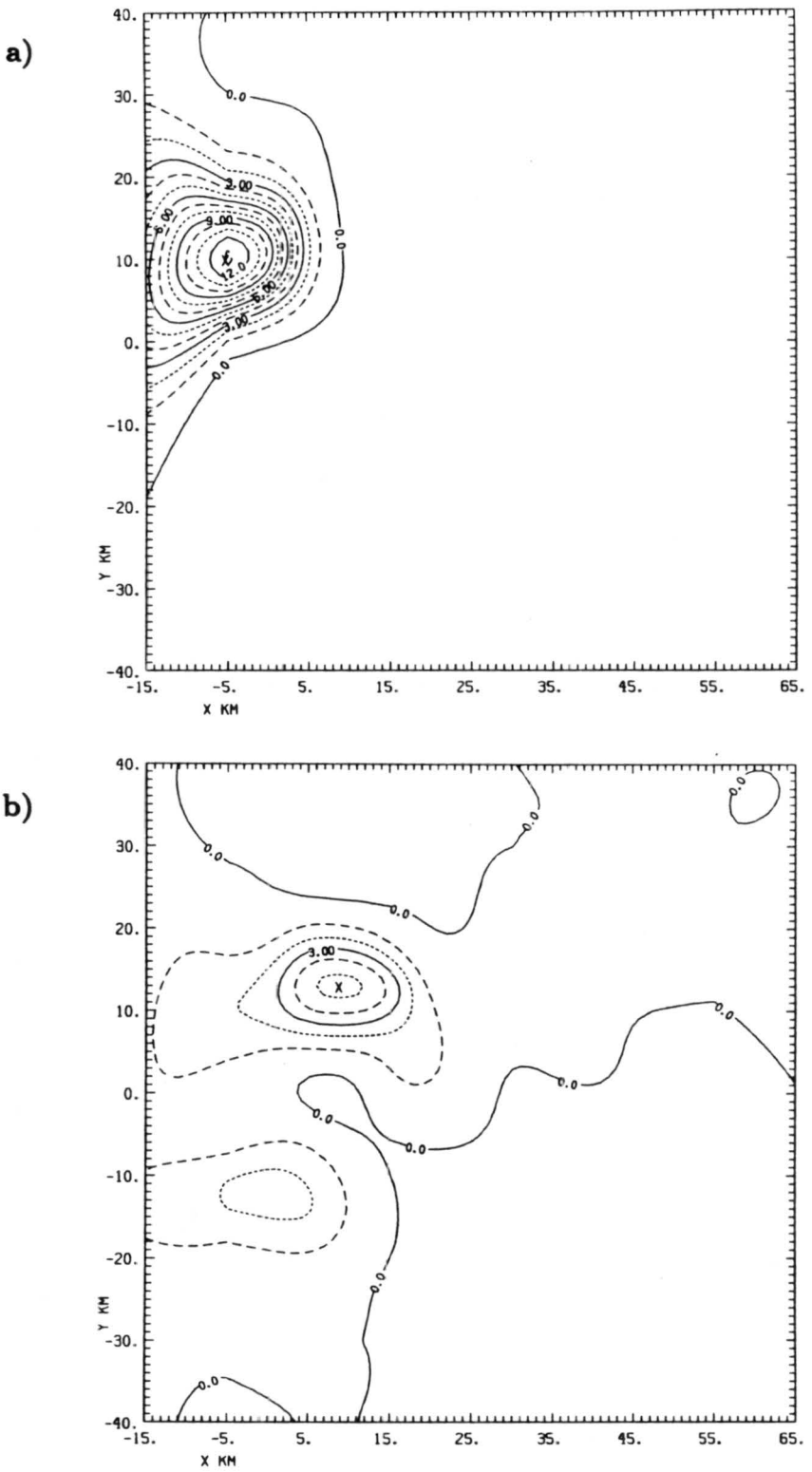

Figure 4.9: Hourly averages of rainfall, from PAM data, for times ending at a) 0000 UTC, b) 0100 UTC and, c) 0200 UTC on 30 July.

c)

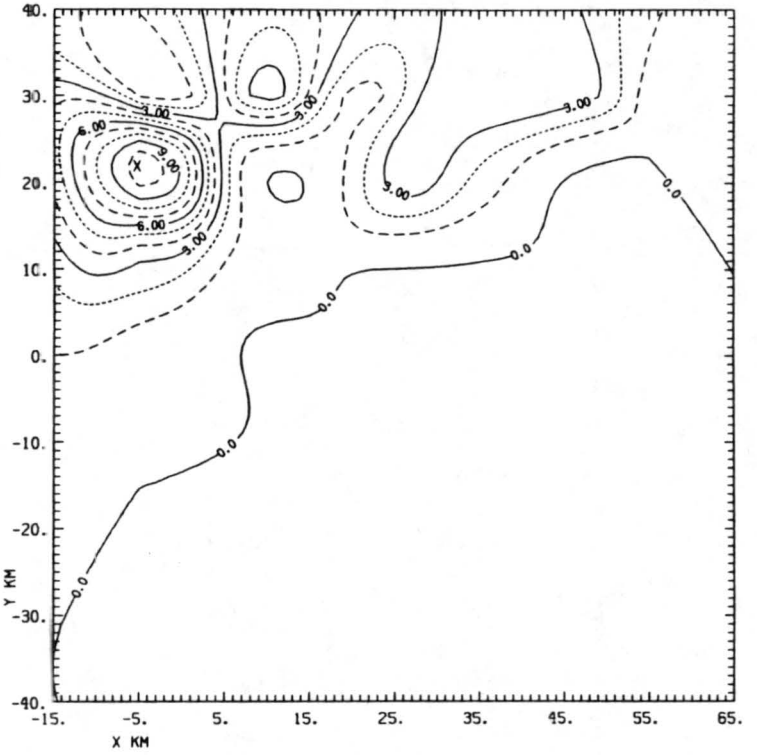

Figure 4.9: Continued.

by averaging all of the individual rain rates within the area over each one hour time period. The area averaged rainfall rates for each hour were then averaged over the two hour period to obtain a single, average rainfall rate value of 2.3 mm/hr.

The estimated average rainfall rate of 2.3 mm/hr is small compared to the 15 mm of rain that was measured at one of the stations over the two hour time period – or an average of 6 mm/hr (a total of 18.04 mm fell over that station). This is a good example of the variability in convective rainfall and explains why more than one station was considered when obtaining the average.

4.3.2 Radar estimates

Multiparameter radars can give improved rain rate estimates (refer to chapter 2); however, mature algorithms were not available for this research. Thus, the single-parameter CP3 radar was used to obtain estimates of precipitation rates. Two different reflectivity-rainfall (Z-R) relationships were used in this study. One was the familiar Marshall-Palmer (1948) relationship ($Z = 200R^{1.6}$), considered to be applicable to general rainfall conditions. The other relationship, $Z = 447R^{1.44}$ (developed by Fankhauser, 1988), was an average of six Z-R relationships, including the Marshall-Palmer relationship just mentioned. The other relationships include the CCOPE-80181 relation ($Z = 1452R^{1.2}$), derived from data observed beneath an intense squall line with relatively high cloud bases. The Martner (1975) relation ($Z = 615R^{1.41}$), based on thunderstorms in northeastern Colorado. The $Z = 155R^{1.88}$ relation developed by Smith et al. (1975) for North Dakota thunderstorms that had a high frequency of hail (presumably accounting for the relatively large exponent on R). The combined CCOPE data ($Z = 590R^{1.33}$) included a mix of the 01 August 1981 squall line measurements and two other days which had lower cloud bases, more stratiform rainfall and were somewhat less convective in nature. The Jones (1955) relation ($Z = 486R^{1.37}$) derived for continental thunderstorms in Illinois. The Fankhauser relationship was developed since direct correlations between rainfall measured at the ground and reflectivity aloft were found to be storm dependent, thus, there was no a priori justification for choosing one Z-R relation over another.

Several empirical studies (Geotis, 1963; Dennis et al., 1971; Barge, 1974; Waldvogel and Federer, 1976; and Dye and Martner, 1978) comparing surface measurements with radar backscatter from convective storms indicate that whenever radar reflectivity factor reaches or exceeds the range of 50 to 55 dBZ over significant time and space intervals, there is a high probability that hail will be observed in the surface precipitation. Consequently, an upper threshold value of 50 dBZ was set in evaluating the associated rain rate and any observed reflectivity that exceeded this value was assigned to the value of the upper threshold.

Figure 4.10 (taken from Fankhauser, 1988) shows that log Z values between 2 and 3 typically lead to rain rates of < 1 mm/hr. Thus, reflectivities less than 20 to 30 dBZ, contribute only a small fraction to the overall radar reflectivity. Using an average of these numbers, only reflectivities greater than 25 dBZ were used to obtain the rain rate estimates in this study.

Applying an upper threshold of 50 dBZ and using reflectivities that are greater than the 25 dBZ, rain rates were computed at an elevation of 2.5 km (which is $\sim$1000 m above the ground) over the same 30 km X 30 km area used to get estimates from the surface data. This height was chosen to insure consistent, uninterrupted radar histories as storms moved away from the radar, although, it would have been more desirable to use radar scans closer to the ground, to minimize the effect of evaporation in the subcloud layer. A single value rainfall rate (in mm/hr) was obtained by averaging the rain rates computed for each volume scan at 2.5 km over a two hour time period (2300 - 0100 UTC).

The above procedure produced rain rates of 7.1 mm/hr (using the combined Z-R relationship of $Z = 447R^{1.44}$) and 11.4 mm/hr (using the Marshall-Palmer relationship).

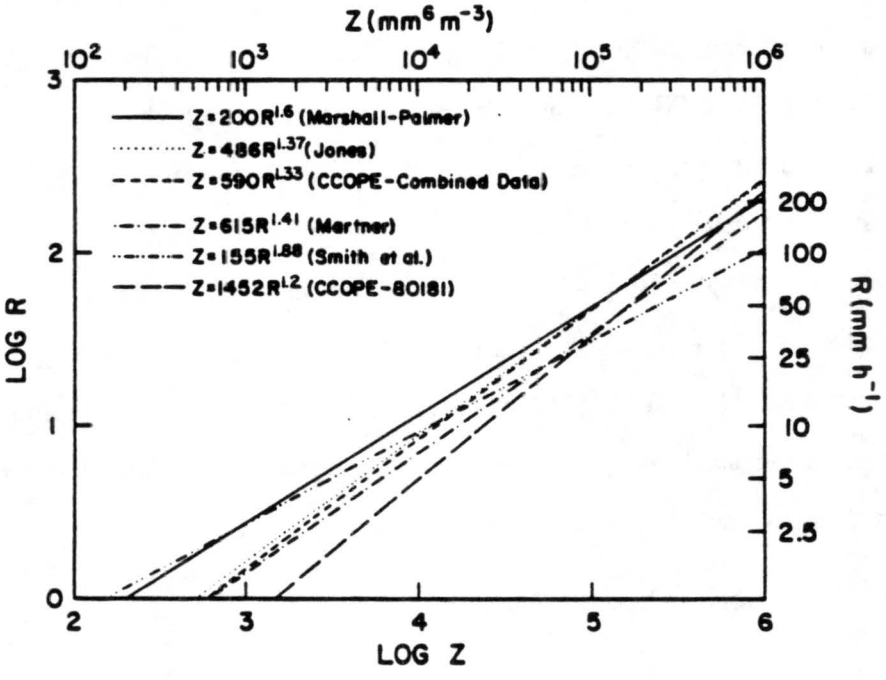

Figure 4.10: Plots of various radar reflectivity (Z) versus rain rate (R) relationships as identified in the upper left corner. (This figure is taken from Fankhauser, 1988).

Chapter 5

EXPERIMENTAL DESIGN

The intent of this thesis is to examine the feasibility of producing improved, short-range quantitative precipitation forecasts (QPF) for convective storms by forcing latent-heat (derived from rain rates) to be released in select areas. This will be accomplished by attempting to simulate the conditions associated with localized ordinary thunderstorms in the Denver area on 29 July 1987 with the Regional Atmospheric Modeling System, RAMS, developed at CSU. The model's accuracy in predicting these conditions, especially the precipitation, will determine the feasibility of this method. However, it should be noted that some discrepancy in the modelled output could be the result of the grid spacing, which may not adequately resolve the convective storm nor the mesoscale circulation driven by local terrain and other surface forcing features. This chapter will briefly describe the numerical model and discuss the initialization procedure, the numerical experiments used in this study and the methods used to obtain the estimated precipitation rates from surface mesonet data and doppler radar.

5.1 Numerical Model Description

The numerical model employed in this study is the Regional Atmospheric Modelling System (RAMS) developed at CSU; which evolved from the merger of the CSU cloud/mesoscale model (Tripoli and Cotton, 1980 and 1982) and a hydrostatic mesoscale model (Mahrer and Pielke, 1977). The basic structure of the model is described in Tripoli and Cotton (1982), Cotton et al. (1982), Tremback et al. (1985), Tripoli (1986), and Tremback (1990). Refer to Appendix A for a general description of RAMS.

The nonhydrostatic model configuration used in this study is as follows. The vertical structure of the grid uses a terrain-following sigma-z coordinate system (Gal-Chen and

Somerville, 1975a,b; Clark, 1977). Radiative lateral boundary conditions are employed following Klemp and Wilhelmson (1978 a,b). The Tremback and Kessler (1985) surface layer and soil model parameterizations are used for the lower boundary condition, and a rigid lid is used for the upper boundary condition. Although this "wall on top" top boundary condition (e.g. w is set to zero at the model top) is the only choice available in the nonhydrostatic model when using variable initialization, there is some concern with this selection. The rigid lid top boundary condition can cause strong reflection of upwardly propagating gravity waves, turning them downward back into the model domain and a Rayleigh friction absorbing layer (which is used in the upper layers of the model to absorb gravity waves approaching the lid, sufficiently damping them before and after reflection so that they are effectively eliminated) was not used. The Rayleigh friction absorbing layer was not included because all of the simulations in this thesis used a variable initialization and prognostic fields which are not initialized horizontally homogeneously cannot sensibly be forced toward a horizontally homogeneous state. However, it should be mentioned that Cram (1990) modified the Rayleigh friction scheme for a prefrontal squall line study but this approach is computationally expensive, and moreover, Heckman (1991) found that it had little impact in his application of the technique to simulating cirrus clouds. The longwave and shortwave radiation parameterizations described by Chen and Cotton (1983) are also used in these simulations. The full microphysical parameterization scheme is activated in all experiments allowing the model to be influenced by liquid and ice phase precipitation processes. A simplified Kuo-type convective parameterization is used (Kuo, 1974); with the convective parameterization scheme described in detail by Tremback (1990). However, modifications to the convective parameterization scheme are used for some of the experiments, to allow the model's heating rates to be determined from estimated rain rates in certain areas. Modifications to the convective parameterization scheme will be discussed later in this chapter.

5.2 Model Initialization

RAMS includes an assimilation package which enables data from the National Meteorological Center (NMC) and individual rawinsonde soundings to provide nonhomoge-

neous fields for initializing the model. The simulations presented in this study used these datasets, which are archived at NCAR. The assimilation includes a mesoscale isentropic data analysis package which is utilized to convert the data to isentropic coordinates. A Barnes (1973) objective analysis scheme is then used to assimilate the data onto the coarse model grid and these data are then used as a variable initialization to start the model.

The three-dimensional simulations conducted in this study contain one nested grid. The coarse grid has 30 grid points in both the x and y-directions with a grid spacing of 1.3°and 1.0°, respectively. Thus, the horizontal area, which covers the majority of the United States, ranges from 125 W to 87.3 W and 24 N to 53 N. The fine grid has a nesting ratio of 4:1; so at 40 N, where the latitude/longitude grid spacing is approximately the same, the coarse grid horizontal spacing is ~111 km and the fine grid spacing is ~28 km. A finer grid spacing of ~8-10 km would have been more desirable for predicting the small scale CINDE thunderstorm, but this is too fine for use of the Kuo scheme. A new scheme developed by Weissbluth (1991), intended for these scales, is being implemented in RAMS but was unavailable for this research. The geographical location of the coarse and fine grid model domains are shown in Figures 5.1a and b. The vertical grid spacing varies from 200 m in the lowest levels to 500 m at 3.937 km. The vertical resolution remains constant, at 500 m, from 3.937 to 18.437 km (the top level of the model domain). The same vertical grid spacing is applied to the coarse and fine grids with 42 grid points used in both.

5.3 Modified Cumulus Parameterization Scheme

Modifications were made to the RAMS cumulus parameterization scheme to allow the insertion of inferred heating rates, over a specified area, from estimated rainfall rates for certain experiments. The procedure utilized to implement the modified cumulus parameterization scheme is as follows. Individual rainfall rates were estimated from PAM and radar data (refer to previous chapter) over the CINDE area. The "locally-calibrated" single value rainfall rates are then used in the modified cumulus parameterization scheme,

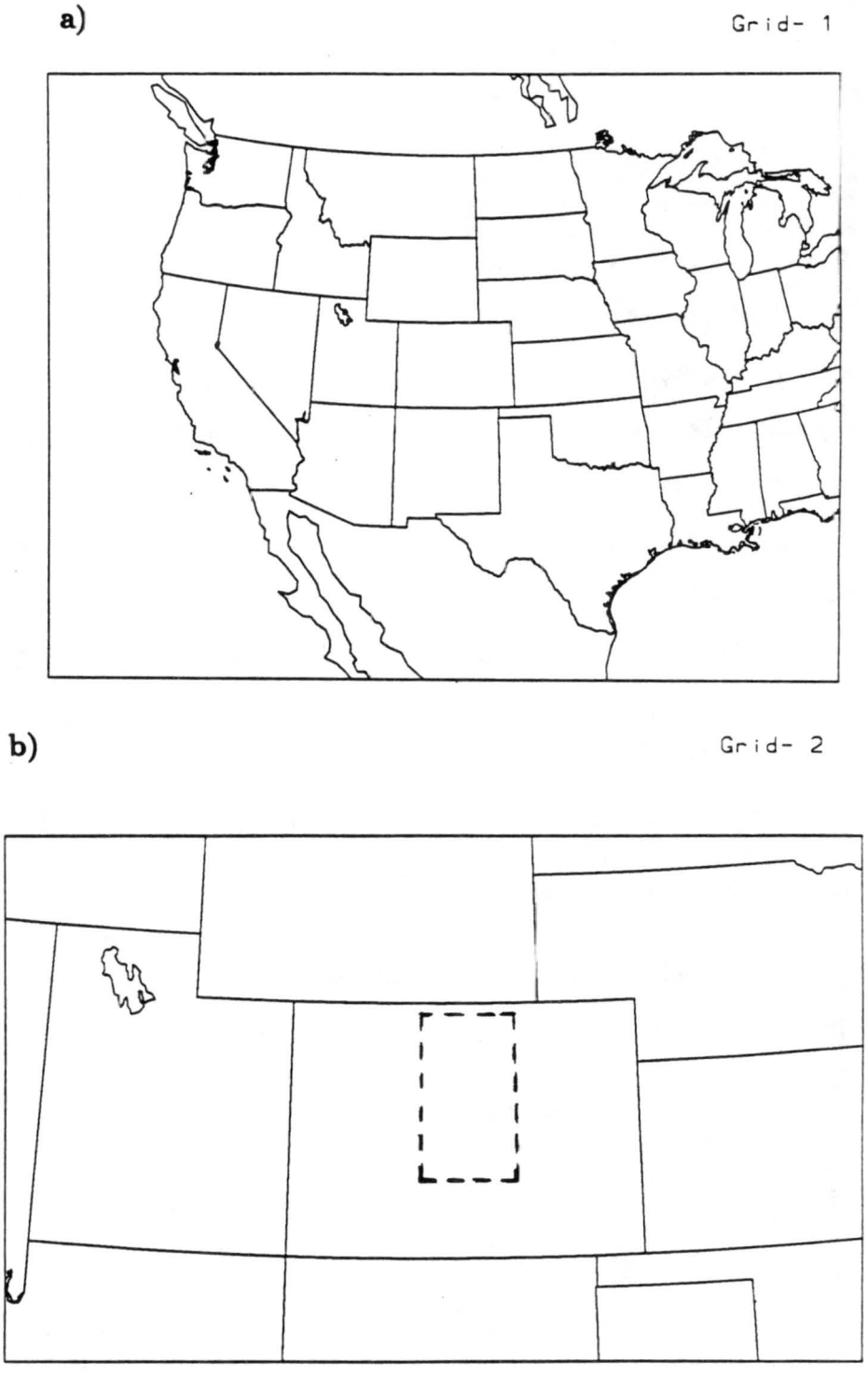

Figure 5.1: Geographical location of the a) coarse grid (Grid 1) and b) fine grid (Grid 2) model domains. The dashed box in the Colorado fine grid represents the area over which the modified cumulus parameterization scheme is applied.

applied over the area represented by the dashed boxed in Colorado (Figure 5.1b) whose dimensions are based upon the 2035 UTC radar summary map shown in Figure 4.4c. This estimate of the three-dimensional latent-heating field (over the specified area and time period), is used in the model's thermodynamic equation in an attempt to drive the model atmosphere toward the observed state. The prescribed latent heating rate that results from the convection is distributed in the vertical by a parabolic profile (Figure 5.2). The parabolic profile is based on vertical profiles of convective heating for extratropical convective systems shown in the study by Kuo and Anthes (1984). The upper and lower bounds of the profile correspond to cloud top and cloud base heights, and the maximum value is positioned at mid-cloud level.

In the experiments that utilized the modified parameterization scheme, only fine grid data over north central Colorado was changed; other areas used the existing Kuo-type cumulus parameterization scheme. The forced heating was applied during a one hour time integration period of 2000-2100 UTC since the area affected by the modified version of the cumulus scheme was based on the 2035 UTC radar summary map. After 2100 UTC , the time integration proceeded with the model's own physical processes.

5.4 Numerical Experiments

Five numerical experiments, in addition to the control run, are conducted in this study to determine whether improved, short-range precipitation forecasts can be obtained

Table 5.1: Brief Description of Numerical Experiments

Experiment	Total Time	Time Interval (UTC)	Forced Heating	Method of Estimating Rain Rate
Control Run	0 hr	(7/30 0000)	no	n/a
1	24 hr	(7/29 0000 – 7/30 0000)	no	n/a
2	12 hr	(7/29 1200 – 7/30 0000)	no	n/a
3	12 hr	(7/29 1200 – 7/30 0000)	yes	rain guage date
4	12 hr	(7/29 1200 – 7/30 0000)	yes	radar (using $Z=447R^{1.44}$)
5	12 hr	(7/29 1200 – 7/30 0000)	yes	radar (using $Z=200R^{1.6}$)

from the RAMS model using diabatic initialization. Table 5.1 provides a brief description of all the experiments. Cumulus convection and microphysical parameterization schemes

are common to all experiments. Conversely, the initialization time, forced latent heating (inferred from precipitation rates), or precipitation rates are variables that varied from one experiment to the next. The numerical experiments were designed to investigate the following: how much the model is affected by the spin-up problem; examine the possibility of producing better QPFs using inferred heating rates, based on observed precipitation rates, to guide the model to a more desirable state; and determine the sensitivity of the model to different estimates of rain rates. Results from these experiments are presented in the following chapter.

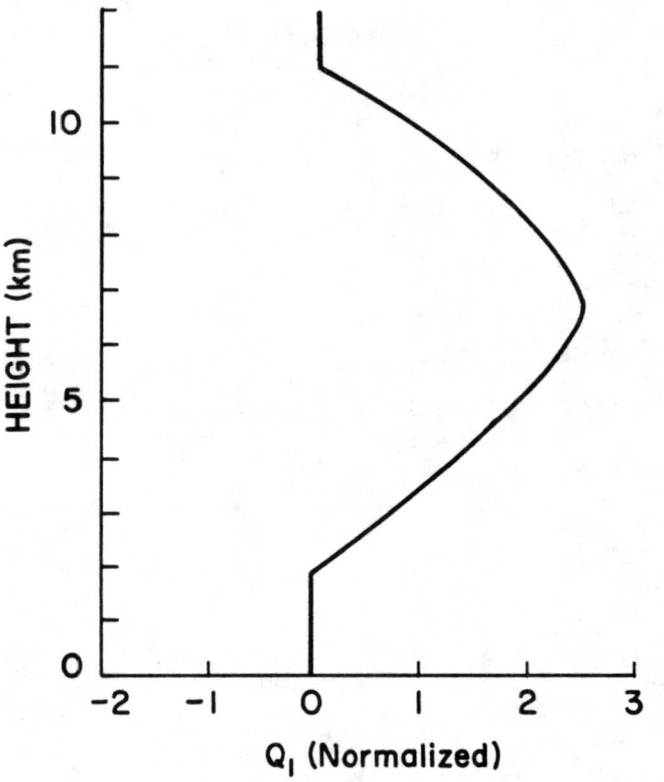

Figure 5.2: Normalized heating profile.

Chapter 6

RESULTS

Several numerical experiments are conducted in this thesis to determine the affects of using inferred heating rates in the RAMS mesoscale model to produce better short-range (0-12 hours) QPFs. The experiments include one 24 hour simulation and four, 12 hour simulations. The 24 hour simulation addresses the problem of how much time is needed before the model dynamics and physics-parameterizations have had sufficient time to develop mesoscale structures, before the onset of precipitation. The only difference between three of the four 12 hour model runs is that, even though a modified cumulus parameterization scheme (refer to chapter 5.3) was used for the same one hour period in all three runs, the precipitation rates used in the modified scheme were estimated by different methods (see chapter 4.3). This was done to determine the model's sensitivity to various rain rates. The fourth 12 hour simulation was run with the original RAMS cumulus parameterization scheme to see how well the simulations that included the forced heating rates improved the QPFs. Results from these numerical experiments as well as the control run are presented in this chapter and chapter 7 discusses the results in detail.

6.1 The Control Run

The Control Run is a straight initialization run. In other words, NMC data from 30 July 1987 at 0000 UTC (29 July at 1800 MDT) are used to initialize the model and plots are obtained from the first time step (0 hour), representing the actual observed data. The most significant problem found in comparing this run to the other simulations is that this run (like all model runs for the initial time step) only produces observed parameters. Therefore, the diagnostic or prognostic parameters, such as the microphysical

mixing ratios, precipitation and w-component fields, are not available. To determine the accuracy of the predicted precipitation fields in the other experiments, comparisons will be made with the radar summary map. The predicted w-component of the wind in the other simulations will be used to explain storm development, but no conclusions will be made on which runs produced the most realistic vertical velocities since the field was not available for the control run.

To examine the quality of data in the control run a comparison will be done with plots from the model's full domain and synoptic plots from 850 and 500 mb. Then plots from the fine grid will be presented since the horizontal resolution is much smaller (28 km) and therefore, it should detect smaller scale features much better. Consequently, all subsequent numerical experiments will also be analyzed on the fine grid and comparisons will be made between them and the fine grid control run results.

6.1.1 Accuracy of control run

Full domain horizontal cross-sections of the wind vector, potential temperature and total mixing ratio fields for 30 July 1987 0000 UTC at 1.38 and 5.94 km, above ground level (AGL), are shown in Figures 6.1 and 6.2, respectively. These heights were chosen because 850 mb is approximately 1500 m above mean sea-level (MSL) and 500 mb is approximately 5900 m above MSL. The most notable feature shown in the wind vector field at 1.38 km (Fig. 6.1a) is the clockwise circulation around the high pressure region centered over Arkansas. This compares well to the 850 mb analysis at 0000 UTC 30 July (Fig. 6.3). The winds at 5.94 km (Fig. 6.2a) reveal that the entire area is dominated by a ridge of high pressure which is centered over the Kansas-Oklahoma border. The same pattern is also shown in the observed data at 500 mb (Fig. 6.4).

Figure 6.1b shows the potential temperature field at 1.38 km. Like the 850 mb analysis map, it shows the warmest potential temperature, 318 K (which corresponds to a temperature of ~30°C at 850 mb), over the Rocky Mountains of Colorado, Wyoming and northern New Mexico and the coolest temperatures are observed along the northwestern coast of the United States with values around 296 K (~9°C at 850 mb). At 5.94 km

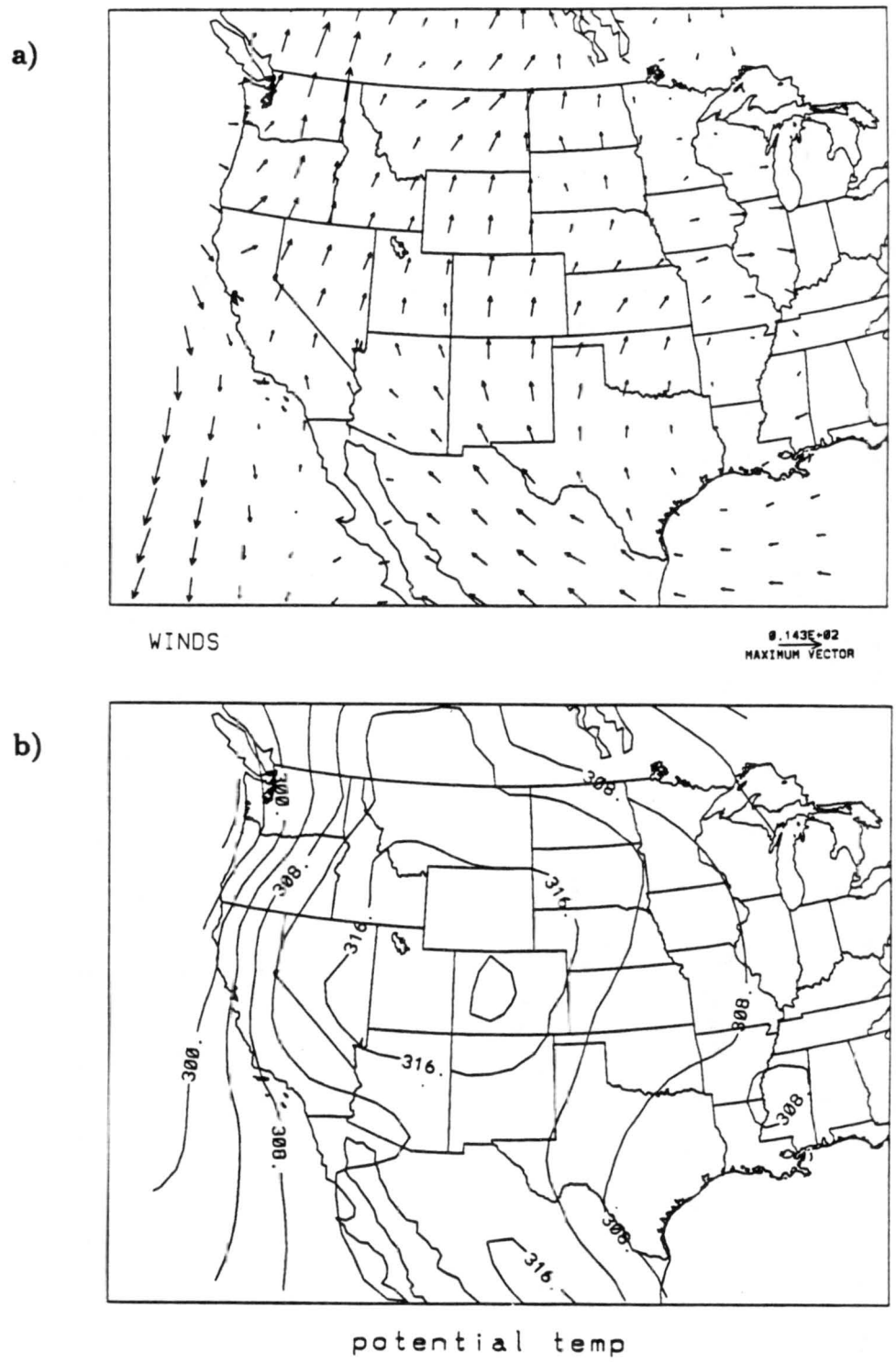

Figure 6.1: Full domain horizontal cross-sections from the Control run at 1.38 km above the surface for the a) wind vectors, b) potential temperature with 4°contour intervals, and c) total mixing ratio with contour intervals (labelled in $\times 10^{-1}$ g/kg) of 2.0 g/kg, all at 0000 UTC 30 July 1987.

c)

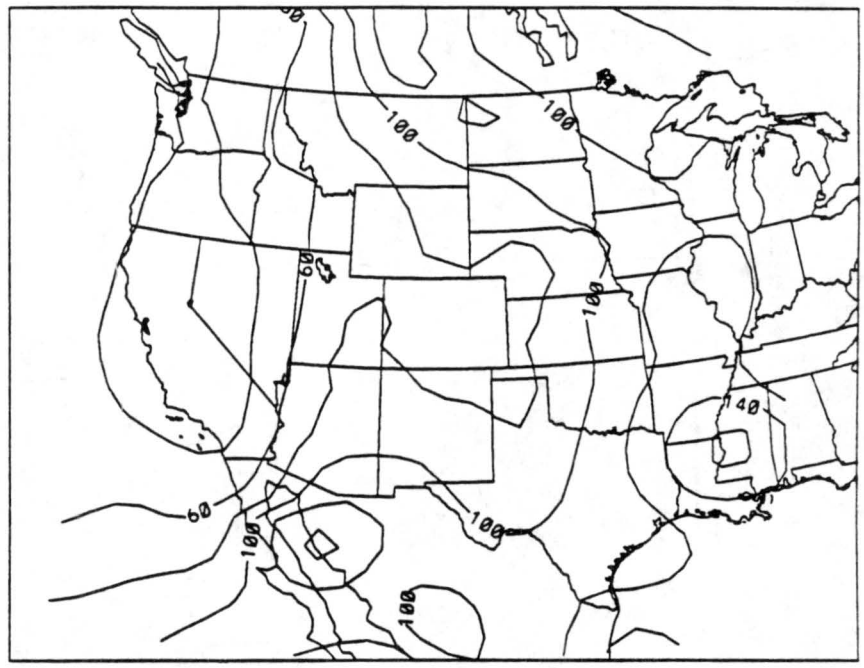

Figure 6.1: Continued.

a)

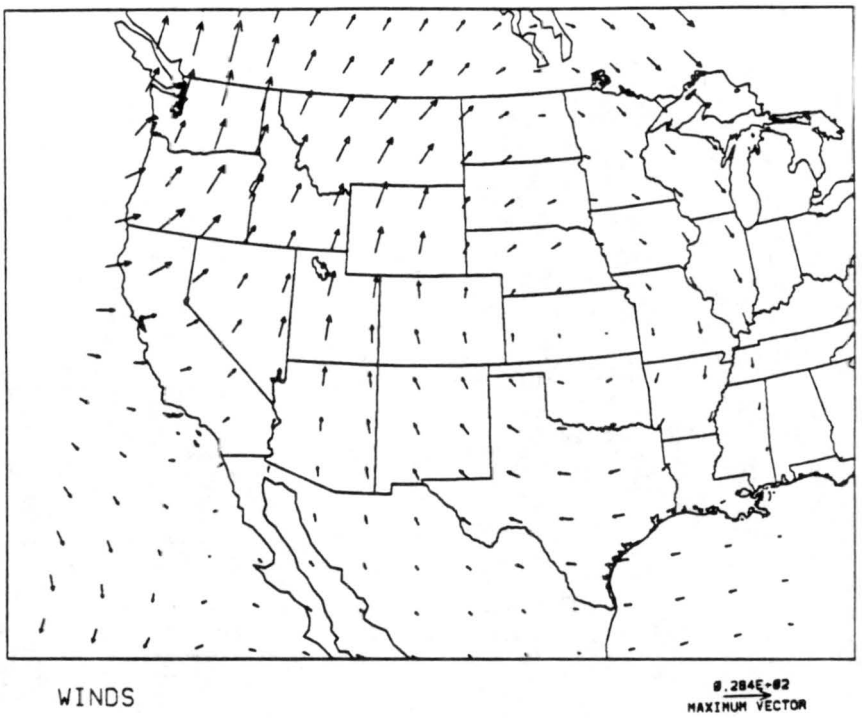

b)

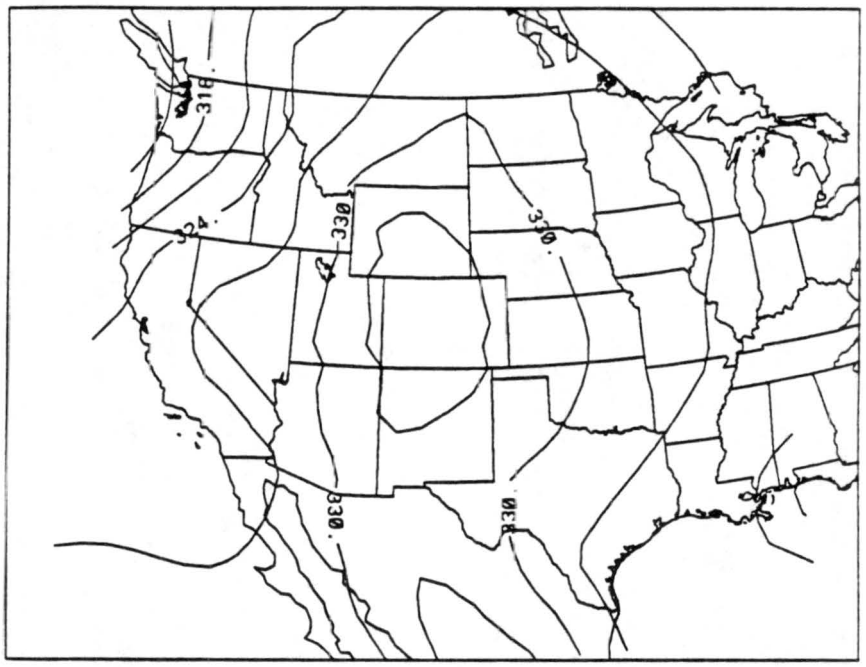

Figure 6.2: Full domain horizontal cross-sections from the Control run at 5.94 km above the surface for the a) wind vectors, b) potential temperature with 3°contour intervals, and c) total mixing ratio with contour intervals (labelled in $\times 10^{-2}$ g/kg) of 0.4 g/kg, all at 0000 UTC 30 July 1987.

c)

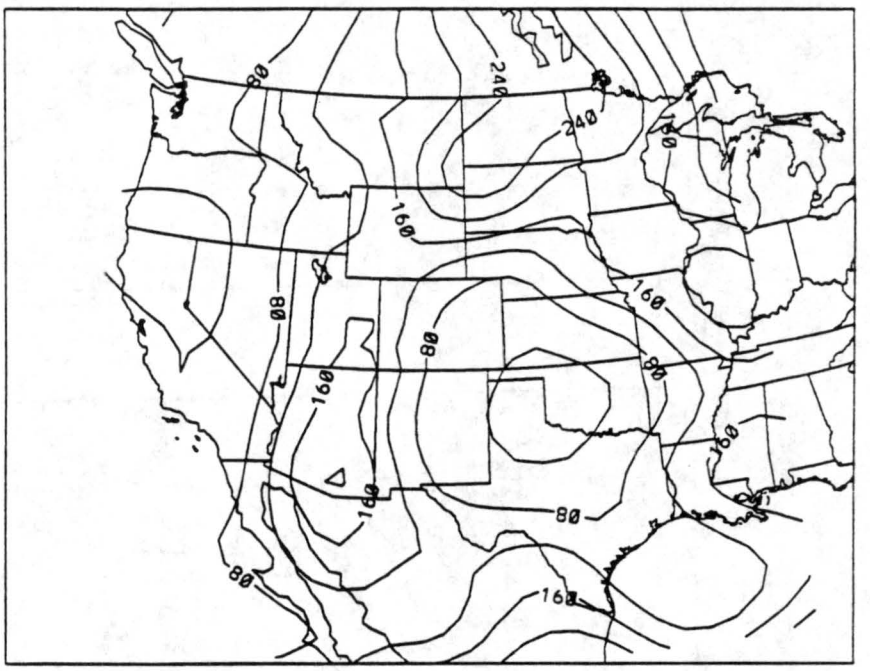

Figure 6.2: Continued.

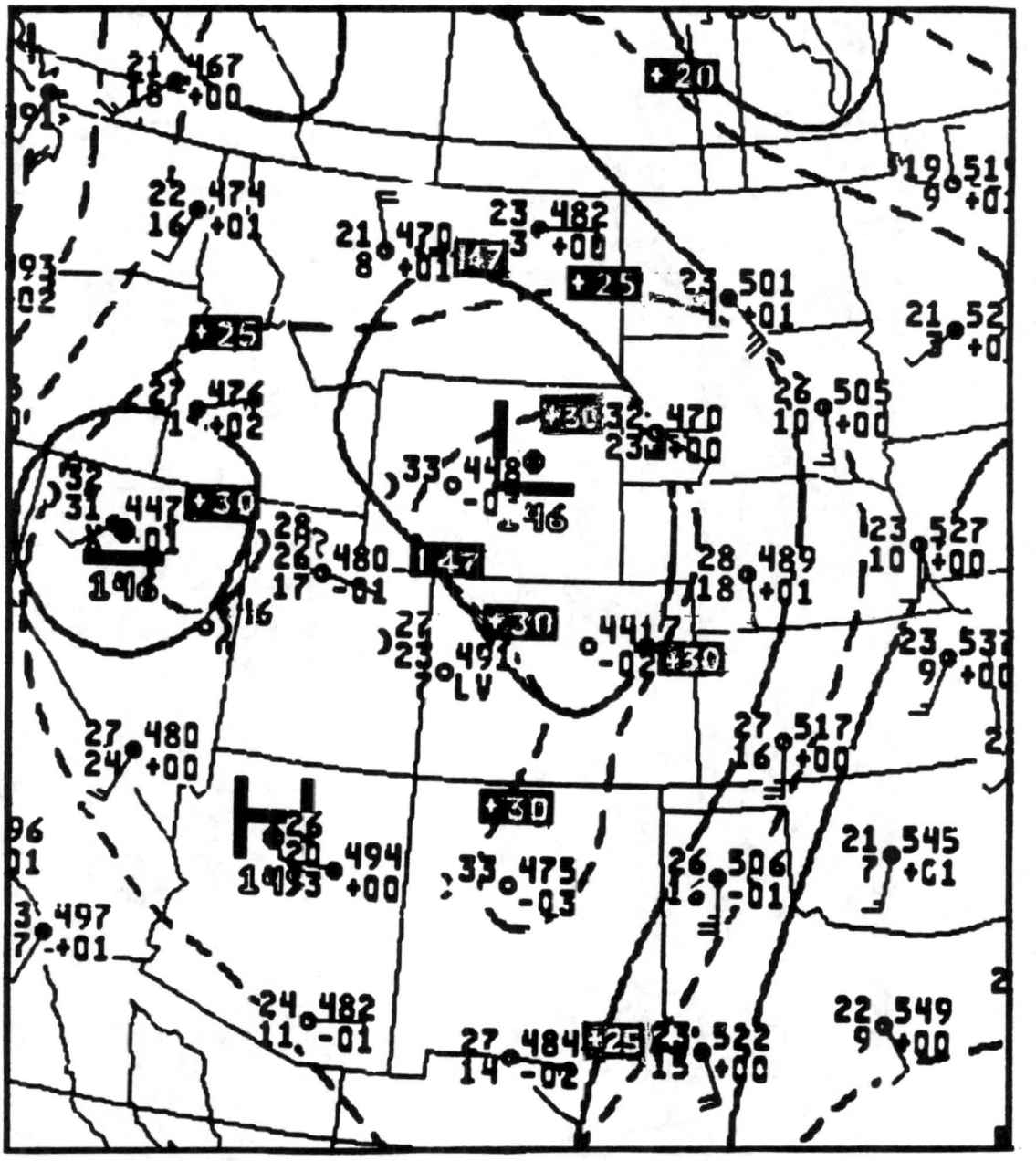

Figure 6.3: 0000 UTC 30 July 1987 850 mb analysis.

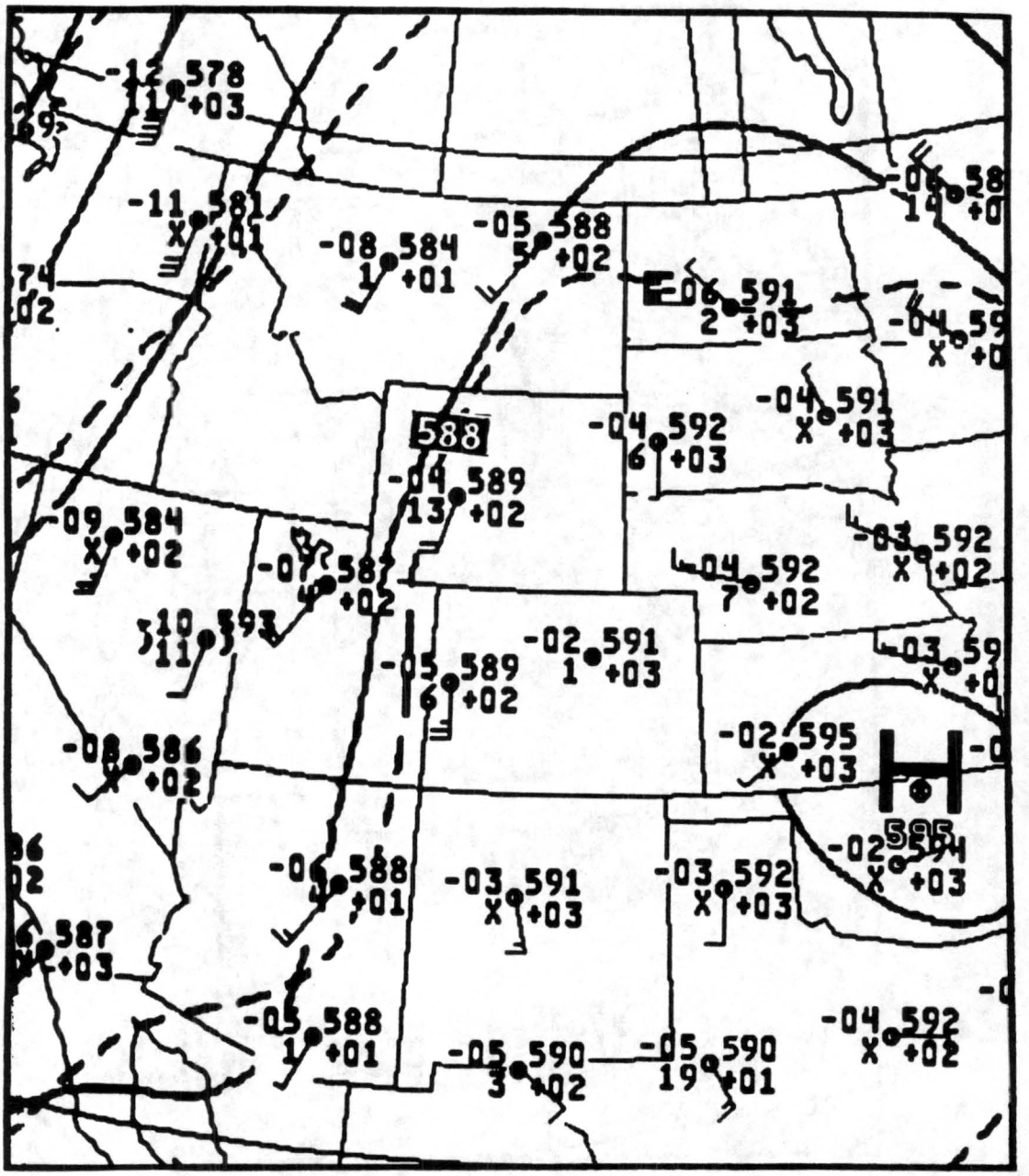

Figure 6.4: 0000 UTC 30 July 1987 500 mb analysis.

(Figure 6.2b) the potential temperature field reveals that most of the central United States has temperatures warmer than 330 K (~ -3°C at 500 mb) which corresponds well with the 500 mb analysis which shows temperatures in this same area warmer than -05°C. The coolest potential temperatures were located in the northwest with values of 315 K (~ -15°C at 500 mb).

The total mixing ratio field at 1.38 km (Fig. 6.1c) indicates that the area with the most abundant moisture supply is located in the southeast and the driest area is associated with the western most States. Once again, this compares well with the 850 mb map, with the exception of a few isolated areas in the northeast where dewpoints of less than 4 degrees were reported.

6.1.2 Control run – fine grid results

The u-component of the wind for the fine grid (Figure 6.5a) is very weak near the surface (0.10 km AGL) and predominantly from the west. However, there is a small area of weak, easterly winds over the southwestern portion of the fine grid model domain, which includes northern Arizona, northwest New Mexico and southern Utah. The wind speeds varied from -1.8 m/s (along the northern New Mexico-Arizona border) to 2.7 m/s (in Central Wyoming). The v-component at 0.10 km (Figure 6.5b) reveals that the winds are mostly from the south, with a few, isolated exceptions of northerly flow over Colorado.

The easterly and northerly wind components shown in Figures 6.5a and b are not observed in the synoptic scale maps but these conditions could be produced by smaller, mesoscale features; thus, it's difficult to determine the accuracy of the data without mesoscale data in these areas. Fortunately, a small portion of the area in question was within the PAM network, in the Denver area, and the northerly winds in northern Colorado were detected by these data. However, the fine grid surface horizontal wind pattern from the control run shows northwest wind colliding with southwest winds a few miles north of Denver, at 0000 UTC. Recall from chapter 4 that the PAM data showed northwest wind colliding with southeast wind in Denver at 0000 UTC. Thus, the control run

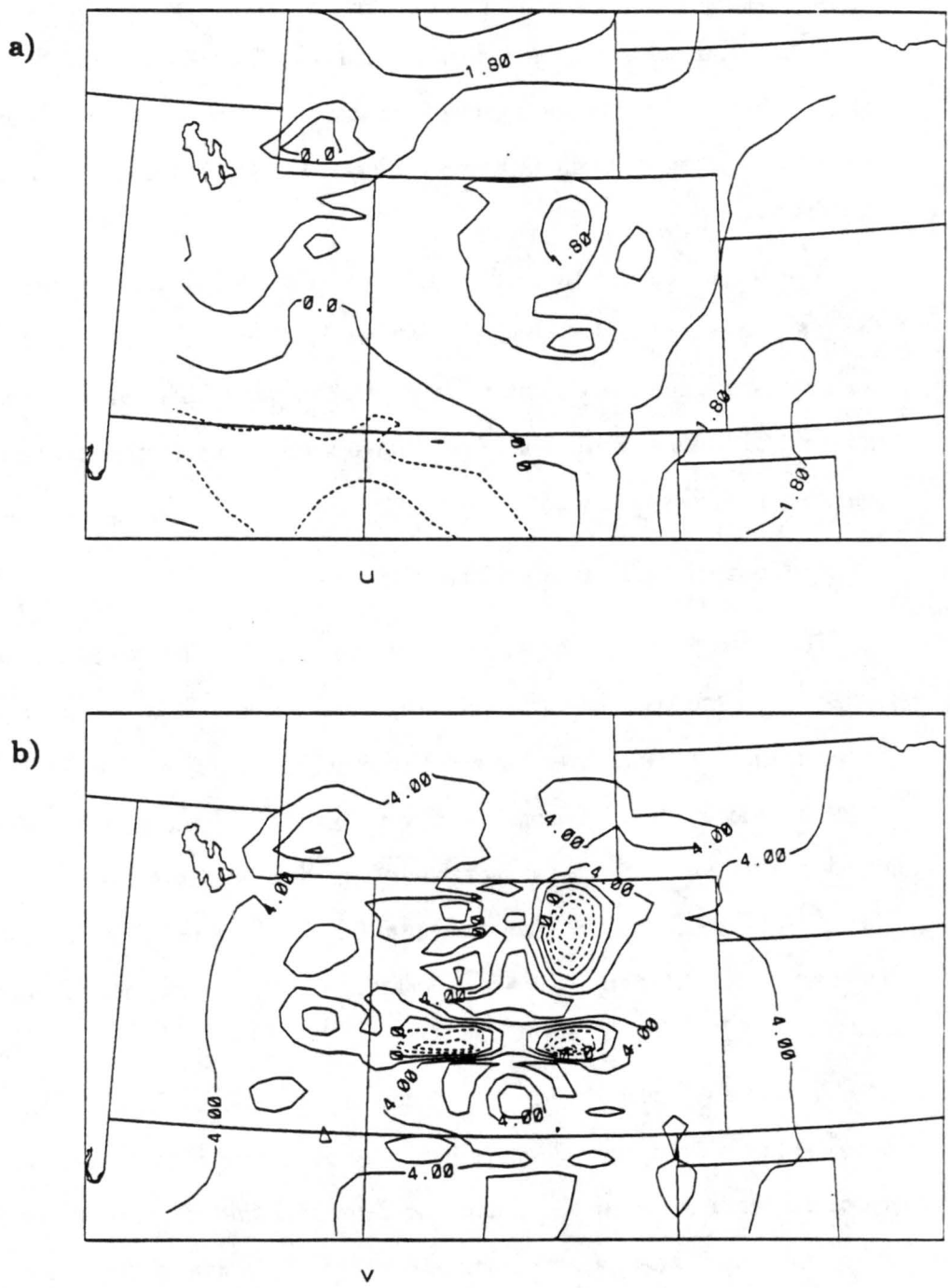

Figure 6.5: Fine grid horizontal cross-sections from the Control run at 0.10 km above the surface for the a) u-component with 0.9 m/s intervals, b) v-component with 2.0 m/s intervals, c) potential temperature with 4°contour intervals, and d) total mixing ratio with contour intervals (labelled in $\times 10^{-}1$ g/kg) of 2.0 g/kg, all at 0000 UTC 30 July 1987.

c)

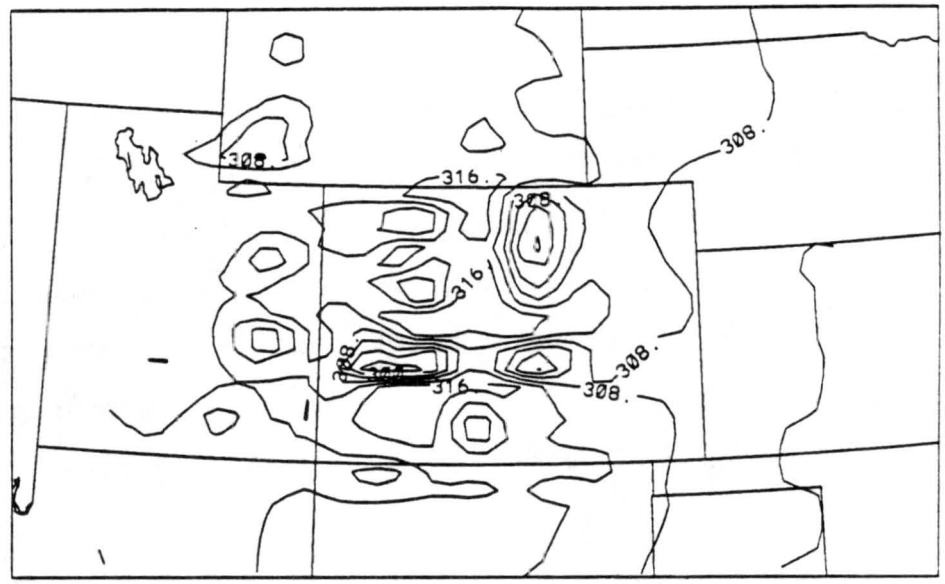

potential temp

d)

total mix ratio

Figure 6.5: Continued.

has the convergence line positioned fairly close to its actual location but it has southwesterly winds south of Denver instead of southeasterly winds. This indicates that the outflow associated with the storm southeast of Denver (refer to Chapter 4) was not represented by the NMC data.

The upper-level flow is depicted in figures 6.6a and b, at a height of 5.94 km above the surface terrain. Even though this is not a constant height surface, the presence of an upper-level ridge, centered somewhere east of south-central Kansas is evident due to southeasterly winds located over the southeastern part of the fine grid and southwesterly flow observed elsewhere. The location of this anticyclonic flow is in reasonable agreement with the 500 mb height analysis (Figure 6.4).

The potential temperature field at 0.10 km AGL, shown in Figure 6.5c, shows the warmest temperatures, 316 K, over the Colorado Rockies. The most notable features at this level is the isolated cool spots in Colorado that are located in the same areas as the northerly winds were. This suggests that these areas may be the result of evaporatively cooled downdraft air that diverged near the surface, producing gust fronts. One of the cold pools of air is located a few miles north of Denver producing a strong temperature gradient in the area that ranges from 300 K north of Denver to 316 K just south of Denver. A strong temperature gradient was also observed in the PAM data at this time (refer to figure 4.5c), however, PAM showed the coolest air located in Denver and warmer temperatures observed east of the area. Also, the PAM potential temperatures ranged from 311 K to 322 K. Therefore, according to the observed surface data, the model's temperatures were too cool and centered slightly north of its actual location.

Figure 6.5d contains the total mixing ratio field at 0.10 km. The values over Colorado range from 4 g/kg in the southwest to nearly 12 g/kg along the eastern border. The Denver area has values between 8 and 10 g/kg, indicating that the strong gradient (ranging from 9.5 to 14.5 g/kg) observed in the mesoscale data (figure 4.6c) was not adequately resolved in the NMC data.

a)

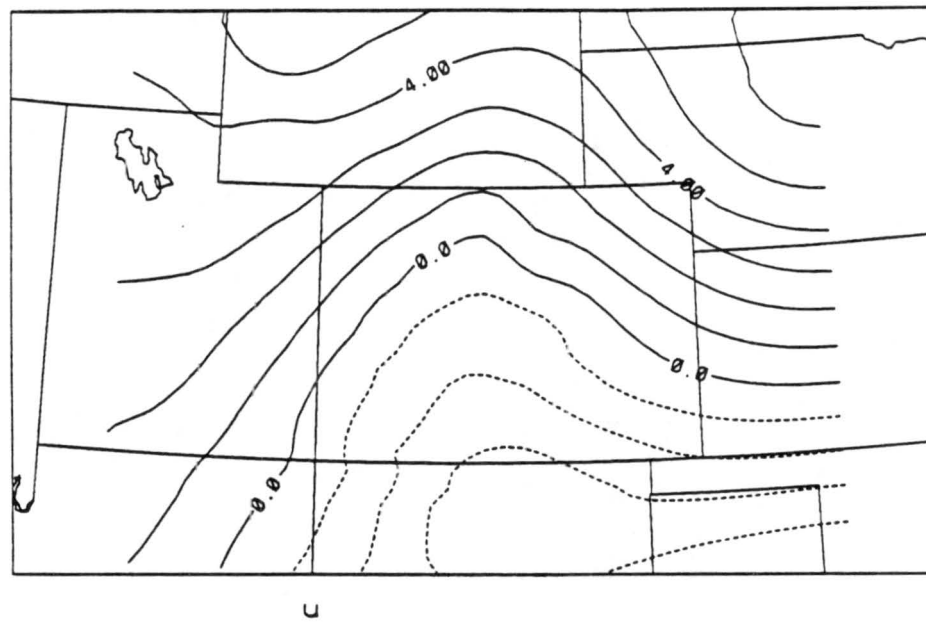

b)

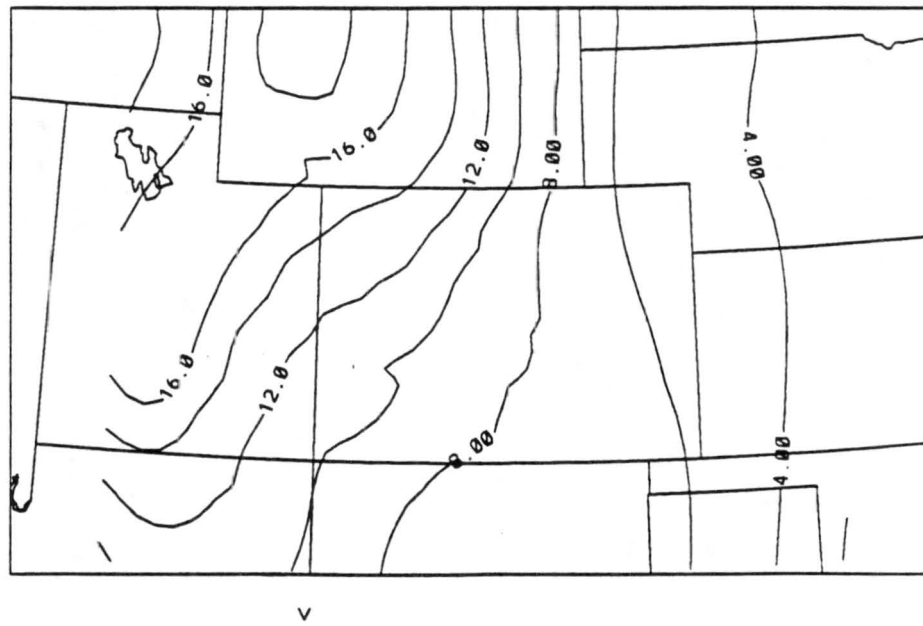

Figure 6.6: Fine grid horizontal cross-sections from the Control run at 5.94 km above the surface for the a) u-component with 1.0 m/s intervals, b) v-component with 2.0 m/s intervals, c) potential temperature with 1°contour intervals, and d) total mixing ratio with contour intervals (labelled in $\times 10^{-2}$ g/kg) of 0.3 g/kg, all at 0000 UTC 30 July 1987.

c)

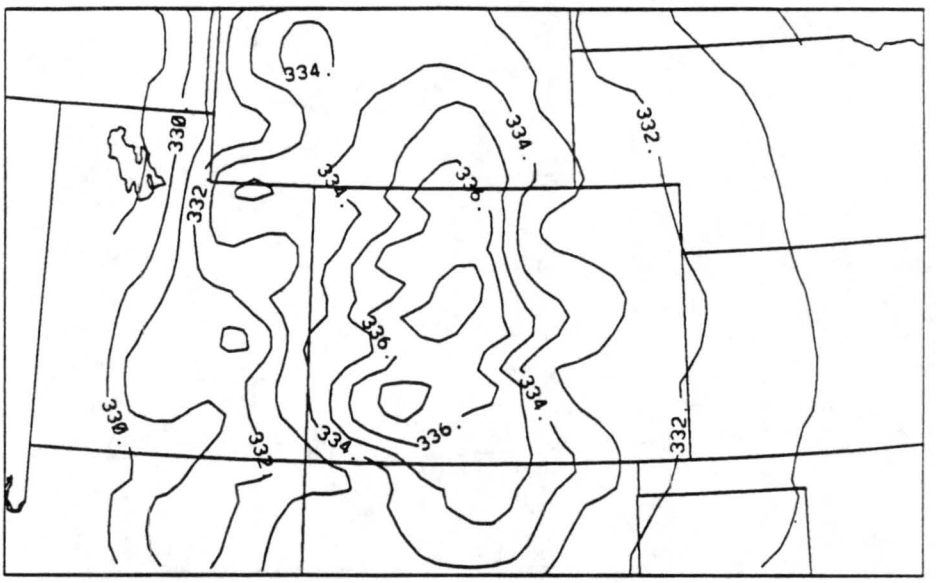

potential temp

d)

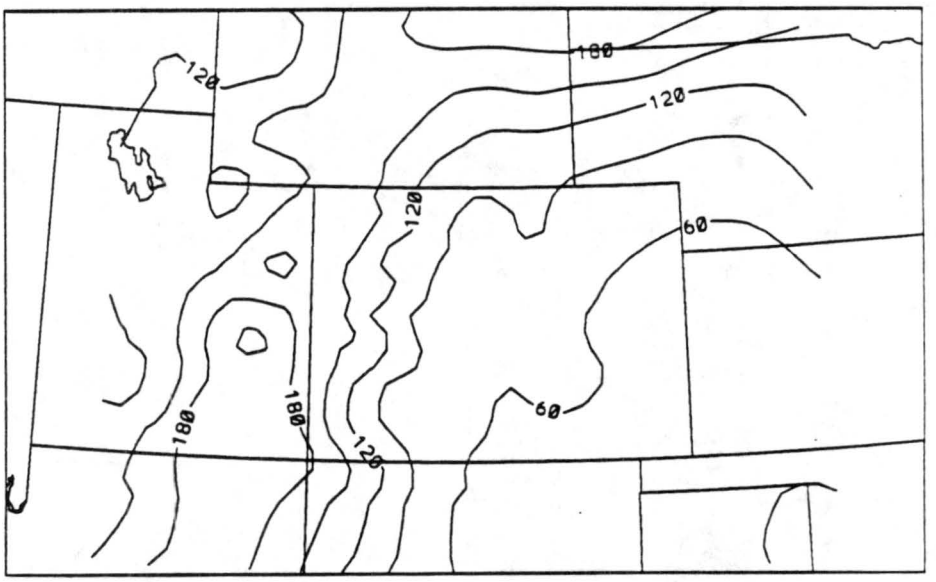

total mix ratio

Figure 6.6: Continued.

6.2 Experiment 1 - 24 Hour Simulation With No Forced Heating

The model is initialized at 0000 UTC on 29 July 1987 for experiment 1, with full microphysical and the RAMS Kuo-type cumulus parameterization scheme activated for the entire simulation. The near surface (0.1 km AGL) predicted winds, temperature and moisture fields at 0000 UTC 30 July (24 hours after the simulation began) are shown in Figure 6.7.

The u-component of the wind reveals an elongated area of light easterly winds oriented parallel to and east of the Rocky Mountains in Colorado near the surface (Fig. 6.7a). The remainder of Colorado is under the influence of westerly winds. The v-component shows southerly winds over the entire area, near the surface with the exception of a small area in southeast Wyoming and northern Colorado. Thus, the horizontal wind pattern reveals a north/south convergence line separating northwesterly winds from southeasterly winds along the Front Range of Colorado and in southeast Wyoming. This compares well with wind data from the surface mesonet stations (shown in figure 4.7d) and produces a more accurate horizontal wind pattern than the NMC data did at this time (refer to the control run u and v fields).

The horizontal wind pattern at 5.94 km (Figure 6.8a and b) reveals the same general pattern as the control run. The only significant difference is that the westerly wind speeds are almost double in this run and the southerly winds are about 4 m/s slower, in the west, than the control run.

The vertical wind field near the surface (Fig. 6.7c) shows a large area of descending air over Wyoming and central Colorado with peak values of -0.12 m/s over north-central Colorado. The strongest ascent was located southeast of Denver, with a value of 0.08 m/s. At 5.94 km above the surface (Figure 6.8c) the strongest ascent was observed in eastern Wyoming and northeast Arizona (both with values close to 0.2 m/s) and northeast Utah (with 0.10 m/s).

The region with the warmest potential temperatures at 0.10 km AGL is located east of the Rockies in Colorado (Denver is included in this warm region) extending northward along the Wyoming-Nebraska border. Temperatures as high as 322 K, which is equivalent

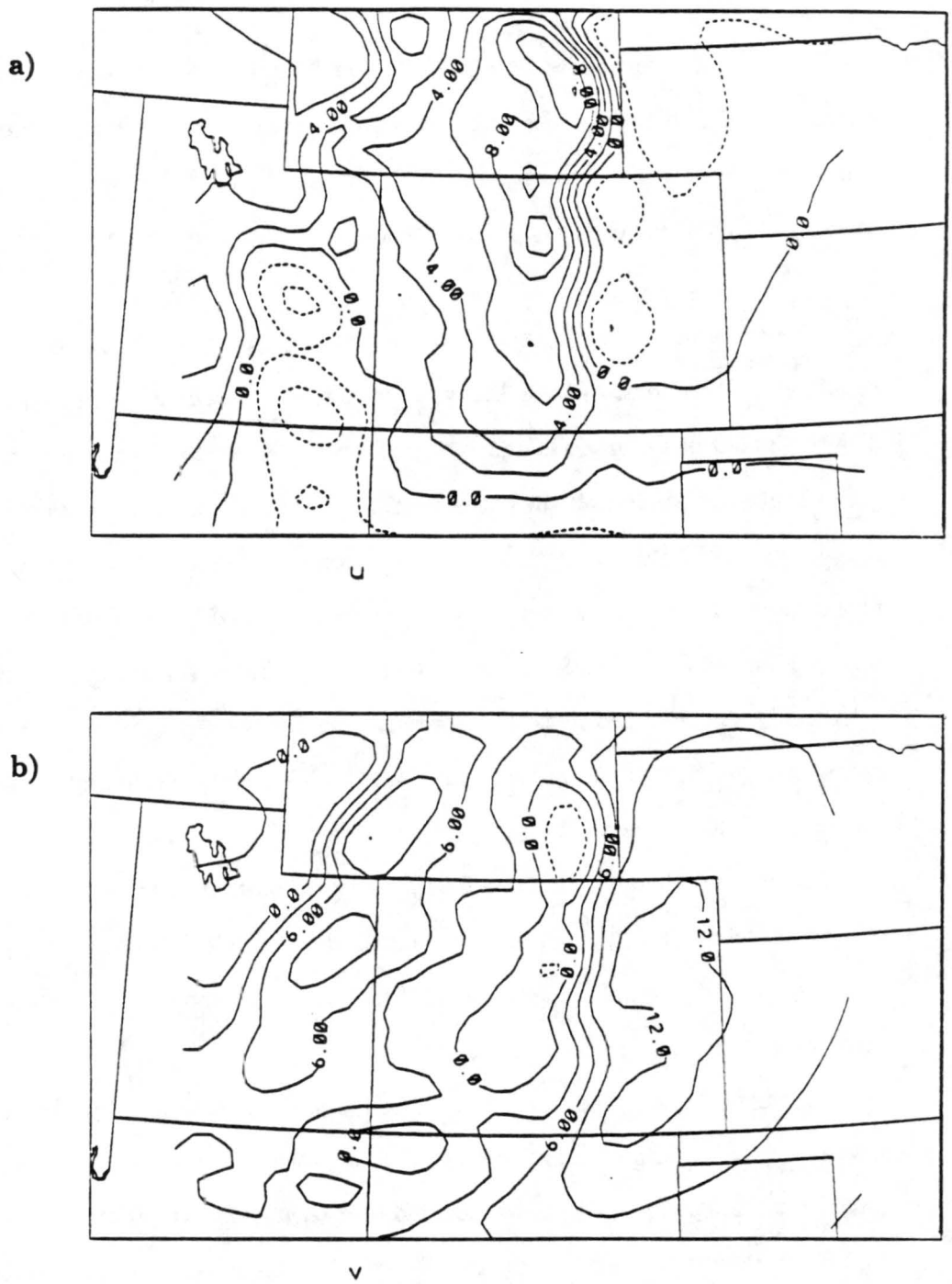

Figure 6.7: Fine grid horizontal cross-sections from Experiment 1 at 0.10 km above the surface for the a) u-component with 2.0 m/s intervals, b) v-component with 3.0 m/s intervals, c) w-component with 0.04 m/s contour intervals, d) potential temperature with 2°contour intervals, e) total mixing ratio with contour intervals (labelled in $\times 10^{-1}$ g/kg) of 1.0 g/kg, f) accumulative surface rain with 6 mm intervals, and g) rain mixing ratio with 0.01 intervals, all at 0000 UTC 30 July 1987.

c)

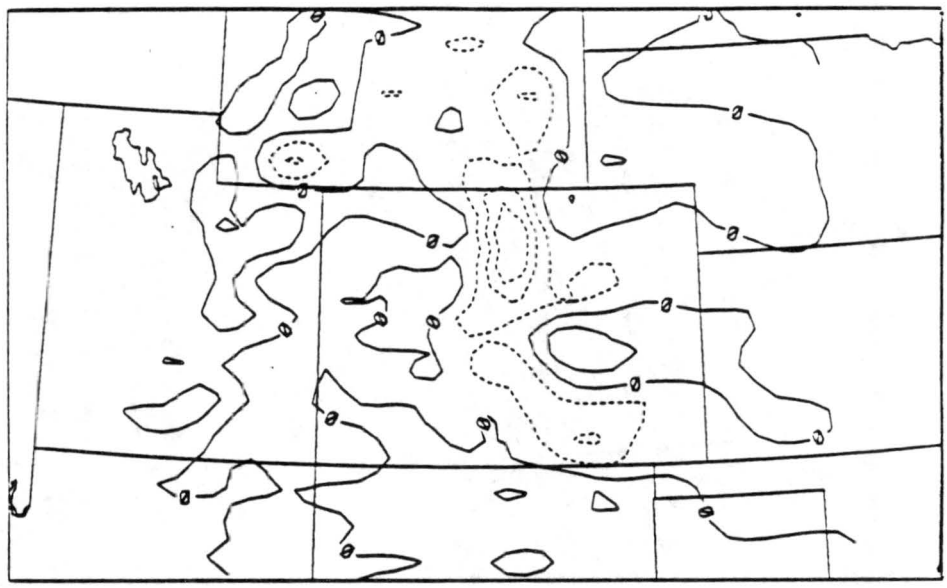

d)

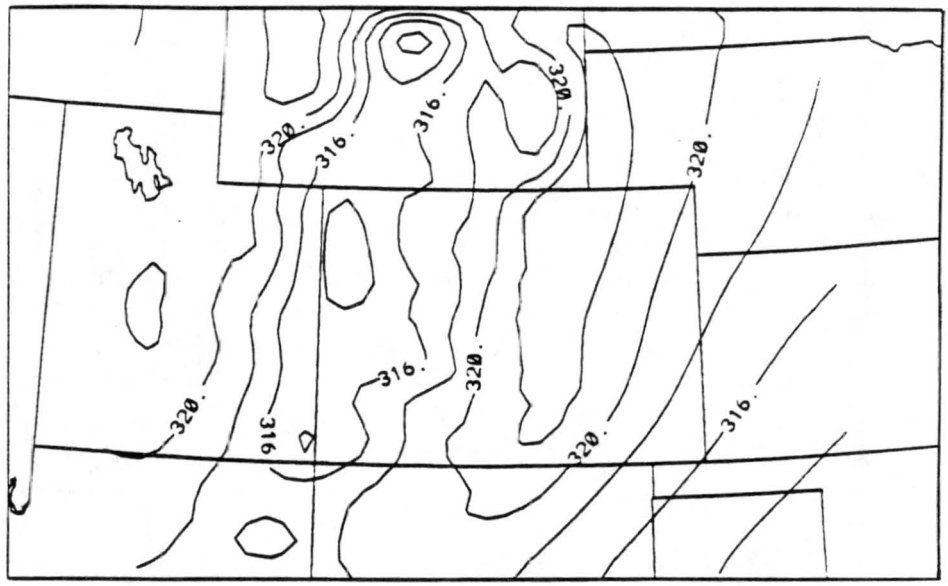

Figure 6.7: Continued.

e)

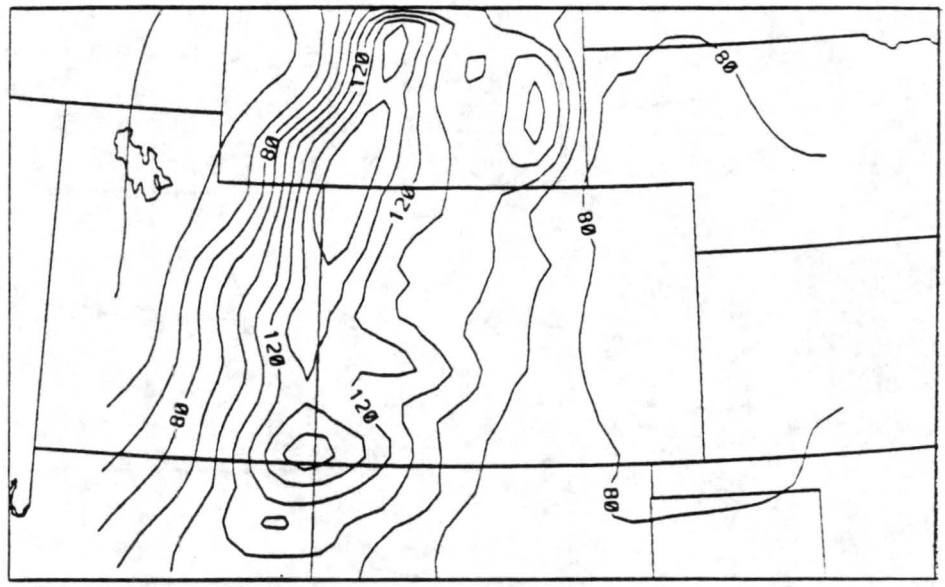

total mix ratio

f)

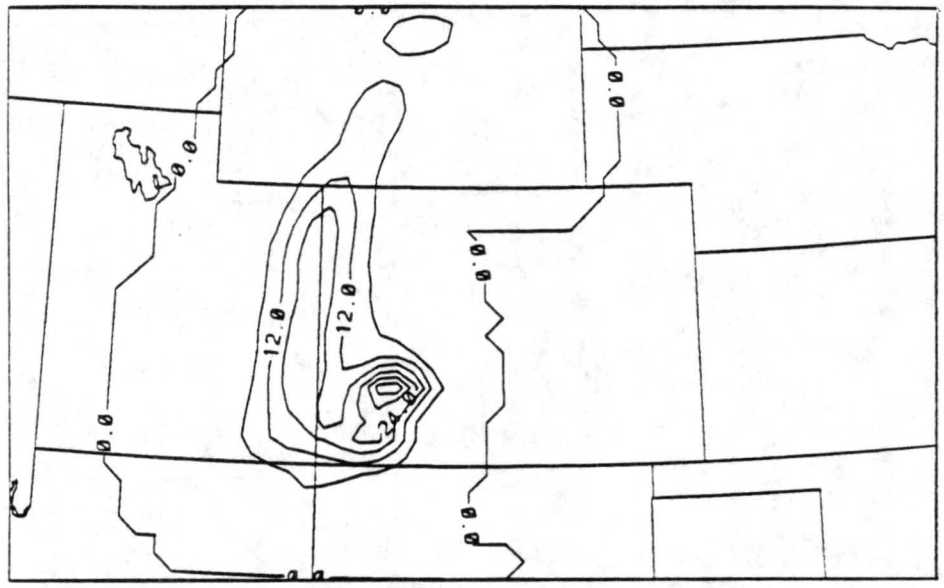

PRECIP. RAIN

Figure 6.7: Continued.

g)

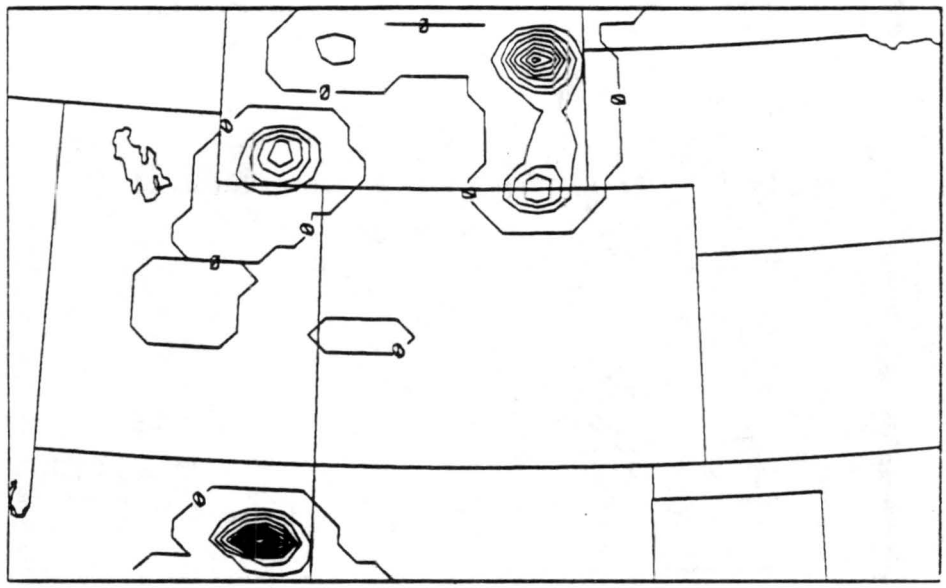

Figure 6.7: Continued.

a)

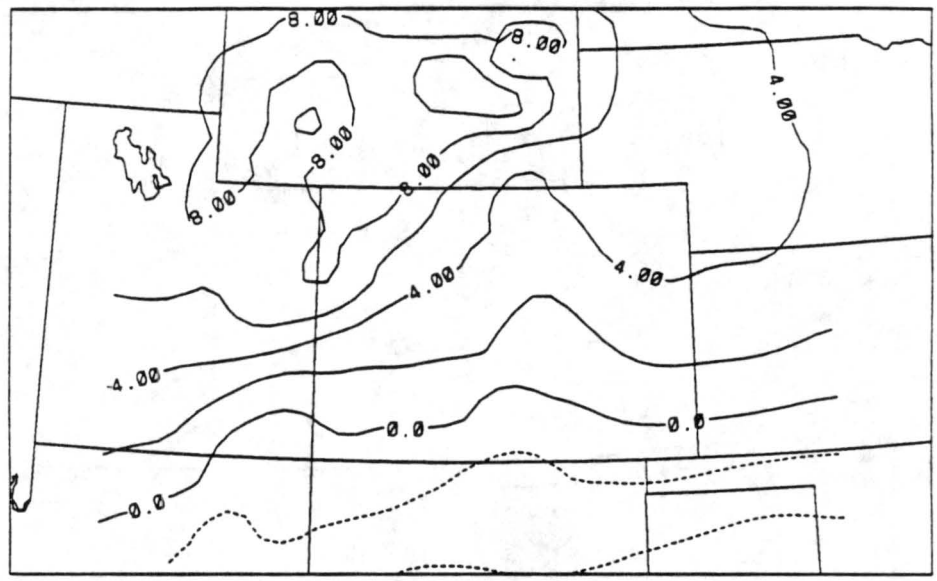

b)

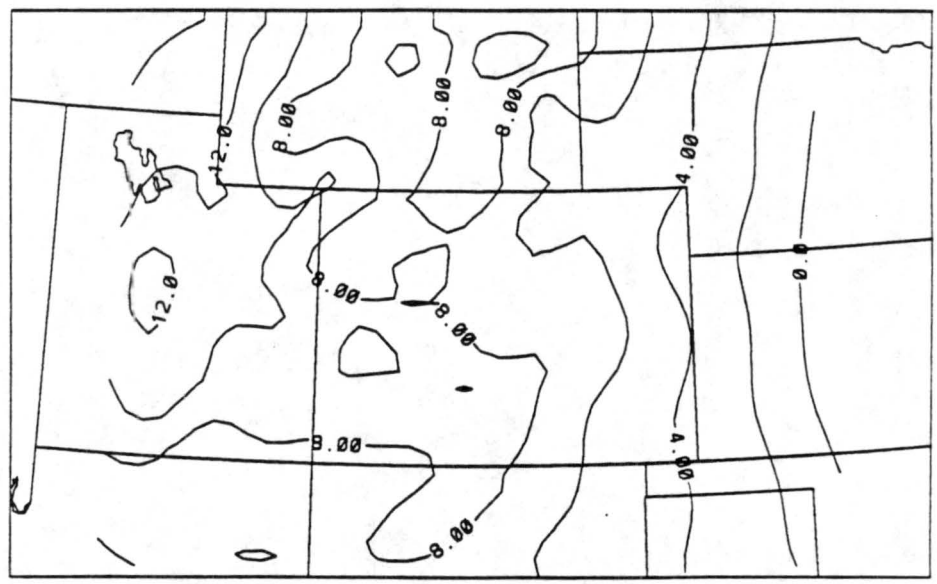

Figure 6.8: Fine grid horizontal cross-sections from Experiment 1 at 5.94 km above the surface for the a) u-component with 2.0 m/s intervals, b) v-component with 2.0 m/s intervals, c) w-component with 0.05 m/s contour intervals, d) potential temperature with 1°contour intervals, and e) total mixing ratio with contour intervals (labelled in $\times 10^{-2}$ g/kg) of 0.6 g/kg, all at 0000 UTC 30 July 1987.

c)

d)

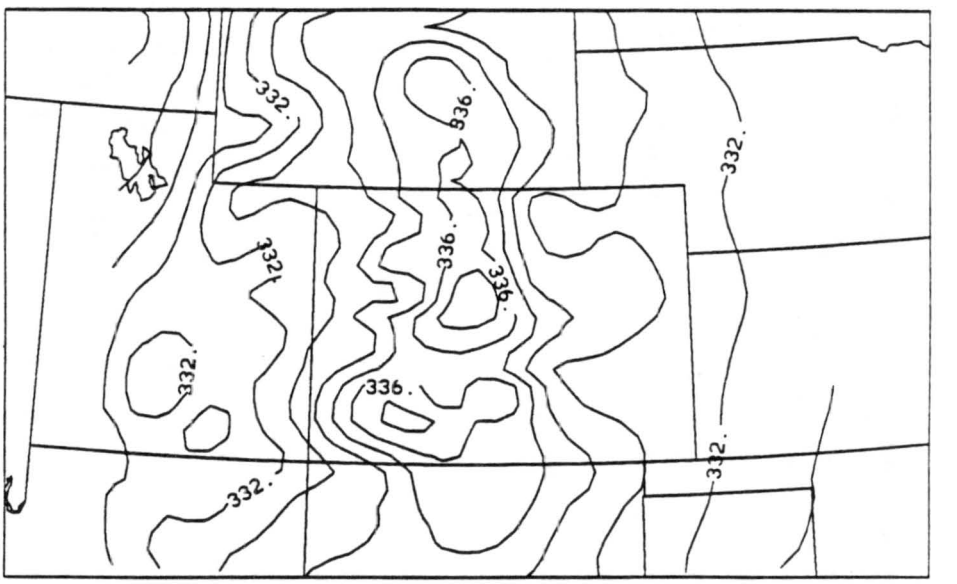

Figure 6.8: Continued.

e)

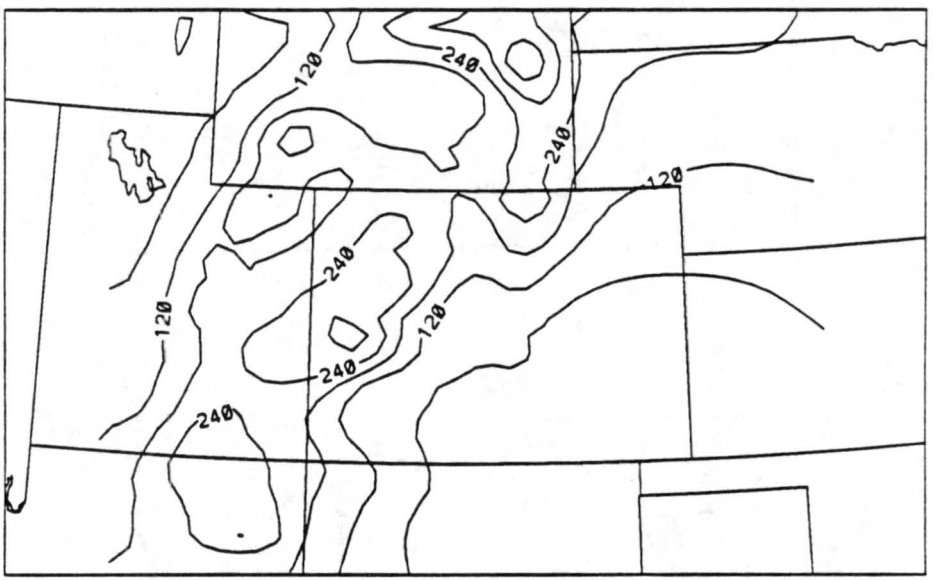

Figure 6.8: Continued.

to a surface temperature of 33°C at 1.7 m above mean sea level (the approximate height 100 m above Denver). This value is close to the 850 mb temperature but the surface mesonet data showed a strong surface potential temperature gradient at 0000 UTC, in the Denver area, that varied from 311 K to 322 K. Not surprisingly, considering its coarse resolution, the model does an inadequate job of predicting the isolated cold pools, associated with mesoscale gust fronts. Also, the coolest potential temperatures predicted by the model at this time are in central Wyoming and northwest Colorado which doesn't compare favorably with the 850 mb height analysis or the control run.

The near surface total mixing ratio field (Fig 6.7e) is quite different than the control run. The maximum values, of 14 g/kg, are located along the western border with minimum values of 7 and 8 g/kg found in eastern Colorado. Despite the inconsistencies in the extreme values, the Denver area has values close to 9 g/kg, which is in reasonable agreement with the control run and was also observed by the mesonet data. However, this simulation did not predict the strong mixing ratio gradient that was observed over the CINDE network by the PAM data.

The accumulative surface precipitation (in mm) is shown in Figure 6.7f. The abundance of rain fell over southwest Colorado, where a maximum of 36 mm fell during the 24 hour period. This total is misleading when it comes to identifying areas of precipitation that correspond with storms occurring on 29 July local time because a large portion of the total precipitation resulted from storms occurring on the evening of 28 July. The most significant factor revealed in this field is the lack of rain produced in eastern Colorado during this time period. The 0.01 km AGL simulated rain mixing ratio field at 0000 UTC July 30 (Figure 6.7g) shows rain occurring over most of Wyoming with a peak value of 0.08 g/kg in east-central Wyoming. This indicates that the model predicted the storm to far north of its actual location. Note that the simulated rainfall in both the accumulative and rain mixing ratio fields comes from the explicit microphysics and not the cumulus parameterization scheme!

6.3 Experiment 2 - 12 Hour Simulation With No Forced Heating

This simulation is initialized at 1200 UTC on 29 July 1987 and as in Experiment 1, full microphysics and cumulus parameterization schemes are turned on for the entire simulation. However, unlike the previous 24 hour simulation, Experiment 2 is a 12 hour simulation (both ending at 0000 UTC 30 July).

At 0000 UTC on 30 July the u-component of the wind at 0.1 km above the terrain, Figure 6.9a, indicates westerly winds, as strong as 9 m/s in some areas, over much of Colorado and the surrounding States. Easterly winds were only observed in the extreme southwestern part of Colorado, southeast Utah, northern Arizona and northwestern New Mexico. Figure 6.9b shows the v field and the only northerly flow shown is over central Colorado, extending north along the Nebraska-Wyoming border. Thus, the horizontal wind pattern reveals a north/south convergence line east of the Rockies with northwest flow west of the line and southwest flow east of the line. The pattern is similar to the control run but the northerly wind is more continuous in Colorado and extends up into southeast Wyoming. This suggests that the model was not able to predict the isolated areas of convergence (that might have been associated with localized thunderstorms) shown in the control run. As was the case in the control run, this simulation inadequately produced the observed easterly flow at the surface in central Colorado.

The upper-level horizontal wind pattern, depicted in figures 6.10a and b at 5.94 km AGL, reveals that this area is under the influence of a ridge of high pressure (centered east of southern Colorado) since there's southeasterly flow in the southern part of the grid and southwesterly flow over the remaining area, producing anticyclonic rotation. This pattern closely resembles the u and v winds in the control run and verifies well with the upper-level observations taken from the 500 mb analysis map (Figure 6.4).

The w field at 0.10 km AGL (Figure 6.9c) is dominated by stronger descending motion over Colorado, reaching a maximum of -0.12 m/s over north central Colorado. One of the few regions of weak ascent (speeds are typically less than 0.03 m/s) is located in the Denver area. At 5.94 km AGL the vertical motion field was still characterized by downdrafts over most of Colorado.

a)

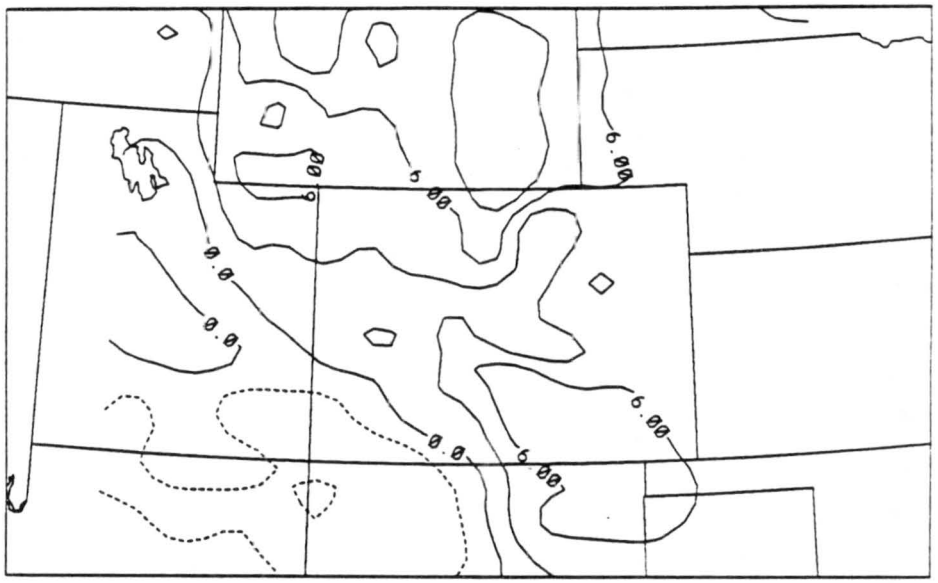

U

b)

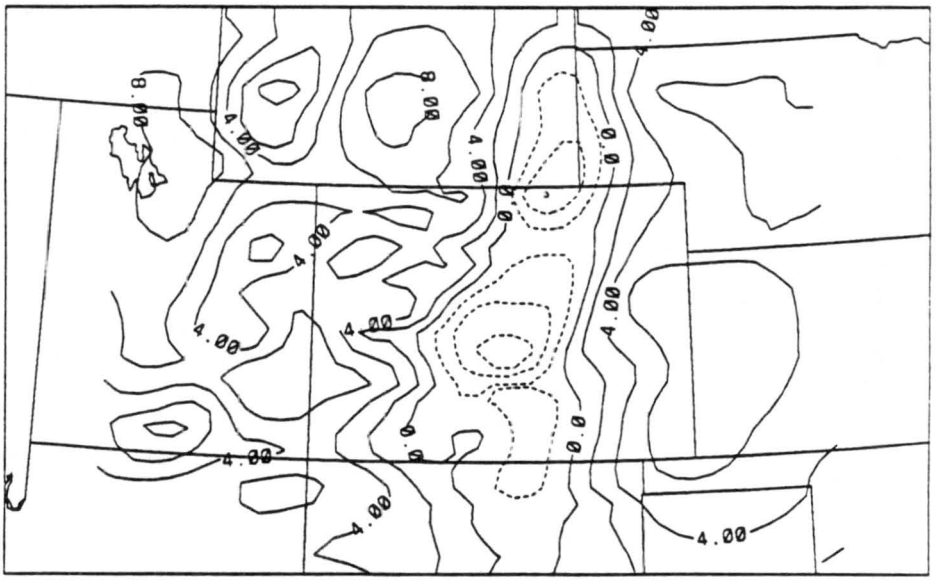

V

Figure 6.9: Fine grid horizontal cross-sections from Experiment 2 at 0.10 km above the surface for the a) u-component with 3.0 m/s intervals, b) v-component with 2.0 m/s intervals, c) w-component with contour intervals (labelled in $\times 10^{-3}$ m/s) of 0.03 m/s, d) potential temperature with 2°contour intervals, e) total mixing ratio with contour intervals (labelled in $\times 10^{-1}$ g/kg) of 1.0 g/kg, f) accumulative surface rain with 0.008 mm intervals, and g) rain mixing ratio with 3 $\times 10^{-4}$ g/kg contour intervals, all at 0000 UTC 30 July 1987.

c)

d)

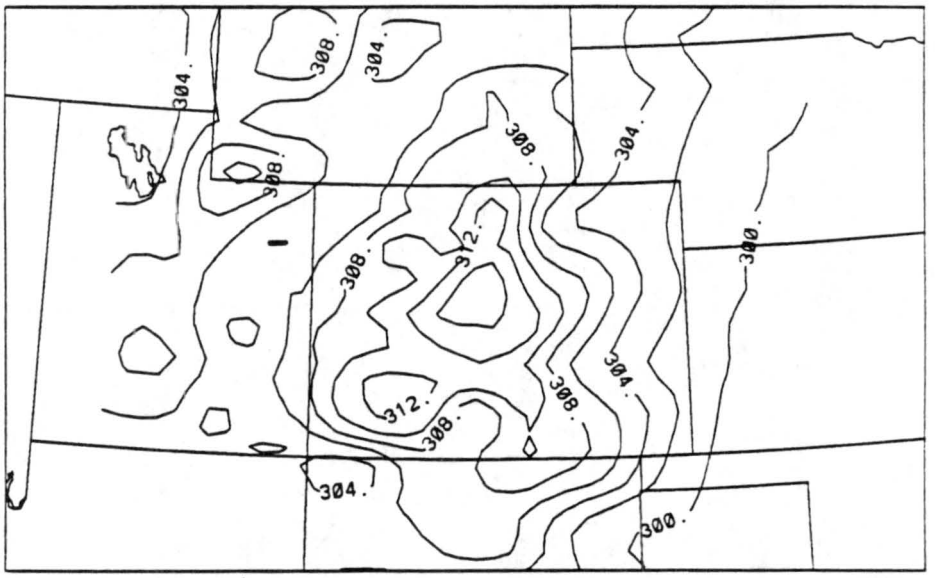

Figure 6.9: Continued.

e)

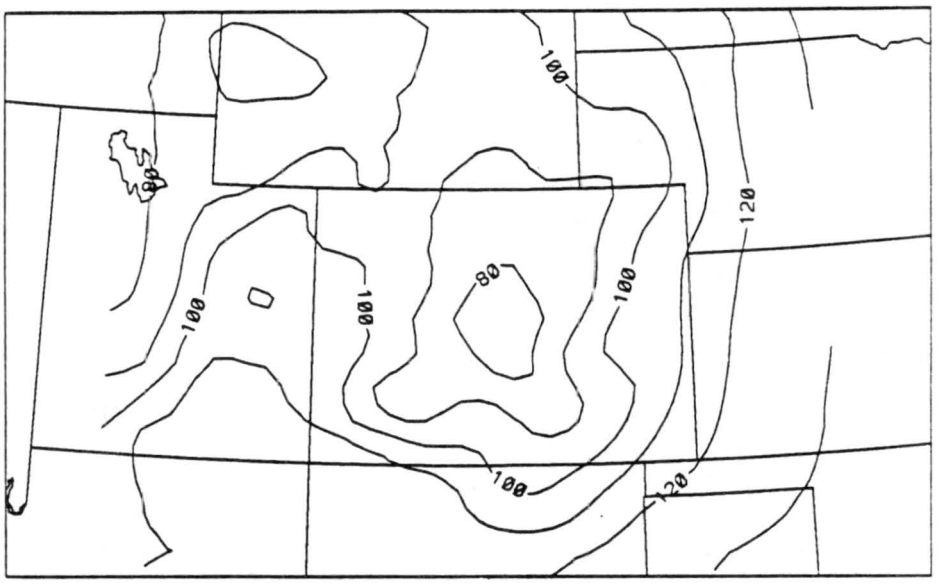

f)

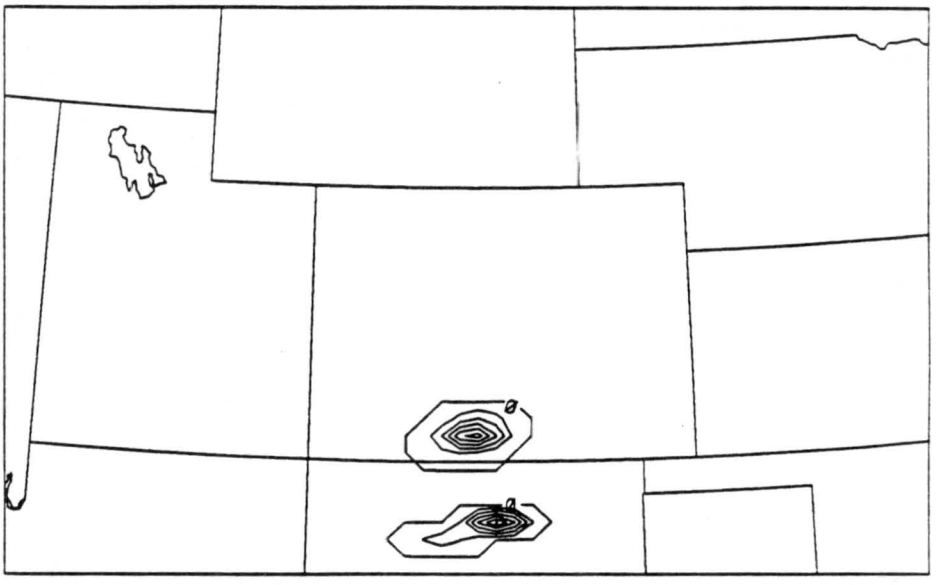

Figure 6.9: Continued.

g)

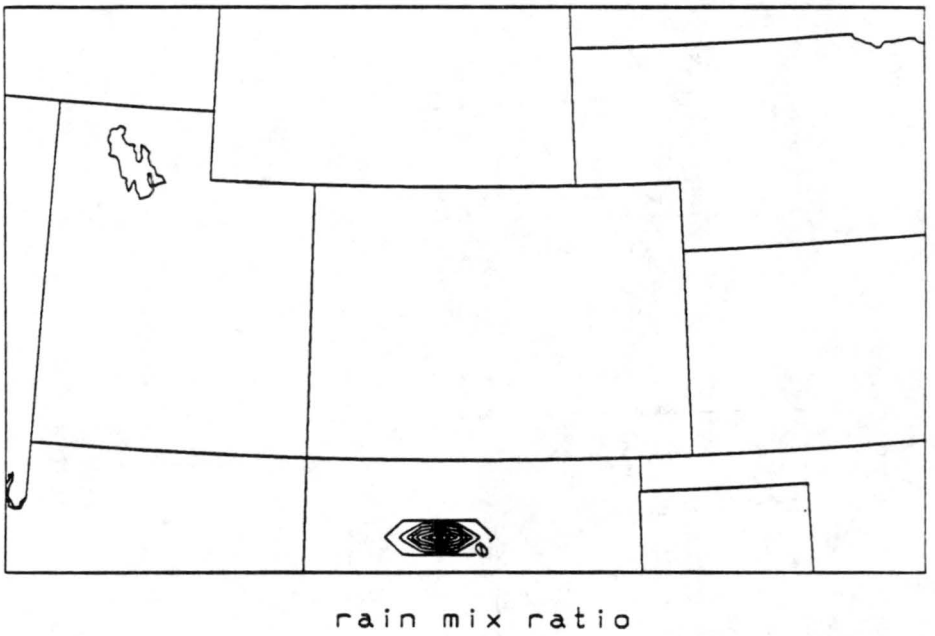

Figure 6.9: Continued.

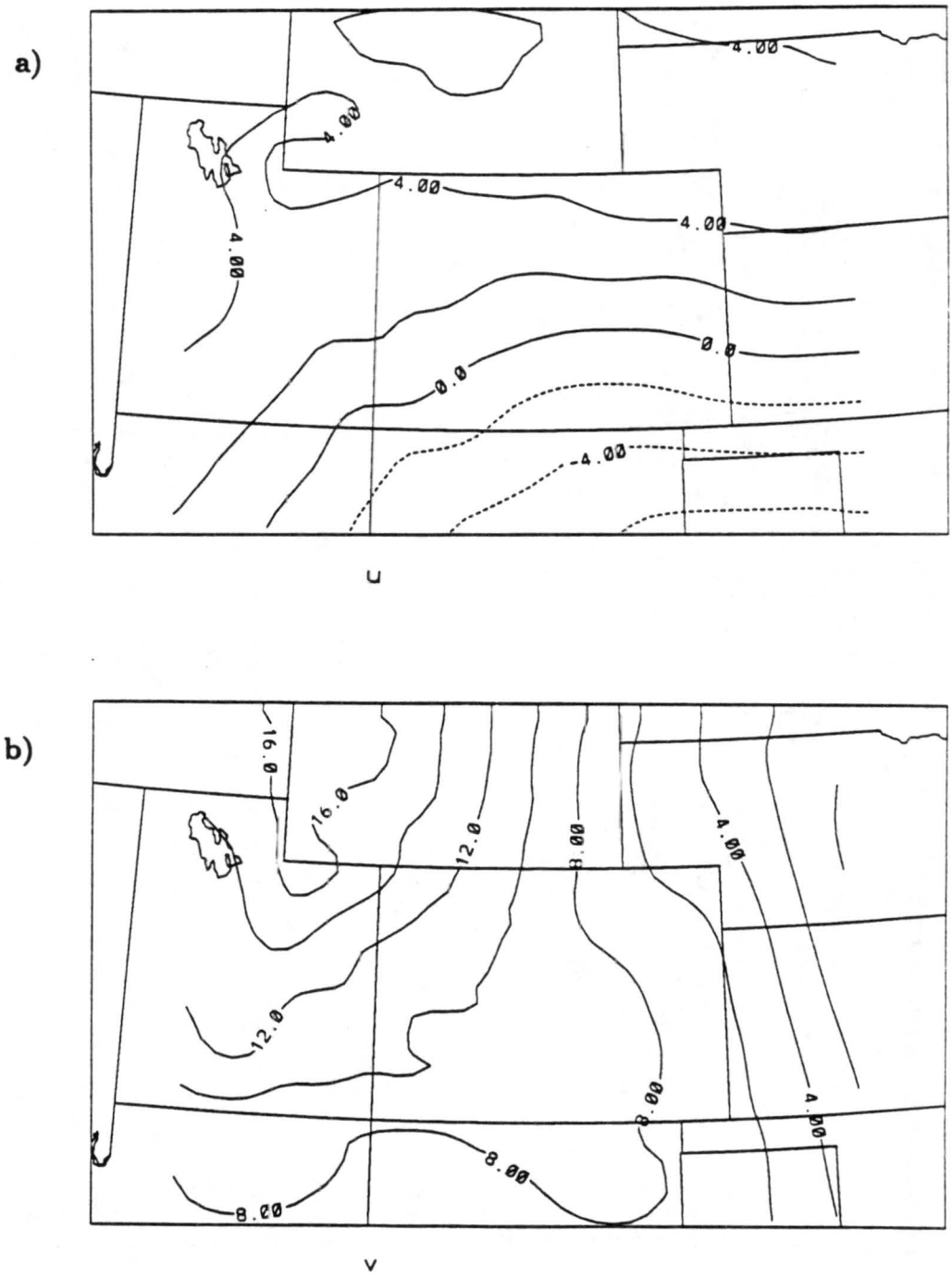

Figure 6.10: Fine grid horizontal cross-sections from Experiment 2 at 5.94 km above the surface for the a) u-component with 2.0 m/s intervals, b) v-component with 2.0 m/s intervals, c) w-component with 0.06 m/s contour intervals, d) potential temperature with 1°contour intervals, and e) total mixing ratio with contour intervals (labelled in $\times 10^{-2}$ g/kg) of 0.2 g/kg, all at 0000 UTC 30 July 1987.

Figure 6.10: Continued.

e)

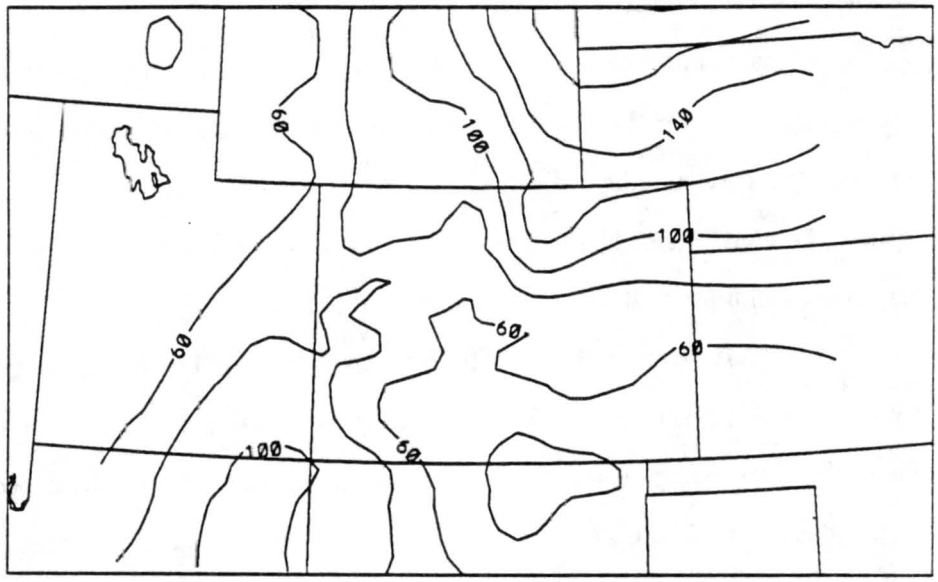

Figure 6.10: Continued.

The potential temperature field near the surface (Figure 6.9d) indicates that the warmest temperatures (315 K) were located over central Colorado while the coolest temperatures (300 K) were observed over the eastern plains. The areas with the warmest temperatures and the temperatures in the western most area compare well with those in the control run; however, the isolated areas of cooler temperatures were not predicted (leading to a much smoother field) and the temperatures over the eastern plains were almost 5 degrees cooler.

The total mixing ratio values around Colorado range from 8 g/kg over central Colorado to 11 g/kg over the southwest and southeast corners. The most noticeable difference between the total mixing ratio fields from this experiment and those in the control run is that the control run has values as low as 4 g/kg and the lowest values are located in southeast Colorado instead of a more central location.

The explicit accumulated rain field shows extremely low rain amounts over southern Colorado and northern New Mexico with a peak value of 0.048 mm in New Mexico. Similarly, Figure 6.9g reveals that the only area of simulated rain produced by the explicit microphysics at 0000 UTC was in north-central New Mexico with values only reaching 0.0021 g/kg.

6.4 Experiment 3 - 12 Hour Simulation With Forced Heating, Inferred From Observed Surface Rain

The model was initialized at 1200 UTC 29 July and integrated for 12 hours. The first 8 hours of this simulation are exactly the same as Experiment 2 (e.g. the model was initialized with microphysics and the RAMS cumulus parameterization activated). At 2000 UTC the modified cumulus parameterization scheme (sec 5.3) is applied to data over 120 grid points in north-central Colorado (out of 1428 grid points in grid 2), corresponding roughly to the area of rainfall coverage shown in the radar summary map of Figure 4.4c. A forced heating rate was applied for one hour at the rainfall rate (2.3 mm/hr) estimated from the PAM surface data. The duration of the latent-heat forcing was arbitrarily chosen as one hour because a constant heating rate was used, indicating the need of a relatively short forcing period since precipitation patterns are often highly variable

in time. On the other hand, too short a time period will not allow sufficient time for the vertical motion to respond to the heating and allow precipitation to be maintained after the forcing period. The other areas of the model domain continue to use the existing cumulus parameterization scheme during this one hour time period. During the remaining time (2100 UTC 29 July - 0000 UTC 30 July) the model is allowed to freely run with its own processes (similar to the beginning of the run) in hopes of producing more accurate QPFs. Of course, the low-level divergence and vertical motion field established during the period of applied heating will affect the model circulations during the subsequent forecast period.

The horizontal wind pattern at 0.10 km AGL (Figures 6.11a and b) is similar to that of the control run, however, the magnitudes of the east-west wind components are about 3 times greater and the northerly wind component over central Colorado is not broken up into isolated areas. The upper-level horizontal flow in this simulation (Figures 6.12a and b) closely resembles the upper-level flow in the control run. The only difference worth mentioning is the slightly higher (as much as 3 m/s higher in some areas) values of westerly wind over northern Colorado.

The vertical motion field near the surface (Fig 6.11c) is not affected at all by the inclusion of the estimated rain rate. A few small changes are observed in the w field at 5.94 km AGL (Fig 6.12c). Specifically, an area of weak ascent (less than 0.03 m/s) is located over the eastern plains of Colorado (while this area was characterized by descending air in Experiment 2) and slightly stronger speeds (typically less than 0.02 m/s higher) are observed.

The surface and upper-level potential temperature fields (Figures 6.11d and 6.12d, respectively) and the surface total mixing ratio field (Fig. 6.11e) are almost identical to the fields in experiment 2 at this time. So, once again the inclusion of the light rainfall did not have an influence on the model's predictions of these fields. However, the upper-level total mixing ratio field (Fig. 6.12e) shows slightly higher values of 1.8 g/kg (compared to 1.2 g/kg in the previous experiment) over the Colorado-Wyoming-Nebraska area.

The accumulated rain field at 0000 UTC 30 July from experiment 3 (Figure 6.11f) shows precipitation in the same area as predicted by Experiment 2 but the peak value

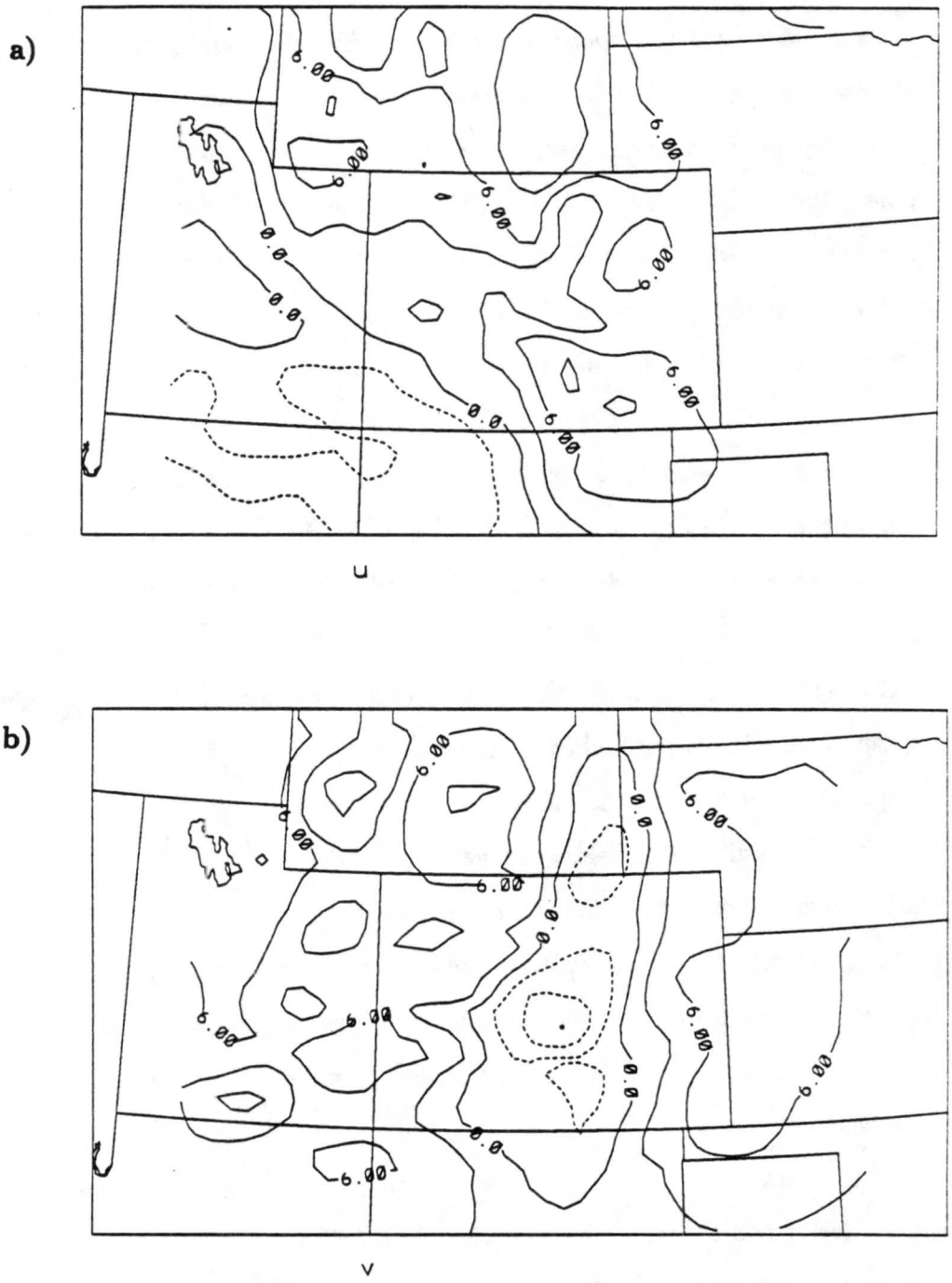

Figure 6.11: Fine grid horizontal cross-sections from Experiment 3 at 0.10 km above the surface for the a) u-component with 3.0 m/s intervals, b) v-component with 3.0 m/s intervals, c) w-component with contour intervals (labelled in $\times 10^{-3}$ m/s) of 0.03 m/s, d) potential temperature with 2°contour intervals, e) total mixing ratio with contour intervals (labelled in $\times 10^{-1}$ g/kg) of 1.0 g/kg, f) accumulative surface rain with 0.01 mm intervals, and g) rain mixing ratio with 9 $\times 10^{-4}$ g/kg contour intervals, all at 0000 UTC 30 July 1987.

c)

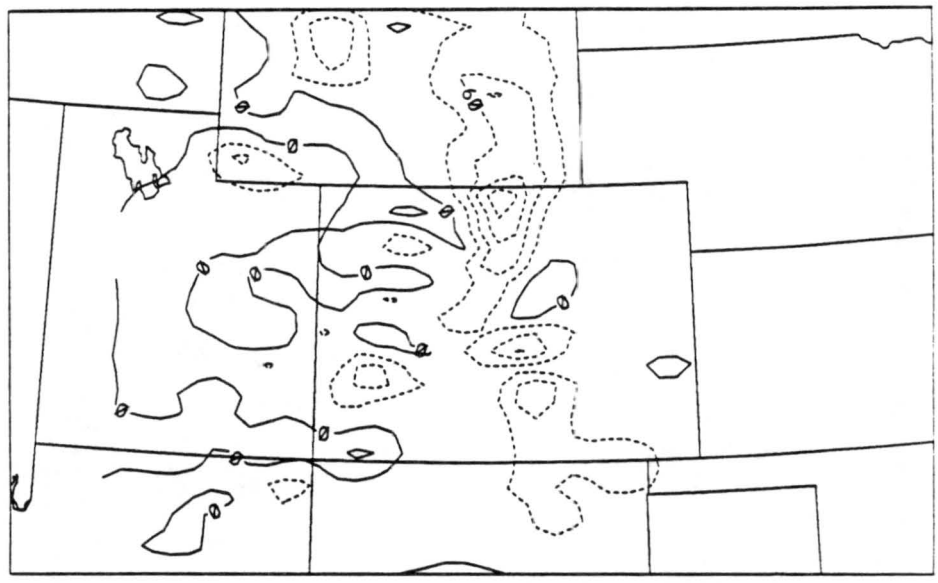

d)

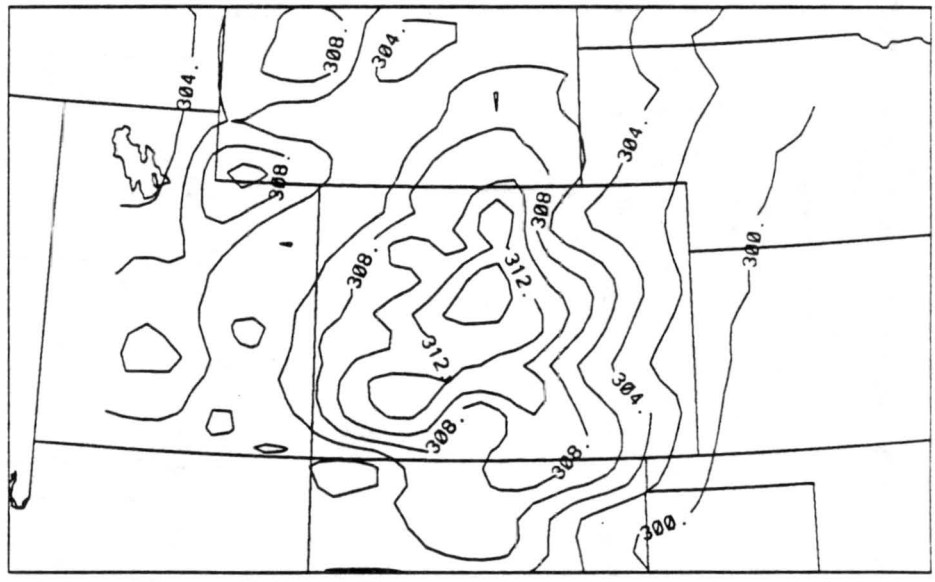

Figure 6.11: Continued.

e)

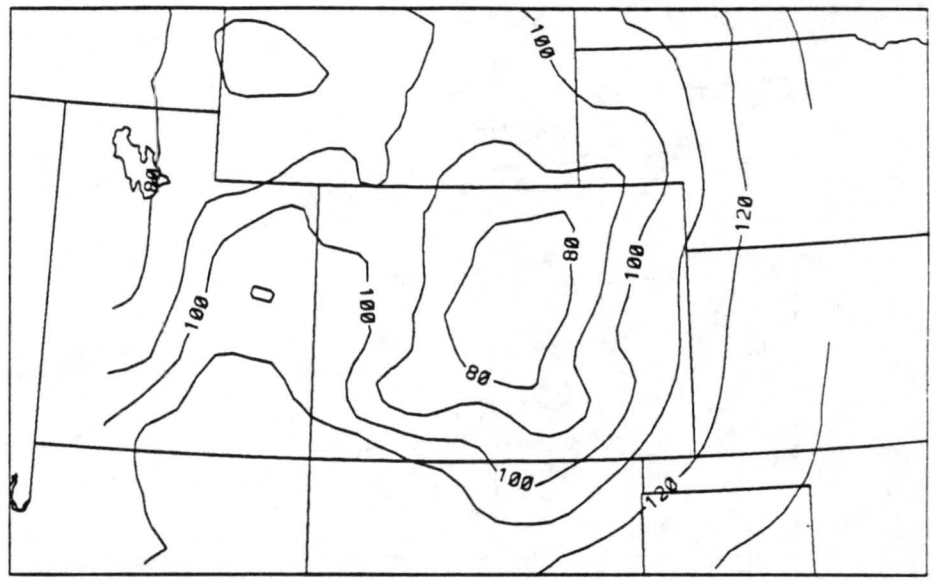

total mix ratio

f)

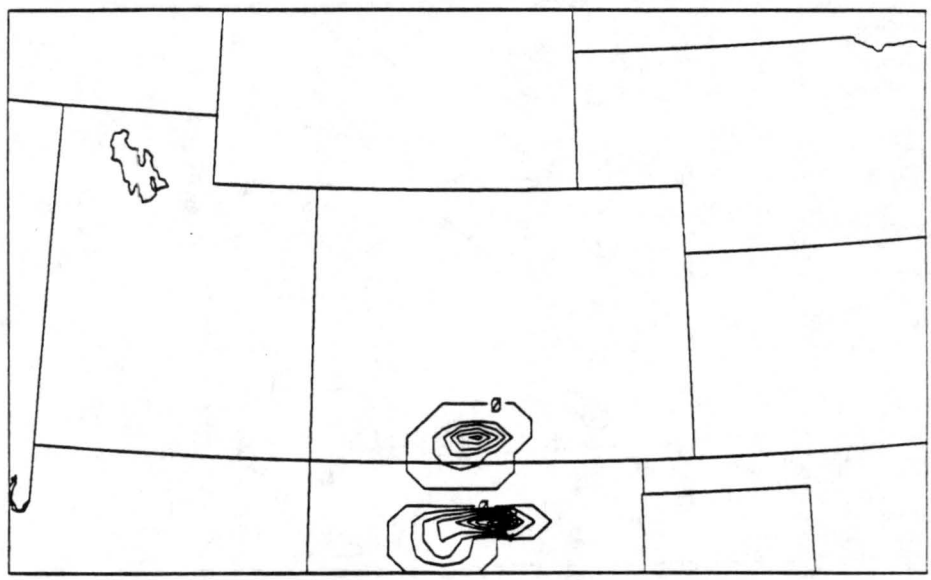

PRECIP. RAIN

Figure 6.11: Continued.

g)

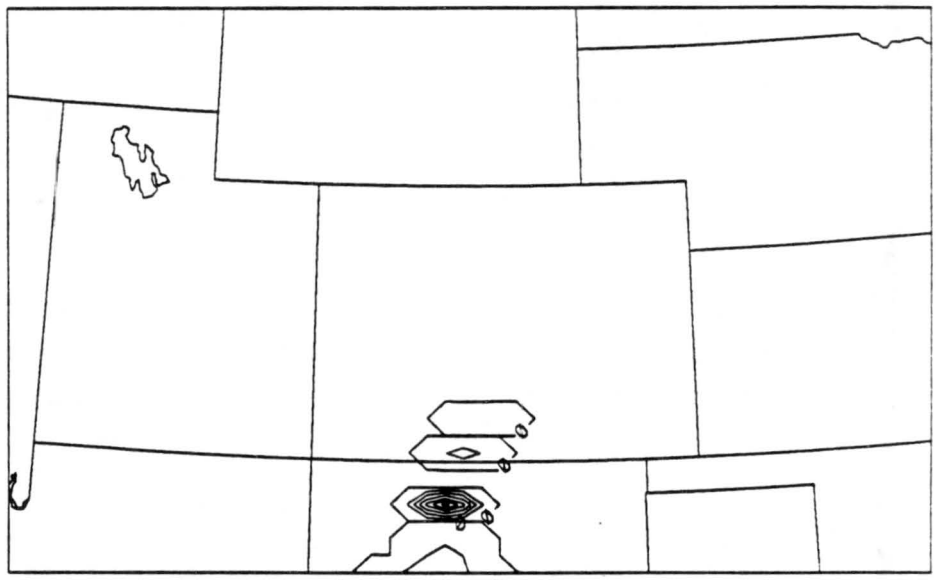

Figure 6.11: Continued.

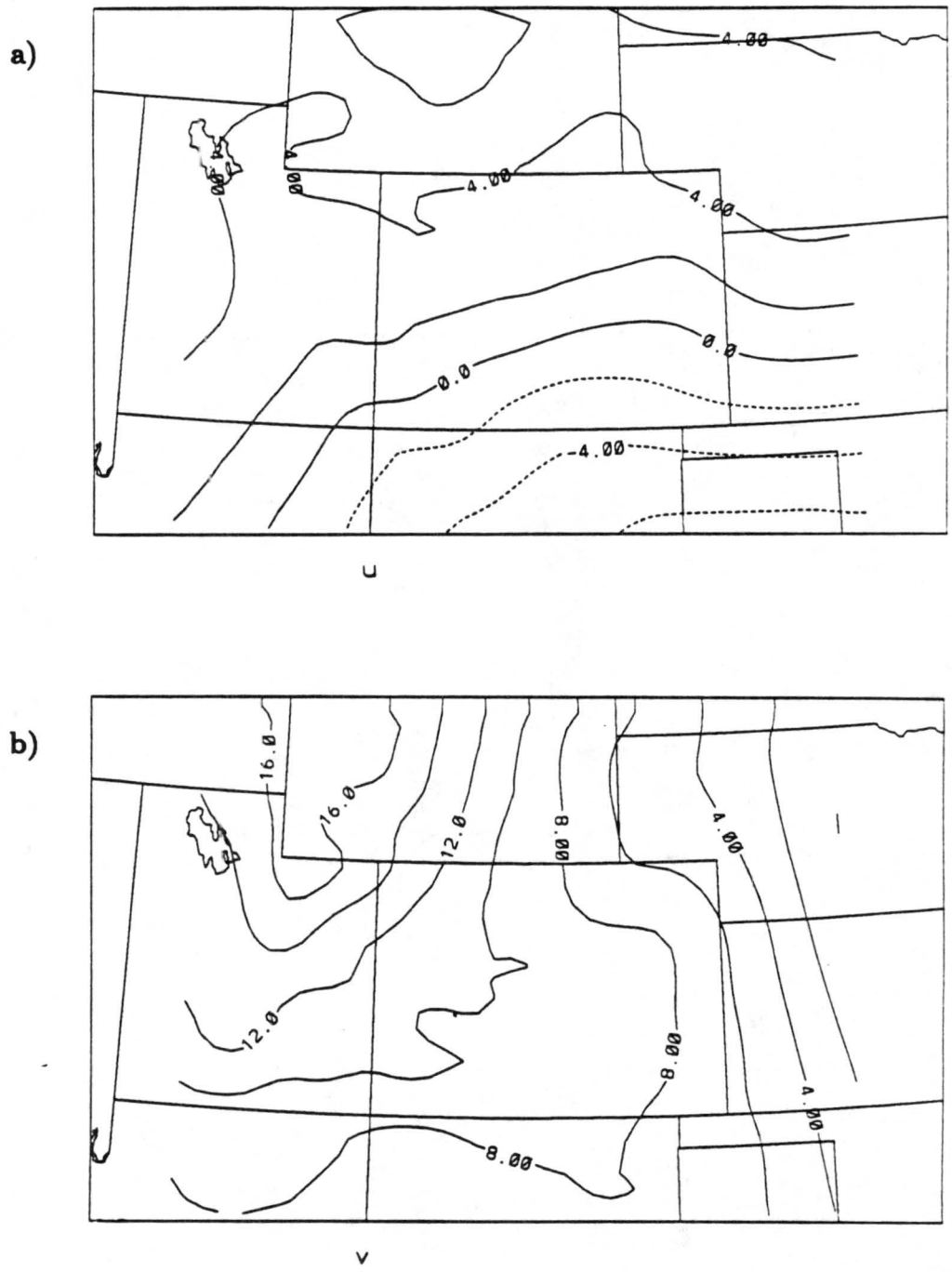

Figure 6.12: Fine grid horizontal cross-sections from Experiment 3 at 5.94 km above the surface for the a) u-component with 2.0 m/s intervals, b) v-component with 2.0 m/s intervals, c) w-component with 0.03 m/s contour intervals, d) potential temperature with 1°contour intervals, and e) total mixing ratio with contour intervals (labelled in $\times 10^{-2}$ g/kg) of 0.2, all at 0000 UTC 30 July 1987.

c)

d)

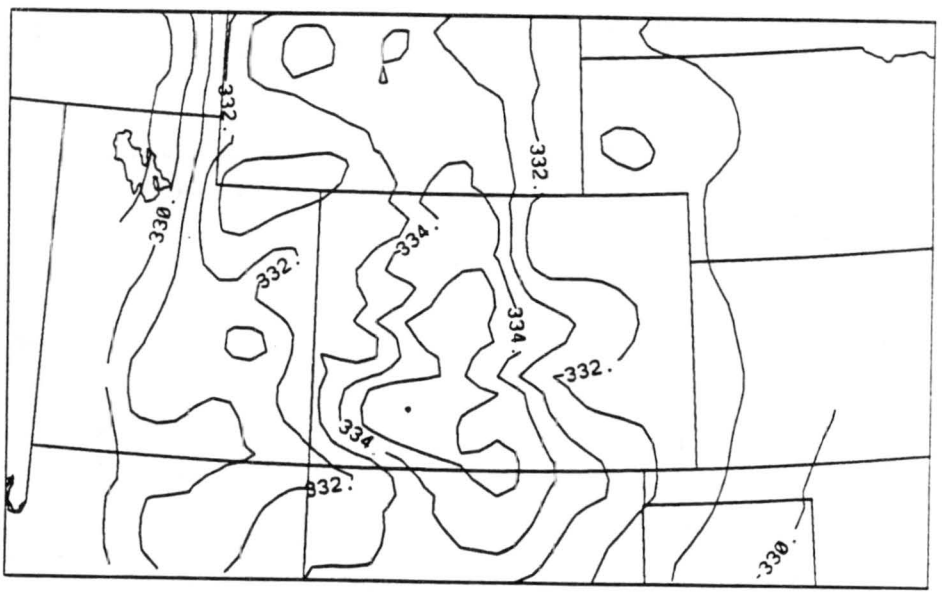

Figure 6.12: Continued.

e)

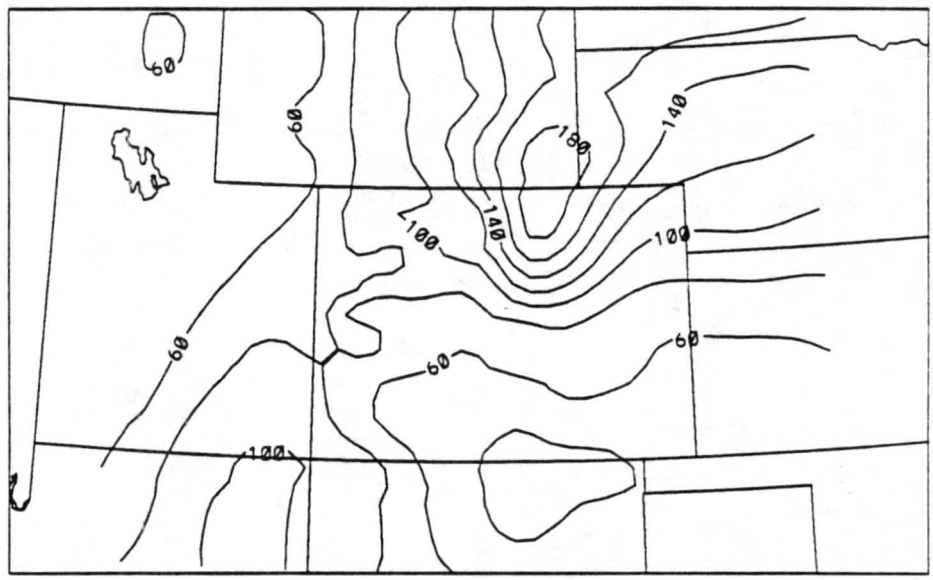

Figure 6.12: Continued.

in this simulation was 0.07 mm (compared to 0.048 mm from the previous experiment). Likewise, the near-surface rain mixing ratio field (figure 6.11g) was almost the same as the one in Experiment 2 except a slightly higher value of 0.0054 g/kg was noted and rain fell over a slightly larger area in this experiment. The similarities between the explicit accumulated rain and rain mixing ratio fields were expected since the other fields did not change at all or else only a slight change was noticed. Consequently, a rainfall rate of 2.3 mm/hr, inserted into the modified cumulus parameterization scheme, does not provide the model with heating rates strong enough to produce better QPFs, based on results from this simulation.

6.5 Experiment 4 - 12 Hour Simulation With Forced Heating, Inferred From Radar Data Using a Combined Z-R Relationship

This simulation is initialized at 1200 UTC on 29 July 1987 and run out to 12 hours of integration time. Full microphysics and the cumulus parameterizations scheme are turned on for the entire 12 hours. A rainfall rate of 7.1 mm/hr, estimated from Doppler radar using a Z-R relationship of $Z = 447R^{1.44}$ (obtained from averaging six various Z-R relationships – refer to section 4.3.2), over the CINDE are was used to calibrate the model's latent heat release for a one hour period beginning at 2000 UTC (2pm MDT) and ending at 2100 UTC. The forced heating was applied over the same 120 grid points as the previous experiment, and as before, the one hour duration was chosen because the forcing was constant; consequently, a longer period may not be representative of the heating rate. Therefore, with the exception of the magnitude of the forced, constant heating rate, Experiment 4 is identical to Experiment 3.

The 0000 UTC surface horizontal winds (Figures 6.13a and b) shows northwest wind colliding with southwest wind in eastern Colorado and western Nebraska. This is the same surface wind pattern that was observed in the control run and Experiments 2 and 3; consequently, no easterly wind was predicted over Colorado at the surface, which does not verify with the PAM mesonet data. However, easterly flow was simulated 2.95 km above the ground over the Wyoming-Colorado-Nebraska border reaching a maximum area coverage and speed, of 3 m/s, at 3.94 km (not shown).

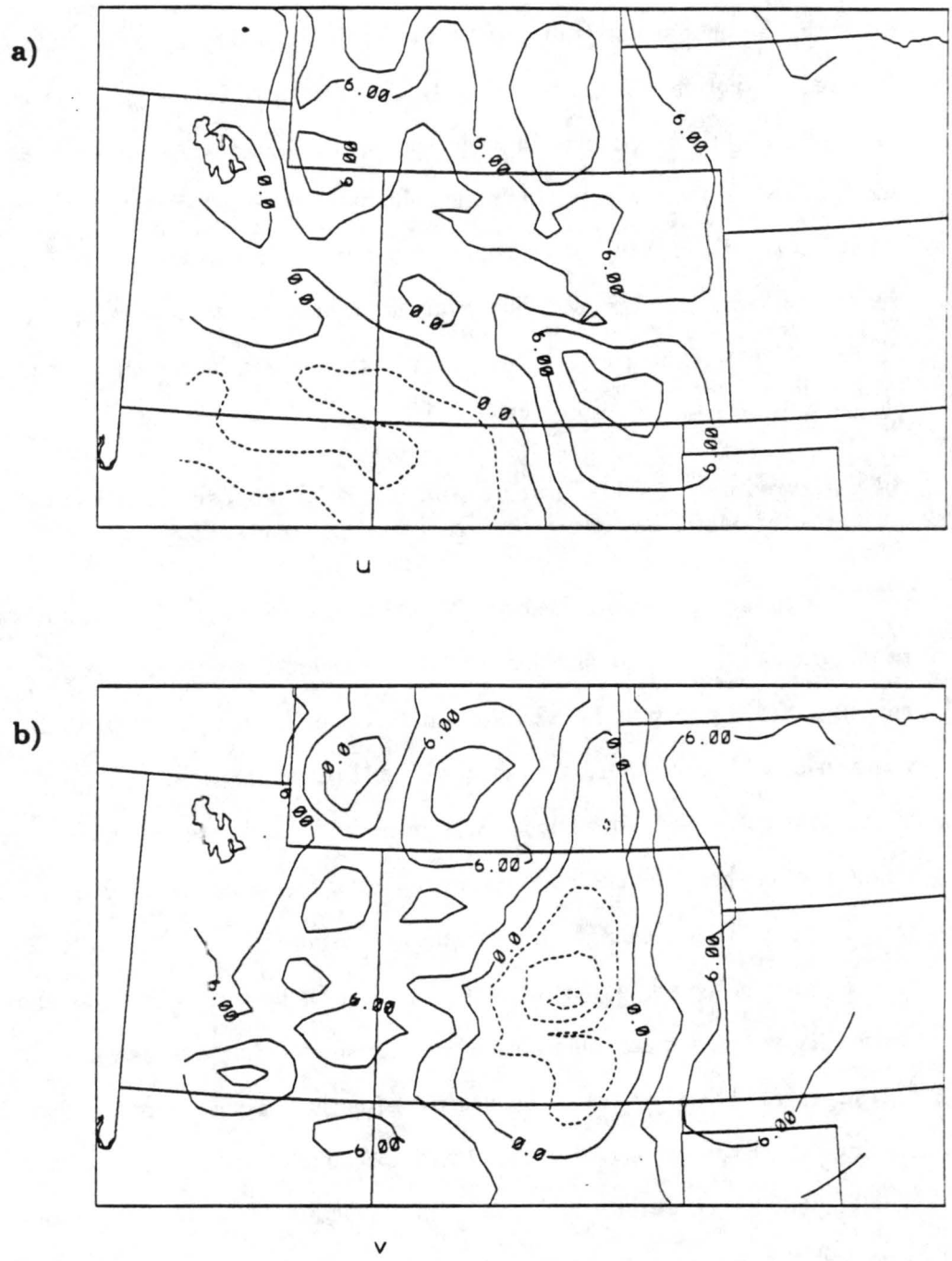

Figure 6.13: Fine grid horizontal cross-sections from Experiment 4 at 0.10 km above the surface for the a) u-component with 3.0 m/s intervals, b) v-component with 3.0 m/s intervals, c) w-component with contour intervals (labelled in $\times 10^{-3}$ m/s) of 0.03 m/s, d) potential temperature with 3°contour intervals, e) total mixing ratio with contour intervals (labelled in $\times 10^{-1}$ g/kg) of 1.0 g/kg, f) accumulative surface rain with 0.5 mm intervals, and g) rain mixing ratio with contour intervals (labelled in $\times 10^{-3}$ g/kg) of 0.02 g/kg, all at 0000 UTC 30 July 1987.

c)

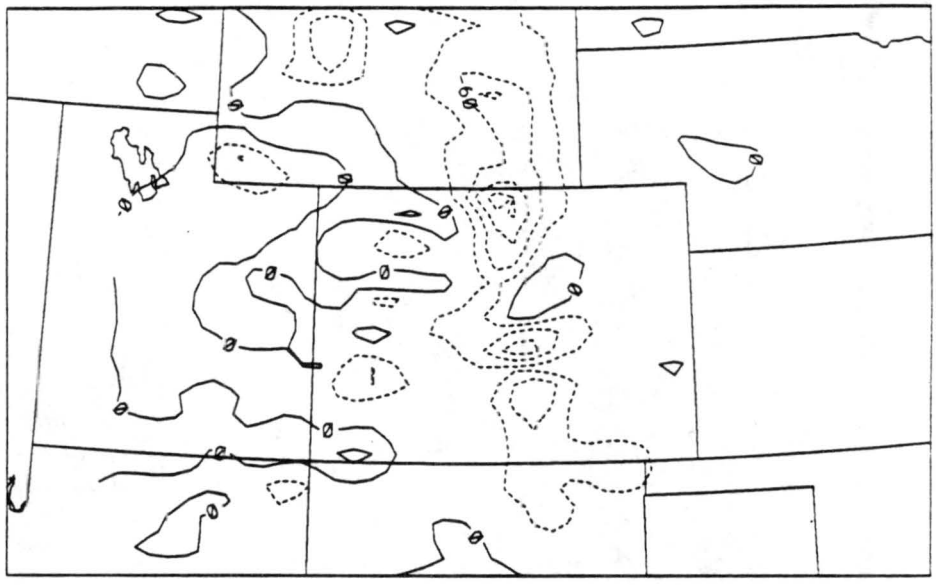

d)

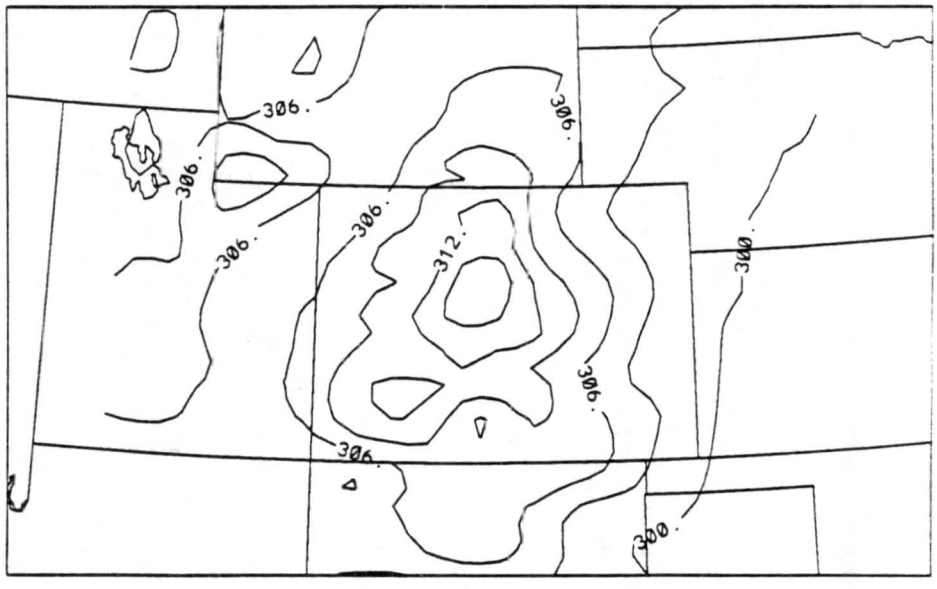

Figure 6.13: Continued.

e)

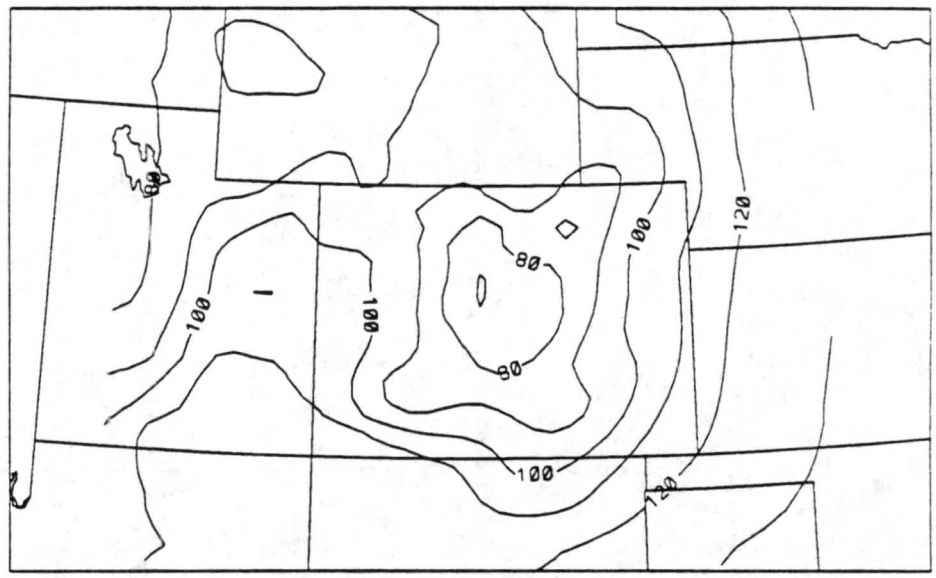

total mix ratio

f)

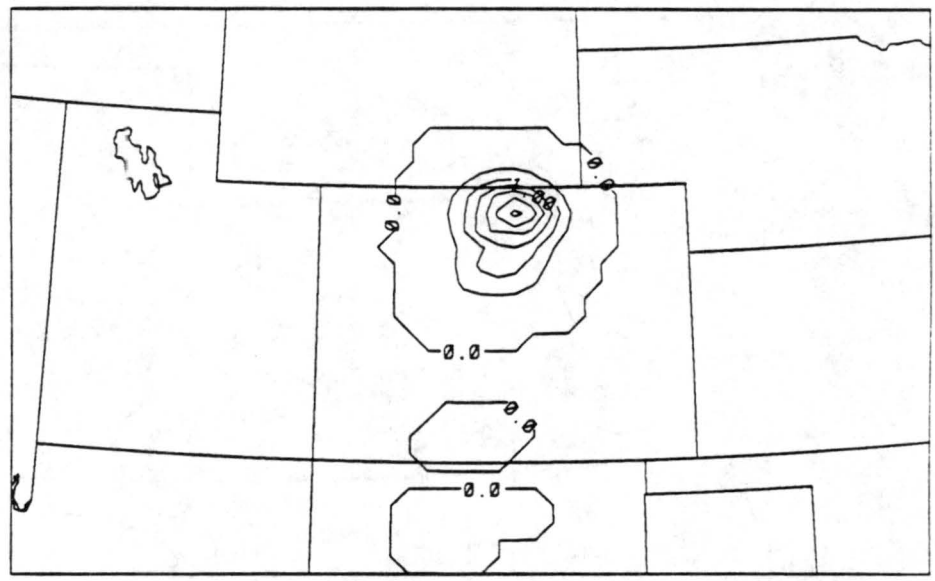

PRECIP. RAIN

Figure 6.13: Continued.

g)

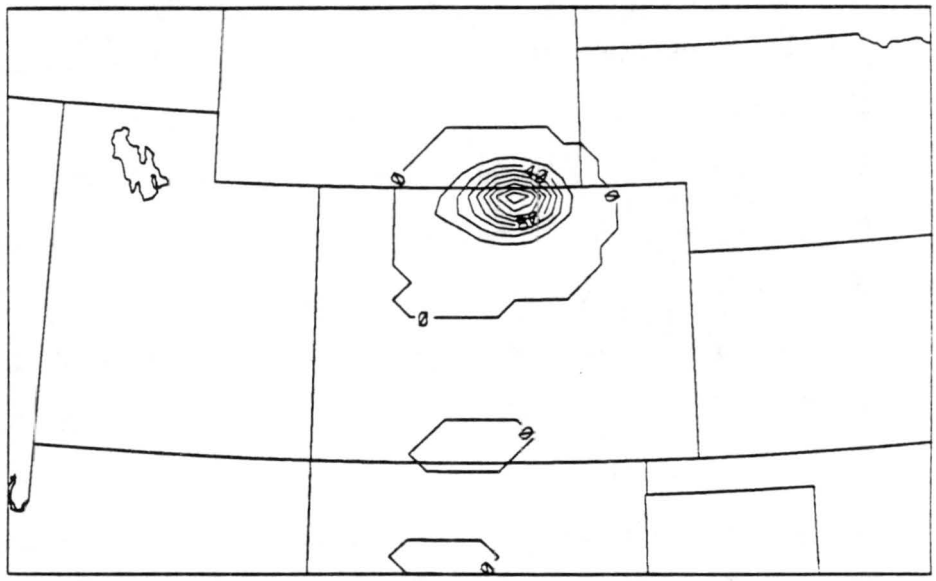

Figure 6.13: Continued.

In general, high pressure dominates the region in the upper elevations as depicted in the 5.94 km AGL plots in Figure 6.14. The high pressure is centered somewhere east of the southern Colorado, which corresponds well with the observed data, that placed the center of high pressure over the eastern Kansas-Oklahoma border. A small area of easterly flow along the Colorado-Wyoming border was also observed, indicating an area of upper-level divergence.

The vertical motion field near the surface (Figure 6.13c) is almost identical to the w field in Experiment 2 and 3, where once again Colorado is dominated by descending air as strong as -0.12 m/s and weak ascent of not quite 0.03 m/s located near Denver; however, the w field in the higher elevations is quite different. The most prominent feature observed in the w wind field at 5.94 km, Figure 6.14c, is the strong ascent over the Colorado-Wyoming border. The ascending region is located in the same area where the strongest surface rain (see Figure 6.13f) is predicted, with values as high as 0.28 m/s. Recall that Experiment 2 had downdrafts in this area at 5.94 km AGL.

The potential temperature and total mixing ratio fields at 0.10 km AGL are the same as those predicted in the previous 12 hour simulations, thus, incorporating a rain rate of 7.1 mm/hr into the model run has no affect on the prediction of these fields. The most significant feature of total mixing ratio field at 5.94 km (Figure 6.14e) is its maximum value of 3.5 g/kg located along the Colorado-Wyoming border. This is more than 2 g/kg higher than the values shown in both the control run and Experiment 2, and almost 1.5 g/kg higher than Experiment 3 values. However, the majority of this increase is probably due to the additional moisture added when a convective precipitation rate of 7.1 mm/hr was used to develop a convective system in northeast Colorado.

The accumulated rain field (Figure 6.13f) has a maximum value of 3 mm located near the Colorado-Wyoming border. The accumulated rain is less than the forced 7.1 mm/hr rain rate since the simulated rainfall depicted in these are produced by explicit microphysics and not by the cumulus parameterization scheme. Even though the 3 mm forecasted in this experiment is much smaller than the 18 mm of rain that fell over one of the rain gauges in the CINDE network, this is a significant improvement compared to the

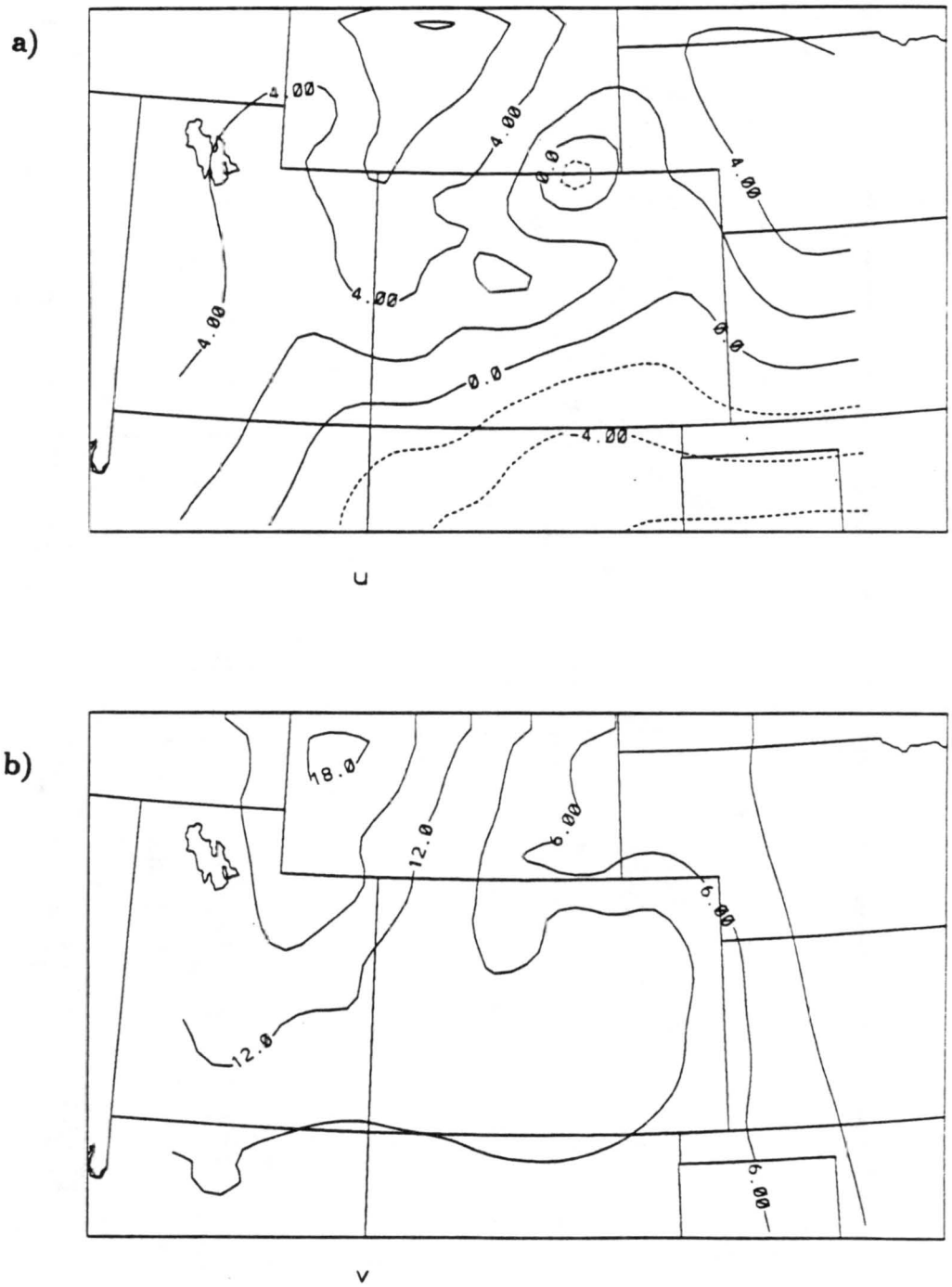

Figure 6.14: Fine grid horizontal cross-sections from Experiment 4 at 5.94 km above the surface for the a) u-component with 2.0 m/s intervals, b) v-component with 3.0 m/s intervals, c) w-component with 0.07 m/s contour intervals, d) potential temperature with 1°contour intervals, and e) total mixing ratio with contour intervals (labelled in $\times 10^{-2}$ g/kg) of 0.5, all at 0000 UTC 30 July 1987.

c)

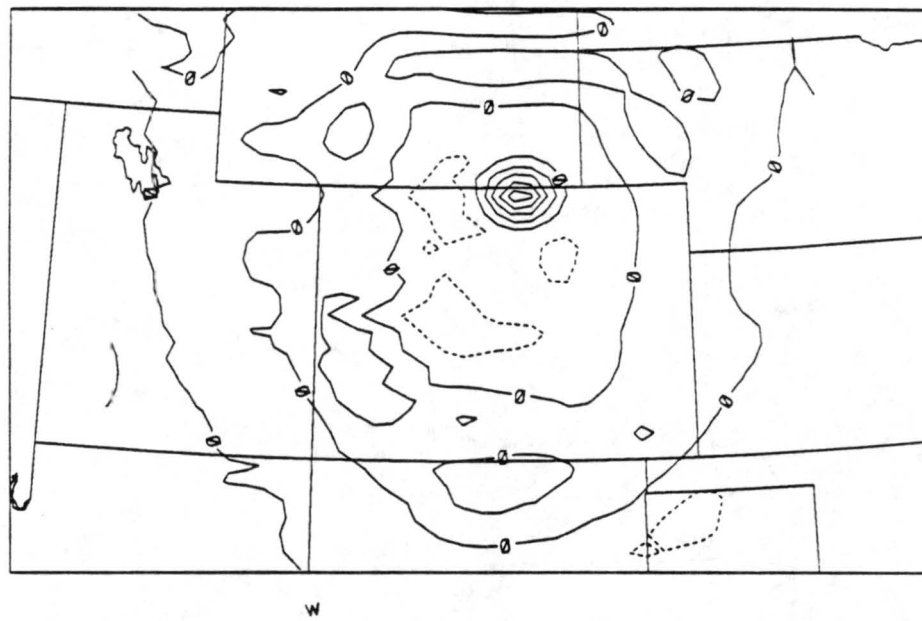

d)

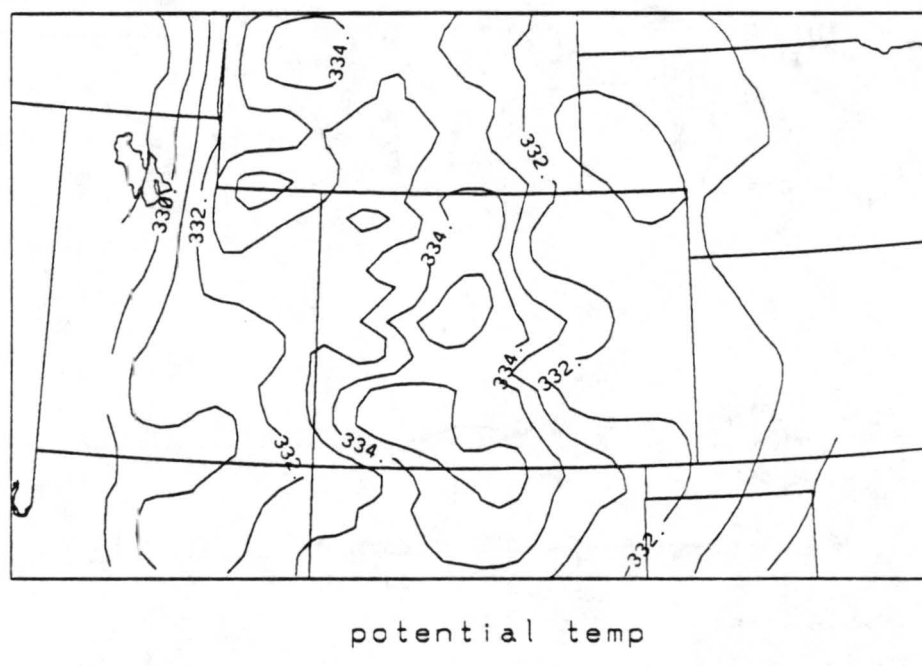

Figure 6.14: Continued.

e)

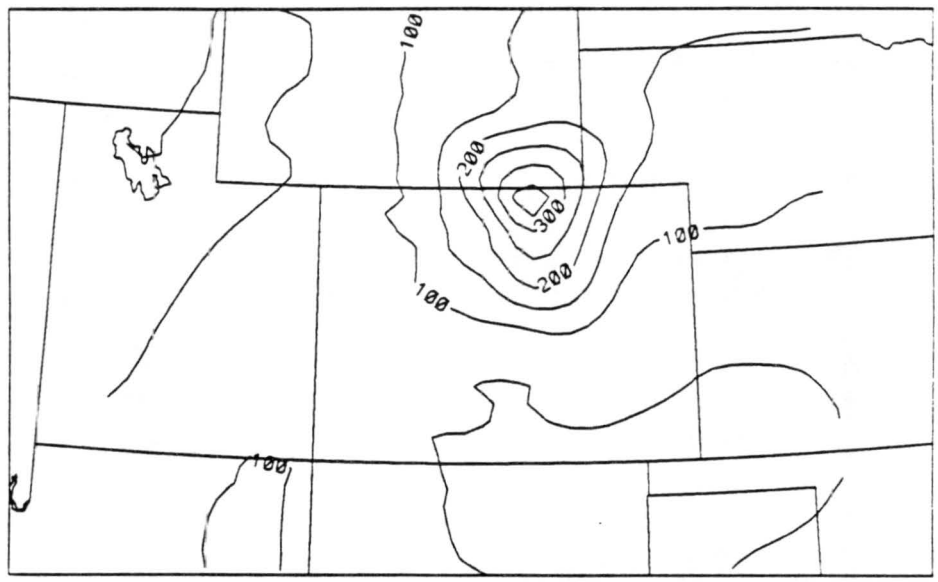

Figure 6.14: Continued.

previous 12 hour simulations which failed to forecast any rain northern Colorado. Also, despite the small values, this area of predicted rainfall is positioned accurately according to the radar summary map at 0035 UTC (Figure 4.4e) but the observed PAM data indicates that the peak value is centered northwest of its actual location. Light rain is also predicted in southern Colorado and northern New Mexico with accumulations of less than 1 mm. Rain in northern Colorado is predicted for the first time in this simulation but the model dynamics are still not strong enough to produce convective precipitation. Nevertheless, this simulation did produce a significant change in the upward vertical motion and the accumulated amount and location of surface rainfall simulated at 12 hours integration time.

6.6 Experiment 5 - 12 Hour Simulation With Forced Heating, Inferred From Radar Data Using a Marshall-Palmer Z-R Relationship

Experiment 5 is identical to Experiment 4 except a rainfall rate of 11.4 mm/hr was used to force the release of latent heat in the model over the same 120 grid points in northeast Colorado for the same one hour duration (2000-2100 UTC). The rainfall rate was estimated from the same Doppler radar data, over the CINDE area, used in Experiment 4; however a Marshall-Palmer Z-R relation ($Z = 200R^{1.6}$) was used for this experiment.

The near-surface predicted winds at 0000 UTC on 30 July for Experiment 5 are shown in Figure 6.15. The u wind field indicates westerly winds as strong as 9 m/s over much of Colorado and the surrounding States. Easterly winds were observed in the extreme southwestern part of Colorado, southeast Utah, northern Arizona and northwestern New Mexico. There was an additional pocket of light easterly winds over the northern part of central Colorado. The v-component (Fig. 6.15b) shows that the only area of northerly flow is located over central Colorado, extending the length of the state. Thus, the horizontal wind pattern reveals a north/south convergence line east of the Rockies that separates northwest flow west of the line and southwest flow east of the line.

The general pattern of the horizontal wind field is similar to the pattern from the control run, however, there are a few differences that should be mentioned. One noticeable

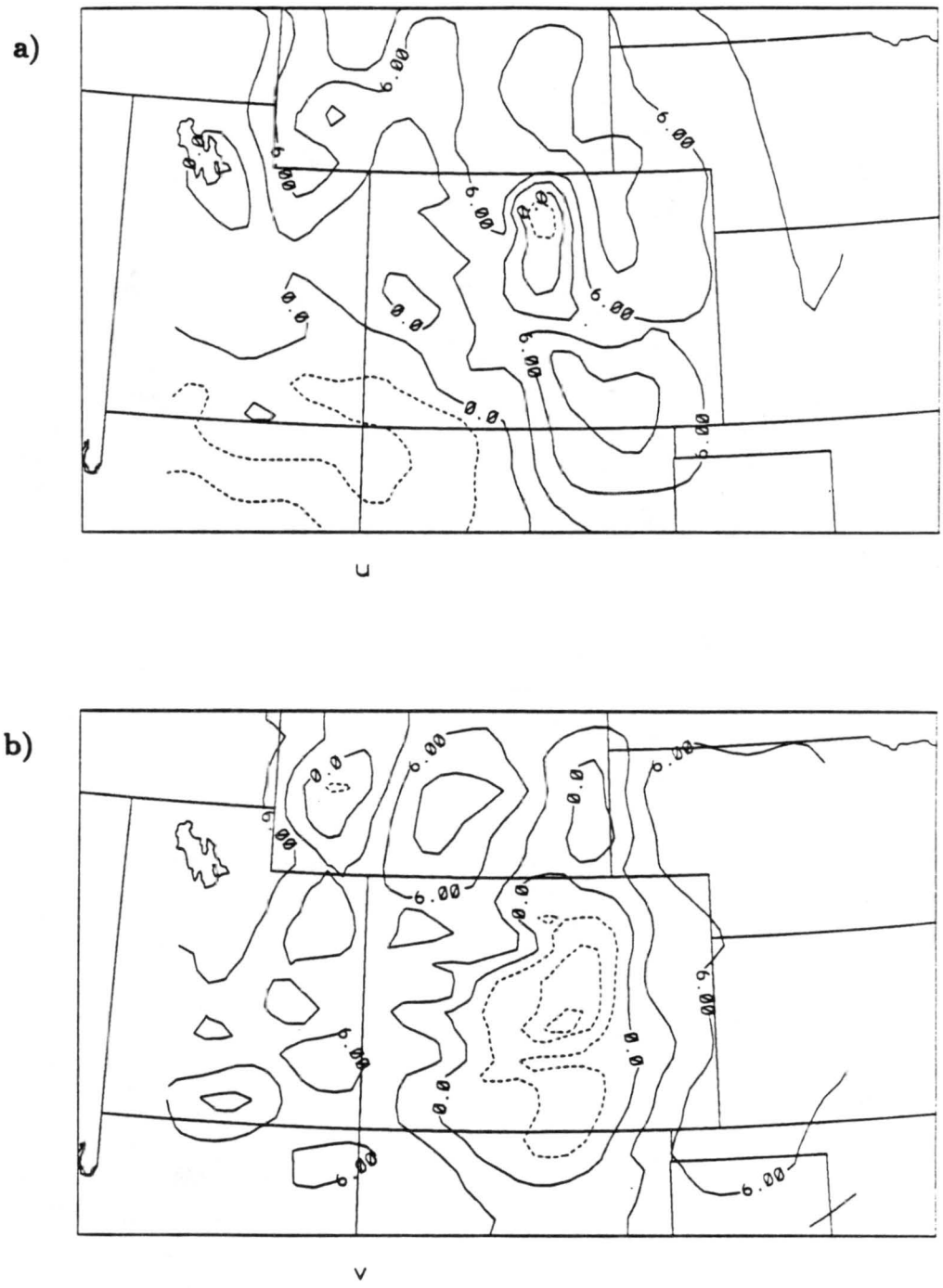

Figure 6.15: Fine grid horizontal cross-sections from Experiment 5 at 0.10 km above the surface for the a) u-component with 3.0 m/s intervals, b) v-component with 3.0 m/s intervals, c) w-component with contour intervals (labelled in $\times 10^{-3}$ m/s) of 0.03 m/s, d) potential temperature with 3°contour intervals, e) total mixing ratio with contour intervals (labelled in $\times 10^{-1}$ g/kg) of 1.0 g/kg, f) accumulative surface rain with 2.0 mm intervals, and g) rain mixing ratio with contour intervals (labelled in $\times 10^{-3}$ g/kg) of 0.07 g/kg, all at 0000 UTC 30 July 1987.

c)

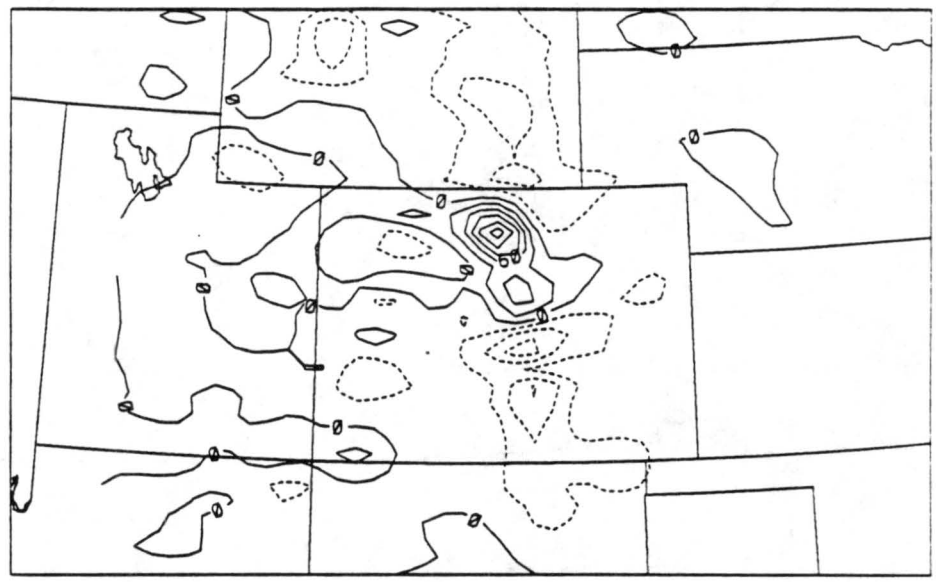

d)

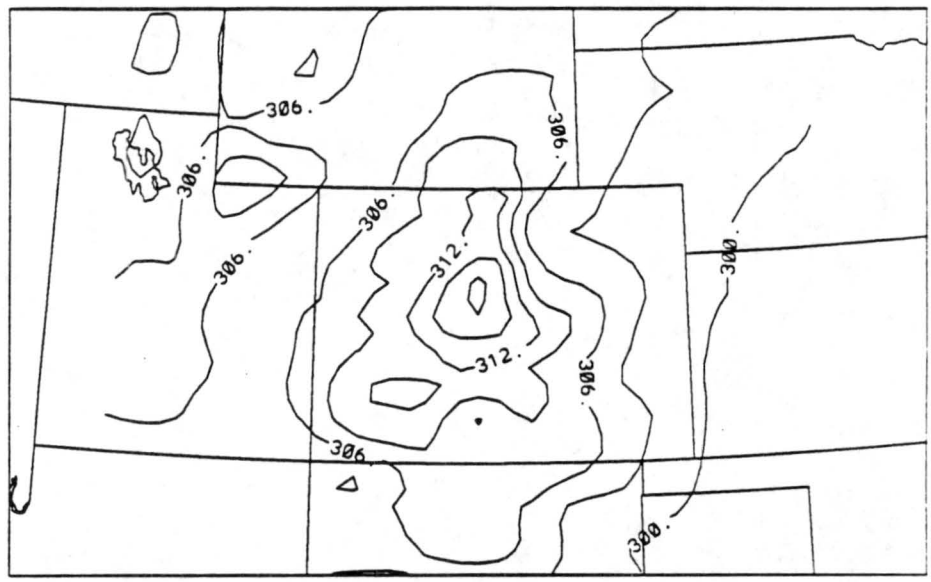

Figure 6.15: Continued.

e)

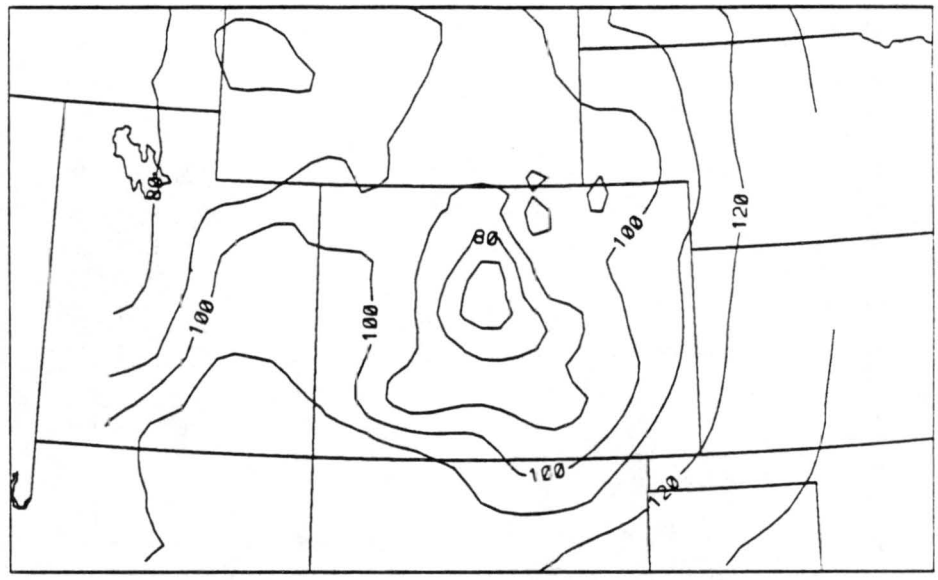

f)

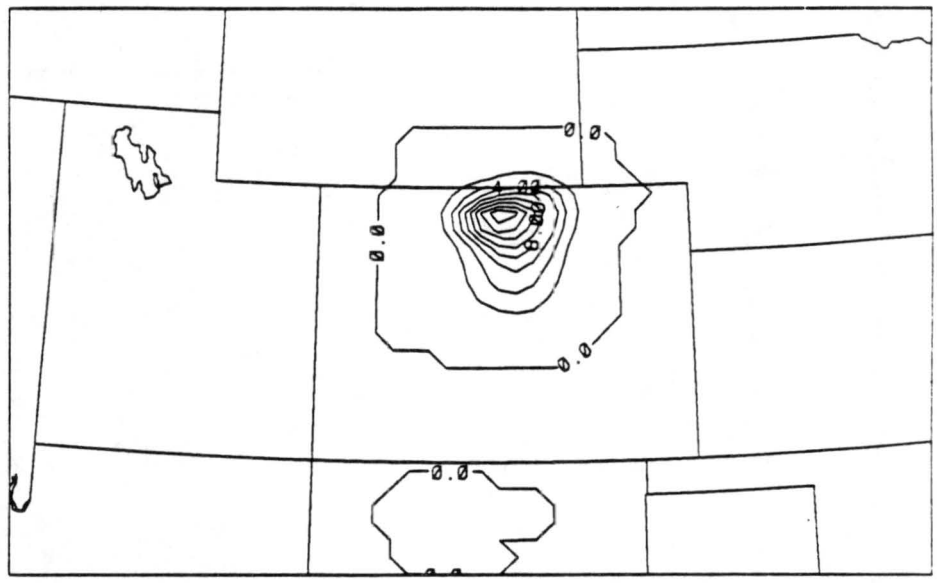

Figure 6.15: Continued.

g)

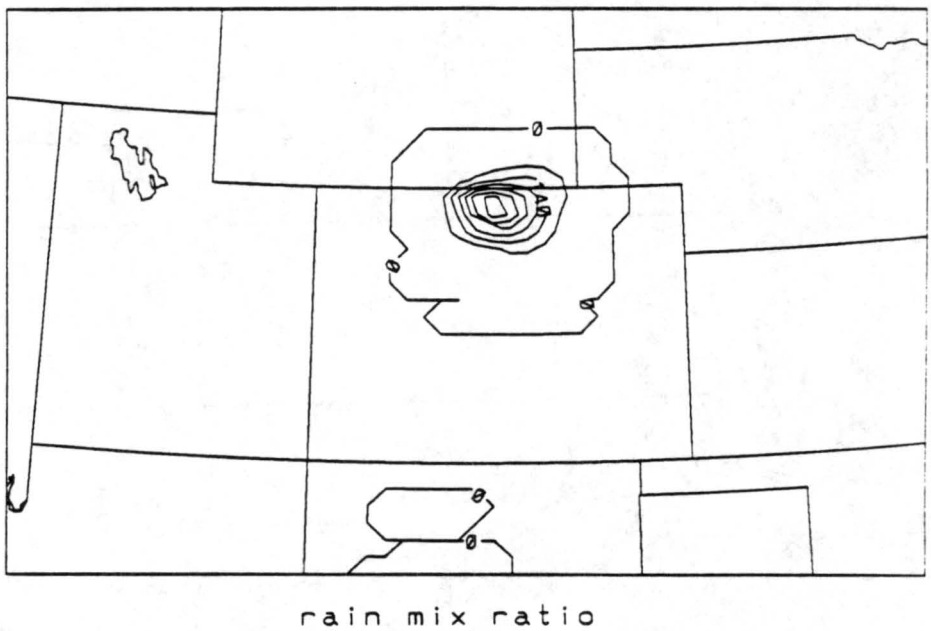

Figure 6.15: Continued.

difference is the magnitudes of the east-west wind speeds; the speeds in this run are about 3 times larger than those of the control run. Another difference is that unlike the control run, this model run did predict easterly flow at the surface in central Colorado. This compares better to the observed mesonet data than any other 12 hour simulation; although, the area of easterlies is predicted northwest of the observed pattern. Finally, the northerly wind over central Colorado had a more continuous flow in this run indicating that the model was not able to predict the separate storms.

The most significant features at 5.94 km AGL (shown in Figure 6.16) are the area of easterly flow located along the Colorado-Wyoming border and the strong southerly wind component in northeast Colorado. These features were not shown in the NMC data (e.g. the control run) but that is not surprising since the low-level convergence was much weaker in that case. The stronger convergence near the surface created stronger upper-level divergence which was not diminished as easily by the southwesterly winds associated with the high pressure in higher elevations.

An interesting feature observed in the vertical motion field near the surface (Fig. 6.15c) is that, while all the other runs showed most of Colorado (especially the northern part) to be dominated by descending air this run had a large area of upward motion in northern Colorado with speeds reaching 0.15 m/s. At 5.94 km a stronger and larger area of ascent, which is shifted slightly north of its surface location, is observed with values as high as 0.36 m/s (Figure 6.16c). The strongest updraft at this time occurred at 2.95 km (the figure is not shown) where a value of 0.66 m/s was simulated.

The surface potential temperature and total mixing ratio fields, figures 6.15d and e, respectively, are almost identical the fields predicted in the other 12 hour model runs. Thus, it appears as if the inclusion of the rain rate has no impact at all on these fields. However, at 5.94 km the total mixing ratio field has values higher than any other model run. Its maximum value of 4.2 g/kg is more than 3 g/kg higher than the control run value in the same area.

Figure 6.15f shows the accumulated rain field with peak values (16 mm) located in north-central Colorado (in the same area as the strongest upward vertical velocity). This

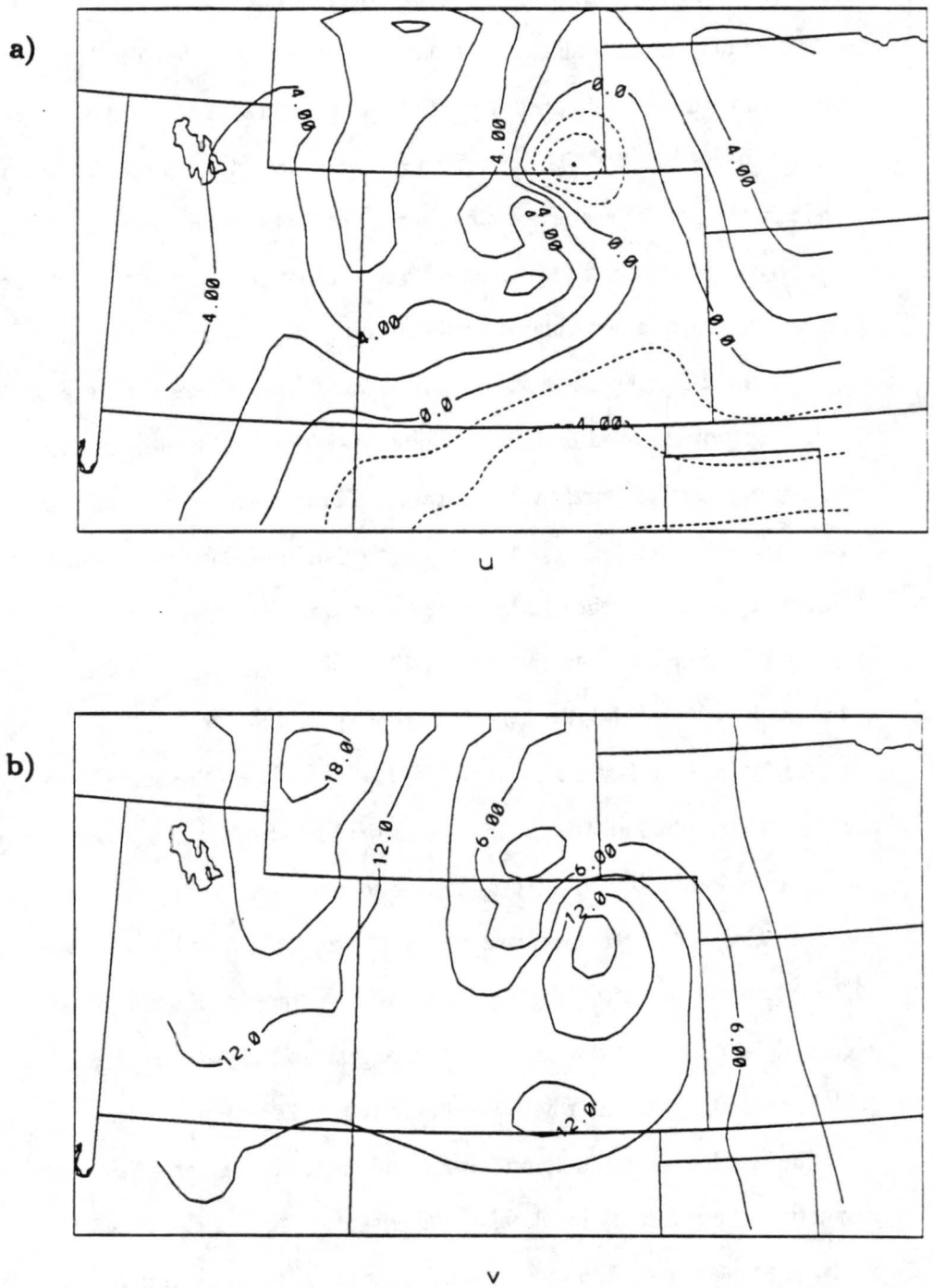

Figure 6.16: Fine grid horizontal cross-sections from Experiment 5 at 5.94 km above the surface for the a) u-component with 2.0 m/s intervals, b) v-component with 3.0 m/s intervals, c) w-component with 0.06 m/s contour intervals, d) potential temperature with 1°contour intervals, and e) total mixing ratio with contour intervals (labelled in $\times 10^{-2}$ g/kg) of 0.6, all at 0000 UTC 30 July 1987.

c)

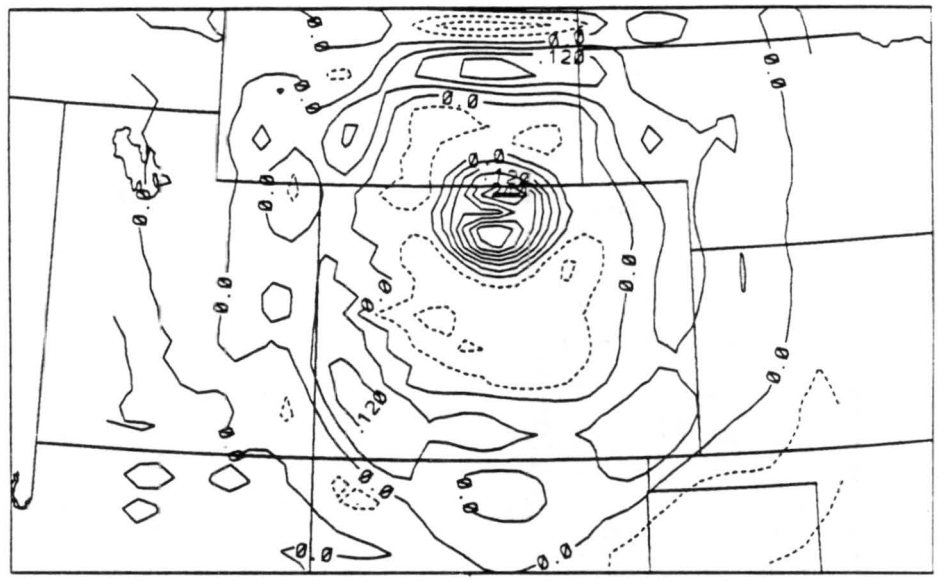

d)

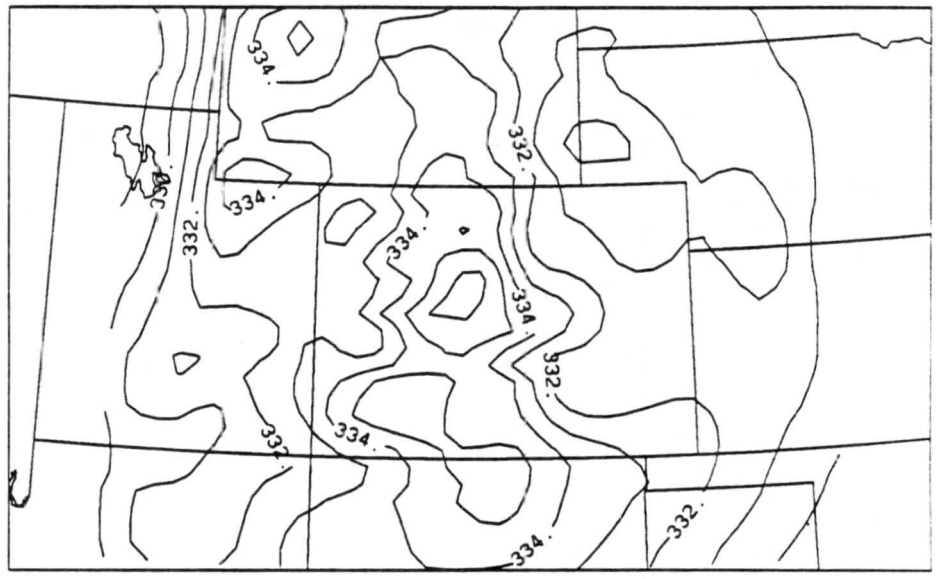

Figure 6.16: Continued.

e)

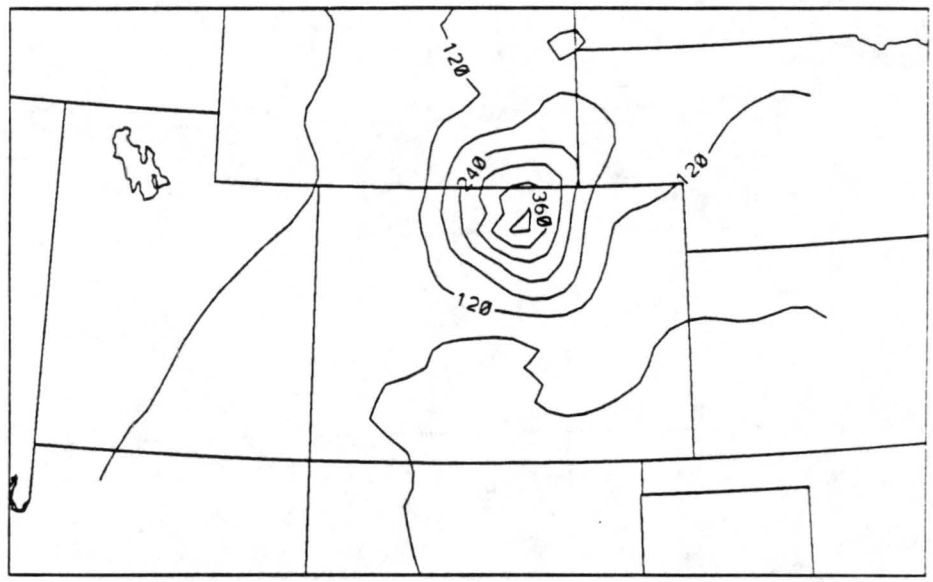

Figure 6.16: Continued.

value compares reasonable well with the 18 mm of observed accumulated rainfall over one of the PAM rain gauges. The rain mixing ratio field at 0000 UTC reveals a similar pattern with a peak value of 0.42 g/kg (located in the same area) which is higher than the previous maximum value of 0.16 g/kg shown in Experiment 4 (figure 6.13f). As mentioned in the previous sections, the moisture fields came from the explicit microphysics and not the cumulus parameterization scheme.

Chapter 7

DISCUSSIONS

7.1 12 vs. 24 Hour Simulation

Comparisons between Experiments 1 and 2, two simulations that were identical in every way except the first one was integrated for an additional 12 hours (both ended at 0000 UTC 30 July 1987), revealed some interesting features. The additional 12 hours provided the model with enough time to predict a surface level convergence line separating northwesterly and southeasterly winds. This is the same horizontal wind pattern that was observed by the PAM data; although the simulated wind speeds are weaker. Warmer potential temperatures (as much as 8°warmer) were also predicted by the 24 hour simulation, covering a larger area and positioned east of the maximum potential temperature field in the 12 hour simulation. The warmer temperatures are located in the same area as the convergence line and compares well to the maximum temperature reported by the PAM stations. The strongest rain mixing ratio in and around northeast Colorado was located in east central Wyoming (the same area as the upper-level, maximum ascent of air), with a peak value of 0.08 g/kg indicating that the 24 hour forecast produced a weaker storm too far north of its northeast Colorado location (based on the synoptic and mesoscale data). Nevertheless, this was still a better forecast than the one produced by the 12 hour model run with no forced heating, which only produced a very small and weak area of upward motion in the northeast Colorado region and consequently no precipitation was predicted.

Convective storms typically form as air rises, expands, and cools. The primary lifting mechanisms responsible for the development of clouds are convection (caused by warm air rising), topography, low-level convergence of air and uplift along weather fronts (Ahrens,

1982). Despite the low-level convergence and warmer temperatures predicted in northeast Colorado for the 24 hour simulation (Experiment 1), the only storm forecasted in that region was too far north of its observed location. This indicates that another method is required to produce better QPFs in a shorter time period.

7.2 Model Heating vs. Forced Heating

The 12 hour simulation that used the original cumulus parameterization scheme in RAMS (Experiment 2) clearly produced results that were not strong enough to support the model dynamics required to generate the localized convective storm in northeast Colorado. The convergence of northwest and southwest air flow near the surface (which is different than the observed northwest-southeast convergence) was not strong enough to produce rising motion (except for a few very weak and small, isolated areas) in the simulated vertical motion field. Consequently, no precipitation was observed in the area. The probable cause of the lack of sufficient model dynamics in the predicted fields is that the spatial separation of the data used to initialize the model was to large to resolve all the terrain-induced and surface forcing features associated with this convective storm. and the model did not have sufficient time to develop these features.

In an attempt to produce a better short-range QPF, precipitation rates estimated from the observed storm in northeast Colorado were incorporated into the model over the larger area of rainfall, indicated by the larger-scale radar summaries, to force the release of latent heating in the storm area. The goal was to determine if the experiments with the forced heating would greatly improve the QPF because the time required to generate the mesoscale features should be reduced, since the precipitation rates are guiding the model to the location and amount of heating observed in the region.

Results from the forced heating experiments indicate that the weaker estimated precipitation rate (2.3 mm/hr) applied over a one hour time period (Experiment 3) has no impact on the results. However, the larger precipitation rate estimates of 7.1 and 11.4 mm/hr, applied over the same one hour time period (Experiments 4 and 5, respectively) generate improved mesoscale dynamics. The simulated near-surface fields in Experiment

4 are unaffected by the forced heating rates inferred from the 7.1 mm/hr rain rate but noticeable changes were observed in a few of the upper-level fields and these changes produced light surface precipitation in the area of interest. The fields affected the most by the forced heating were the vertical motion and total mixing ratio fields. To examine further the effects of the forced heating on the 12 hour simulations, the 0000 UTC 30 July vertical profiles of the w field at y = 40.6°N are shown in Figure 7.1. Figure 7.1c clearly illustrates the relatively strong vertical ascent 3 km above the surface at a longitude of 105°W, compared to the vertical motion fields with no forced heating (Figure 7.1a) or weaker forced heating (Figure 7.1b).

Experiment 5 (Figure 7.1d) reveals that the maximum ascent of vertical is much stronger than the predicted values from any other simulation. This simulation (which released the strongest amount of latent heat, based on rain rates of 11.4 mm/hr) was the only 12 hour run to predict winds with an easterly component and relatively strong ascent near the surface. Consequently, this is the only experiment to predict a maximum accumulated precipitation amount (16 mm) that compares well with the observed amount, from the PAM stations, of 18 mm. Most of this amount came from the explicit precipitation (not the cumulus parameterization scheme) which was initiated by explicit rising motions.

Comparing results from the 12 hour simulation that used the model-generated heating rates for the entire time to those that used forced heating rates for part of the run show that the simulations with the forced heating can lead to better QPFs; however, this is highly dependent on the magnitude of precipitation rates inserted in the model.

7.3 Sensitivity to Estimated Rain Rates

Precipitation rates were estimated by different methods to examine the model's sensitivity to forced heating rates, based on these precipitation rates. One estimate was obtained from surface data and the other two were estimated from radar reflectivities, using two different Z-R relationships (see section 4.3 for details). As mentioned above, results from Experiments 3, 4 and 5 indicate that no changes occurred in the potential

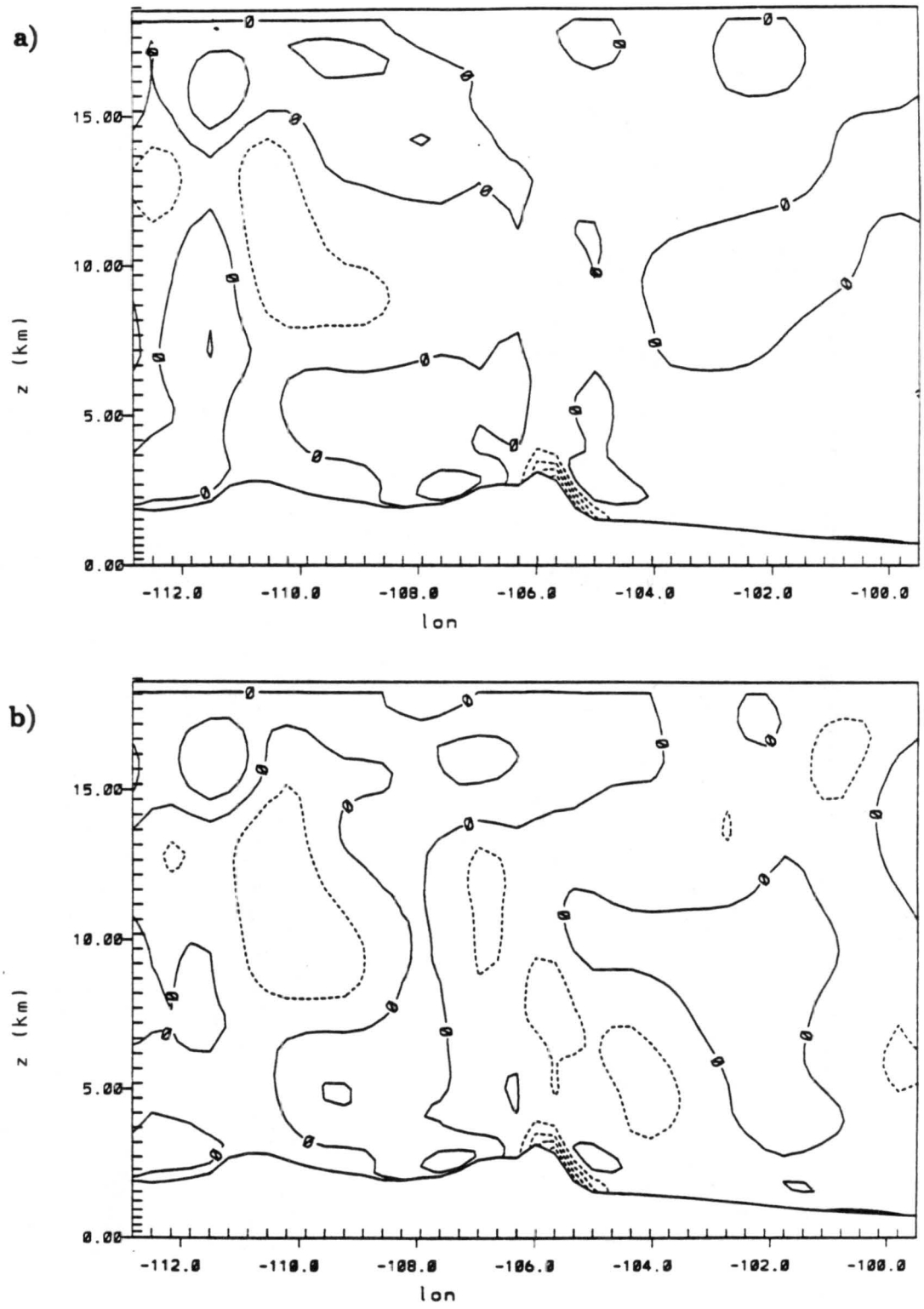

Figure 7.1: Vertical profiles of w-component on the fine grid at 40.6°N for a) Experiment 2 with 0.03 m/s intervals, b) Experiment 3 with 0.03 m/s intervals, c) Experiment 4 with 0.06 m/s intervals, and d) Experiment 5 with 0.1 m/s intervals; all at 0000 UTC 30 July 1987.

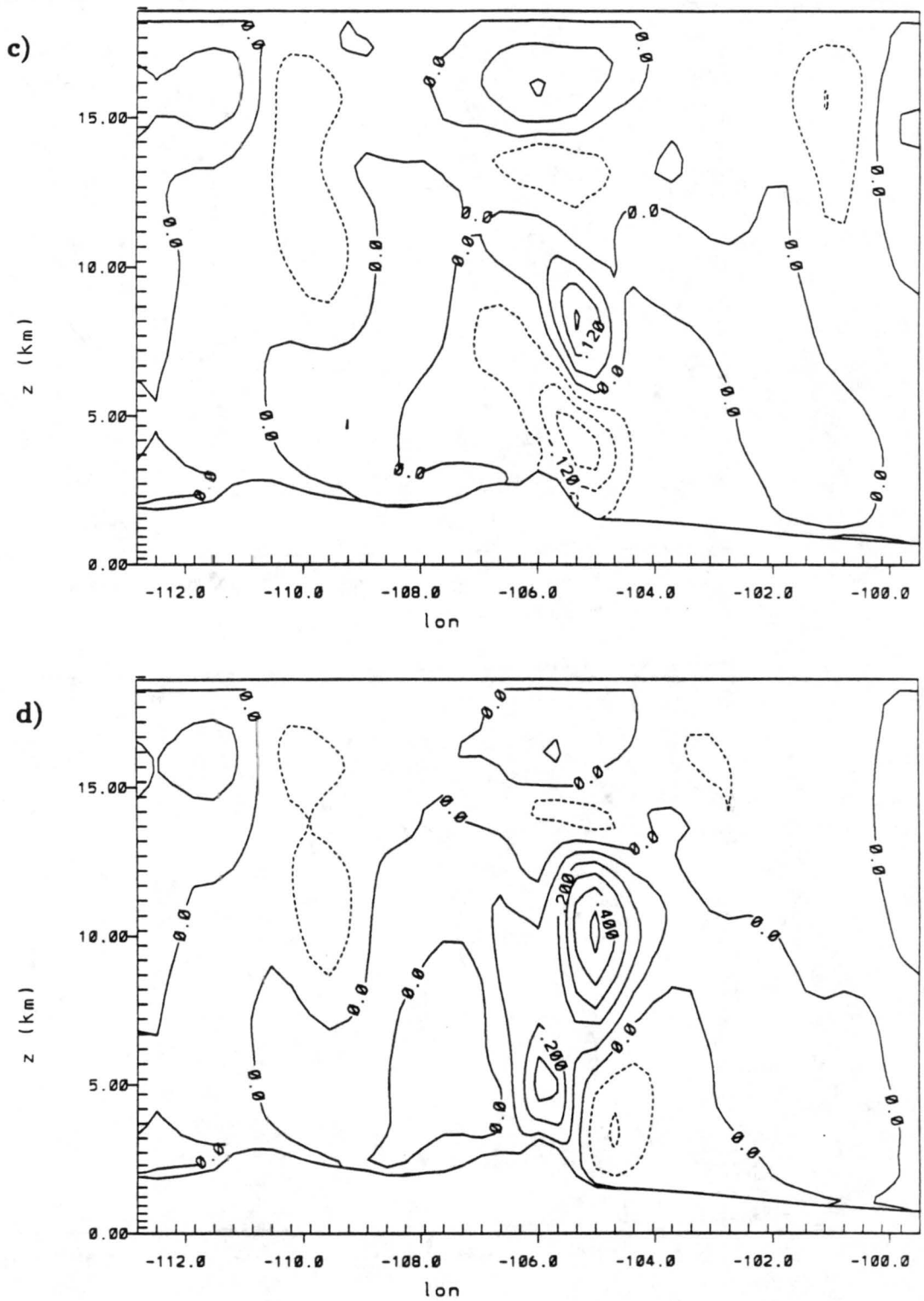

Figure 7.1: Continued.

temperature field and surface total mixing ratio; small changes occurred in some of the horizontal wind fields; and significant changes occurred in the w wind fields (especially a few kilometers above the surface), the upper-level total mixing ratio fields and the accumulative surface precipitation amounts. Since the results are clearly affected by the various precipitation rates, the accuracy of the estimated rain rates are very important.

Based on the three estimates of precipitation rates used in this thesis the one estimated from the sparse PAM surface data (compared to the storm size) is probably to low, due to the spatial variability of the convective rainfall. On the other hand, radar-derived rain rates estimated from the Marshall-Palmer relationship (applicable to general rainfall conditions) are known for producing values that are too high for convective precipitation. Therefore, the most accurate precipitation rate is probably the radar-derived rate estimated by the Fankhauser Z-R relation, which was an average of six Z-R relationships (most of them developed for mid-latitude convective storms), and was used in Experiment 4. Unnfortunately, it was the results from Experiment 5, not Experiment 4, that produced the most realistic results of the 12 hour simulations. This suggests that, in addition, to finding the most accurate precipitation rate, adjustments to the heating rates and/or use of a finer grid is needed to produce QPFs that compare favorably to the observed data.

Chapter 8

CONCLUSIONS AND SUGGESTIONS FOR FUTURE RESEARCH

8.1 Conclusions

The main objective of this thesis was to determine the impact of using heating rates, inferred from estimated precipitation rates, to override the model predicted heating rates (in selected areas), in an attempt to guide the model's atmosphere to a more desirable state. Several numerical experiments were conducted to investigate the impact of the forced heating rates on QPFs, in addition to examining the affects of allowing more time for the model to generate (or spin-up) the dynamics needed to produce more accurate forecasts and to examine the sensitivity of the model to a variety of rainfall rates. Based on the results from these experiments, the following conclusions were made.

- The 12 hour simulation (with no forced heating) did a poor job of simulating the storm in northeast Colorado. This indicates that maybe the model dynamics and physics-parameterizations did not have sufficient time to develop mesoscale structures.

- The 24 hour simulation (which had no forced heating) produced improved horizontal wind patterns near the surface which led to relatively stronger upward vertical motion and simulated precipitation. Thus, the 24 hour simulation made a better QPF then the similar 12 hour forecast. Nevertheless, the predicted storm was positioned incorrectly with the southern part of the storm located in east central Wyoming, whereas the observed storm (based on data from the Radar Summary maps) was mostly located over northeast Colorado, with the northern most part of the storm located in east-central Wyoming. This indicates that the model was not able to

resolve all the terrain-induced and surface forcing features needed to generate the appropriate dynamics for localized ordinary thunderstorms, thus, another method is required to produce better QPFs in a shorter time period.

- In general, forced convective heating provided better QPFs than the model heating; however, this was dependent on the rain rate estimates used to infer the latent heating.

- The RAMS model was extremely sensitive to the precipitation rates used to infer the various heating rates. Smaller precipitation rates (2.3 mm/hr) resulted in no changes in the simulated fields, whereas larger values (7.1 and 11.4 mm/hr) produced significant changes. This indicates the importance of obtaining the most accurate precipitation rate.

- The forced heating rate based on the 11.4 mm/hr rainfall rate produced the most accurate forecast but the 7.1 mm/hr rain rate was probably the best estimate. This suggests that more heating is needed in the model than can be justified from observed rainfall rates.

An example of how the technique employed in this study could be used is illustrated in the following hypothetical scenario. Suppose, while performing a 12-24 hour forecast in real-time, it is determined that convection is forming in regions not predicted by the model. Using an interactive workstation, determine from radar, satellite and/or surface rain gauges, the rain amounts and areal distributions. Then "hot" start RAMS just before the unpredicted convection begins by, interactively, specifying the area of imposed heating, the rainfall rate contours and the heating profile parameters. An "adjusted" 6-12 hour forecast is then performed.

8.2 Suggestions for Future Research

Despite the improvement shown in some of the short-range (12 hours) forecasts that incorporated the forced heating rates, several changes are necessary to produce

forecasts that compare even better with the observed atmosphere. The fine grid spacing of ~28 km is to coarse to detect some of the mesoscale features. Thus, a finer grid is needed to adequately resolve mesoscale features of localized ordinary thunderstorms. A new cumulus parameterization scheme developed by Weissbluth (1991), currently being implemented in RAMS, will allow future simulations to be run on a finer grid. Another problem encountered with the procedure used in this thesis is that the duration of the latent-heat forcing was relatively short (one hour) because of a constant value is being used. However, this short time period may be insufficient to allow the model dynamics to produce mesoscale circulations of realistic amplitudes. Thus, another suggestion for improved results is to progressively add the rainfall rates over longer time periods. This will give the model more time to respond to the heating. Another problem is that the parabolic shape of the heating profile may not be realistic, thus, future studies should investigate how sensitive the results are to the vertical structure of the heating profile. There is also some uncertainty in using single estimates of rain rate averages to estimate grid-box averages that are converted to latent heating rates. Horizontally-varying rainfall rates should be used to infer horizontal variations in heating rates. Finally, utilizing a four-dimensional data assimilation approach, in which inferred heating is combined with wind estimates from wind profilers and/or single-Doppler radar, may be beneficial for future research since, in principle, the initial conditions will then be in better dynamic balance and contain more mesoscale structure than experiments based on a static initialization or solely by diabatic heating.

REFERENCES

Adler, R. F., and E. B. Rodgers, 1977: Satellite-observed latent heat release in a tropical cyclone. *Mon. Wea. Rev.*, **105**, 956-963.

Ahrens, D. C., 1982. "Meteorology Today an Introduction to Weather, Climate, and the Environment". West Publishing Company, St. Paul, Minnesota.

Anthes, R. A., E. Y. Hsie, and Y. H. Kuo, 1981: Impact of data and initialization procedures on variations of vertical motion and precipitation in mesoscale models. *Proc. IAMAP Symposium*, Hamburg, 25-28 August 1981, 245-257.

Anthes, R. A., 1977: Hurricane model experiments with a new cumulus parameterization scheme. *Mon. Wea. Rev.*, **105**, 287-306.

Atlas, D., 1964: Advances in radar meteorology. *Adv. in Geophys.*, **10**, 317-478.

Augustine, J. A., C. G. Griffith, W. L. Woodley and J. G. Meitin, 1981: Insights into errors of SMS-inferred GATE convective rainfall. *J. Appl. Meteor.*, **20**, 509-520.

Barge, B. L., 1974: Polarization measurements of precipitation backscatter in Alberta. *J. Rech. Atmos.*, **8**, 163-173.

Barnes, S. L., 1973: Mesoscale objective map analysis using weighted time series observations. NOAA Tech. Memo. ERL NSSL-62, 60 pp. [NTIS COM-73-10781].

Benoit, R., and M. Roch, 1987: Impact of a direct assimilation of satellite- inferred precipitation rates into a regional meteorological model. Proc. Symp. on *Mesoscale*

Analysis and Forecasting Incorporating Nowcasting, Vancouver, 617-623 (Available from European Space Agency, ESTEC, Noordwijk, Netherlands).

Bradford, M., 1988: GEMINI - The GEneral INterpolation Interface. Internal NCAR/MMM software documentation. 60 pp.

Chandrasekar, V., and V. N. Bringi, 1987: Simulation of radar reflectivity and surface measurements of rainfall. *J. Atmos. Oceanic Tech.*, **4**, 464-478.

Chen, C., and W. R. Cotton, 1983: A one-dimensional simulation of the stratocumulus-capped mixed layer. *Boundary-Layer Meteor.*, **25**, 289-321.

Clark, T. L., 1977: A small-scale dynamic model using a terrain-following coordinate transformation. *J. Comp. Phys.*, **24**, 186-215.

Cotton W. R., R. L. George and K. R. Knupp, 1982: An intense, quasi-steady thunderstorm over mountainous terrain. Part I: Evolution of the storm-initiating mesoscale circulation. *J. Atmos. Sci.*, **39**, 328-342.

Cotton, W. R., and R. A. Anthes, 1989. "Storm and Cloud Dynamics." Academic Press, Inc., San Diego.

Cram, J. M., 1990: Numerical simulation and analysis of the propagation of a prefrontal squall line. Ph.D. thesis, Colorado State University, Fort Collins, Colorado, 332 pp

Danard, M., 1985: On the use of satellite estimates of precipitation in initial analyses for numerical weather prediction. *Atmosphere-Ocean*, **23**, 23-42.

Dennis, A.S., P. L. Smith, G. A. P. Peterson and R. D. McNeil, 1971: Hailstone size distributions and equivalent radar reflectivity factors computed from hailstone momentum records. *J. Appl. Meteor.*, **10**, 79-85.

Doviak, J. D., 1983: A survey of radar rain measurement techniques. *J. Climate Appl. Meteor.*, **22**, 832-849.

Dye, J. E., and B. E. Martner, 1978: The relationship between radar reflectivity factor and hail at the ground for northeast Colorado hailstorms. *J. Appl. Meteor.*, **17**, 1335-1341.

Fankhauser, J. C., 1988: Estimates of Thunderstorm Precipitation Efficiency from Field Measurements in CCOPE. *Mon. Wea. Rev.*, **116**, 663-684.

Fiorino, M., and T. T. Warner, 1981: Incorporating surface winds and rainfall rates into the initialization of a mesoscale hurricane model. *Mon. Wea. Rev.*, **109**, 1914-1929.

Gal-Chen, Tzvi and R. C. J. Somerville, 1975a: On the use of a coordinate transformation for the solution of the Navier-Stokes equations. *J. Comp. Phys.*, **17**, 209-228.

— and —, 1975b: Numerical solution of the Navier-Stokes equations with topography. *J. Comp. Phys.*, **17**, 276-310.

Geotis, S.G., 1963: Some radar measurements of hailstorms. *J. Appl. Meteor.*, **2**, 270-275.

Griffith, C. G., W. L. Woodley, P. G. Grube, D. W. Martin, J. Stout and D. N. Sikdar, 1978: Rain estimation from geosynchronous satellite imagery–visible and infrared studies. *Mon Wea. Rev.*, **106**, 1153-1171.

Heckman, S. T., 1991: Numerical simulation of cirrus clouds - FIRE case study and sensitivity analysis. M.S. thesis, Atmos. Sci. Paper No. 483, Colorado State University, Dept. of Atmospheric Science, Fort Collins, CO 80523, 132 pp.

Jones, D. M. A., 1955: Three cm and ten cm wavelength radiation backscatter from rain. *Proc., Fifth Weather Radar Conf.*, Boston, Amer. Meteor. Soc., 281-285.

Klemp, J. B., and R. B. Wilhelmson, 1978a: The simulation of three-dimensional convective storm dynamics. *J. Atmos. Sci.*, **35**, 1070-1096.

— and —, 1978b: Simulations of right- and left-moving storms produced through storm splitting. *J. Atmos. Sci.*, **35**, 1097-1110.

Kuo, H. L., 1974: Further studies of the parameterization of the influence of cumulus convection on large-scale flow. *J. Atmos. Sci.*, **31**, 1232-1240.

Kuo, Y-H., and R. A. Anthes, 1984: Semiprognostic tests of Kuo-type cumulus parameterization schemes in an extratropical convective system. *Mon. Wea. Rev.*, **112**, 1498-1509.

Lejenas, H., 1980: On the influence of the technique of nonlinear normal mode initialization on the nonconvective precipitation rate. *Mon. Wea. Rev.*, **108**, 1465-1468.

Mahrer, Y., and R. Pielke, 1977: A numerical study of airflow over irregular terrain. *Beitr. Phys. Atmos.*, **50**, 98-113.

Marshall, J. S., and W. M. K. Palmer, 1948: The distribution of raindrops with size. *J. Meteor.*, **5**, 165-166.

Martner, B. E., 1975: Z-R and Z-W_o relations from drop size measurements in high plains thunderstorms. *Preprints, Ninth Conf. on Severe Local Storms*, Boston, Amer. Meteor. Soc., 307-310.

Mohr, C. G., L. J. Miller, R. L. Vaughan and H. W. Frank, 1986: On the merger of mesoscale data into a common cartesian format for efficient and systematic analysis. *J. Atmos. Oceanic Tech.*, **3**, 143-161.

Ninomiya, K., and K. Kurihara, 1987: Forecast experiment of a long-lived mesoscale convective system in Baiu frontal zone. *J. Meteor. Soc. Japan*, **65**, 885-899.

Puri, K., and M. J. Miller, 1990: Sensitivity of ECMWF analyses-forecasts of tropical cyclones to cumulus parameterization. *Mon. Wea. Rev.*, **118**, 1709-1741.

Salmon, E. M., and T. T. Warner, 1986: Short-term numerical precipitation forecasts initialized using a diagnosed divergent-wind component. *Mon. Wea. Rev.*, **114**, 2122-2132.

Seliga, T. A., and V. N. Bringi, 1976: Potential use of differential reflectivity measurements at orthogonal polarizations for measuring precipitation. *J. Appl. Meteor.*, **15**, 69-76.

Smith, E. A., A. Mugnai, H. J. Cooper, G. J. Tripoli and X. Xiang, 1991: Foundations for statistical-physical precipitation retrieval from passive microwave satellite measurements. Part 1: brightness temperature properties of a time dependent cloud-radiation model. Re-submitted to J. Appl. Meteor.

Smith, P. L., Jr., D. Z. Cain and A. S. Dennis, 1975: Derivation of an R-Z relationship by computer optimization and its use in measuring daily areal rainfall. *Preprints, 16th Conf. on Radar Meteor.*, Boston, Amer. Meteor. Soc., 461-466.

Tarbell T. C., T. T. Warner and R. A. Anthes, 1981: An example of the initialization of the divergent wind component in a mesoscale numerical model. *Mon. Wea. Rev.*, **109**, 77-95.

Tremback, C. J., 1990: Numerical simulation of a mesoscale convecttive complex: Model development and numerical results. Ph.D. dissertation, Atmos. Sci. Paper No. 465, Colorado State University, Dept. of Atmospheric Science, Fort Collins, CO 80523, 247 pp.

—, and R. Kessler, 1985: A surface temperature and moisture parameterization for use in mesoscale numerical models. *Preprints, 7th Conference on Numerical Weather Prediction*, 17-20 June 1985, Montreal, Canada, Amer. Meteor. Soc.

—, G. J. Tripoli, and W. R. Cotton, 1985: A regional scale atmospheric numerical model including explicit moist physics and a hydrostatic time-split scheme. *Preprints, 7th Conference in Numerical Weather Prediction*, 17-20 June 1985, Montreal, Quebec, Amer. Meteor. Soc.

Tripoli, G. J., 1986: A numerical investigation of an orogenic mesoscale convective system. Ph.D. dissertation, Atmos. Sci. Paper No. 401, Colorado State University, Dept. of Atmospheric Science, Fort Collins, CO 80523, 290 pp.

—, and W. R. Cotton, 1980: A numerical investigation of several factors contributing to the observed variable intensity of deep convection over South Florida. *J. Appl. Meteor.*, **19**, 1037-1063.

—, and —, 1982: The Colorado State University three-dimensional cloud/mesoscale-1982. Part I: General theoretical framework and sensitivity experiments. *J. Rech. Atmos.*, **16**, 185-220.

Turpeinen, O. M., L. Garand, R. Benoit and M. Roch, 1990: Diabatic initialization of the Canadian regional finite-element (RFE) model using satellite data. Part I: Methodology and application to a winter storm. *Mon. Wea. Rev.*, **118**, 1381-1395.

Ulbrich, C. W., 1983: Natural variations in the analytical form of raindrop size distribution. *J. Climate Appl. Meteor.*, **22**, 1764-1775.

Waldvogel, A., and B. Federer, 1976: Large raindrops and the boundary between rain and hail. *Preprints, 17th Conf. on Radar Meteor.*, Boston, Amer. Meteor. Soc., 167-172.

Wang, W. and T. T. Warner, 1988: Use of Four-Dimensional Data Assismilation by Newtonian Relaxation and Latent-Heat Forcing to Improve a Mesoscale-Model Precipation Forecast: A Case Study. *Mon. Wea. Rev.*, **116**, 2593-2613.

Weissbluth, M. J., 1991: Convective parameterization in mesoscale models. Ph.D. dissertation, Colorado State University, Dept. of Atmospheric Science, Fort Collins, CO 80523, 211 pp.

Wilson, J. W., J. A. Moore, G. B. Foote, B. Martner, A. R. Rodi, T. Uttal, and J. M. Wilczak, 1988: Convective Initiation and Downburst Experiment (CINDE). *Bull. Amer. Meteor. Soc.*, **69**, 1328-1348.